Impulse TDR and its Application to Characterisation of Antennas

A thesis
submitted in fulfillment
of the requirements for the degree
of
Master of Philosophy
in Electronic Engineering
at the
University of Waikato
by

Steven Owen McCabe

University of Waikato

2011

Abstract

Passive microwave systems are traditionally characterised in the frequency-domain with a vector network analyser (VNA). The measurement of antennas typically takes place in an anechoic chamber where the interference from spurious reflections and outside noise is minimised. Despite the high level of accuracy achieved with this approach, such facilities have high costs associated with them.

Recent publications have demonstrated the characterisation of antennas using a step-function time domain reflectometer (TDR) along with frequency-domain processing techniques. Localisation of the measurement in time prior to transformation allows for the dismissal of unwanted spurious reflections, eliminating the need for an anechoic chamber.

An alternative technique is proposed whereby an impulse generator is employed in place of the step generator in a TDR. The advantage conferred by "impulse TDR" (ITDR) is that more energy is available at higher frequencies than with conventional step TDR, leading to a higher bandwidth and signal-to-noise ratio (SNR). The theoretical result is compared with measurement.

Preface

The motivation behind this work was to develop new applications for a class of impulse generators that have recently become available. The device was originally intended as a phase reference standard for non-linear vector network analysers (NVNAs) but has also been found useful in the measurement of group delay in frequency-translating devices. The department of Engineering has possession of an Agilent U9391C (26.5 GHz version).

A recent paper described the advantages of characterising antennas with time-domain reflectometry (TDR), where the stimulus signal was a transient voltage step. With knowledge that the energy in a step falls rapidly with increasing frequency, it became obvious that such a measurement would have limited bandwidth. On the other hand, an impulse-like signal with comparable rise-time such as from our generator would have energy distributed over a much flatter and wider bandwidth.

With this in mind, a research proposal was drafted to investigate the measurement of band-pass microwave systems such as wideband antennas using impulse TDR. After a culmination of one year's work and an equipment failure that delayed progress by about four months, impulse TDR was finally demonstrated as a viable approach for measuring antennas. The intentions of this thesis are to present these findings, while addressing existing methods and making performance comparisons. Background information, including the theory behind the work is discussed. Suggestions for future research are proposed and conclusions are drawn.

Parts of the research have been published. A manuscript describing the advantages of impulse TDR to the characterisation of antennas has been published in the IEEE Microwave and Wireless Components Letters. A second manuscript describing the use of impulse TDR and the differences between this and step

TDR will be presented at the Asia-Pacific Microwave Conference in December 2011. These are world-class venues for the reporting of microwave research.

Chapter Synopses

Chapter 1 provides an overview of sampling and discusses the importance of the Nyquist-Shannon sampling theorem. Comparisons are made between the real-time and equivalent-time sampling techniques employed in the front-end of modern digital oscilloscopes.

Chapter 2 is a review of transmission line theory. Key concepts are discussed including the propagation of electromagnetic waves in coaxial cable, characteristic impedance, and the effect of a load impedance on a transmission line.

Chapter 3 explores the use of TDR to measure the impedance of an arbitrary load. The steps necessary for developing an equivalent circuit from the analysis of voltage waveforms are described. Various applications for TDR are discussed including the measurement of the loss in transmission lines and the dielectric properties of materials.

Chapter 4 investigates the application of TDR to the characterisation of antennas. Practical considerations for the acquisition of the time-domain measurements are examined along with the pre-processing and transformation algorithms necessary for the computation of the reflection scattering parameter $S_{11}(f)$.

Chapters 5, 6, 7, and 8 explore the advantages of making impulse TDR measurements where the excitation signal is a voltage impulse instead of the voltage step used in traditional TDR. The Fourier transforms for the impulse and step test signals are compared through simulation followed by measurement of a wideband antenna. Recommendations for the application of impulse TDR are made along with suggestions for future research. Parts of the material contained in these chapters have been published in an IEEE journal and IEEE conference proceeding.

Acknowledgements

First and foremost I would like to thank my primary supervisor Professor Jonathan Scott for contributing his wealth of knowledge and tremendous support throughout the project. I would like to extend my thanks to Dr. Michael Cree for providing his supervision when needed. Agilent Technologies Component Test Division kindly provided the loan of essential equipment and detailed support. Without their contribution the project would not have been possible. Furthermore, thanks are due to Grant at Skynet Data Communications Technology Ltd for supplying the test antennas. Pawan Shrestha's effort in organising access to key equipment and components is greatly appreciated. Last but by no means least, I am indebted to my family for their encouragement, support, and understanding when I was often working until late hours of the night to meet deadlines.

Contents

List of Figures

List of Tables

Chapter 1

Sampling Techniques and the Equivalent-Time Sampling Oscilloscope

1.1 Overview

An equivalent-time sampling oscilloscope, or more commonly sampling oscilloscope, has the ability to measure signals with much higher frequency components than would be possible using a real-time digital storage oscilloscope (DSO) of similar caliber [1]. The highest bandwidth achievable from a real-time oscilloscope currently stands at 32 GHz [2] while equivalent-time sampling oscilloscopes have reached bandwidths in excess of 80 GHz [3]–[5]. Differences lie in the front-end architectures and sampling techniques used to digitise the input signals.

1.2 Sampling

Sampling is the process of converting a continuous analog signal into a discrete digital representation [6], implemented by means of a sample-and-hold (S/H) circuit and an analog-to-digital converter (ADC) as shown in figure 1.1. The S/H circuit consists of a sampling gate (shown as a simple switch) and a holding capacitor. When the switch is closed for a short period of time, the capacitor charges up to some fraction of the input voltage. The switch is then opened to isolate the capacitor from the input, leaving the voltage on the capacitor constant [7]. Finally, the ADC quantises the voltage level into a discrete digital form to be stored in memory.

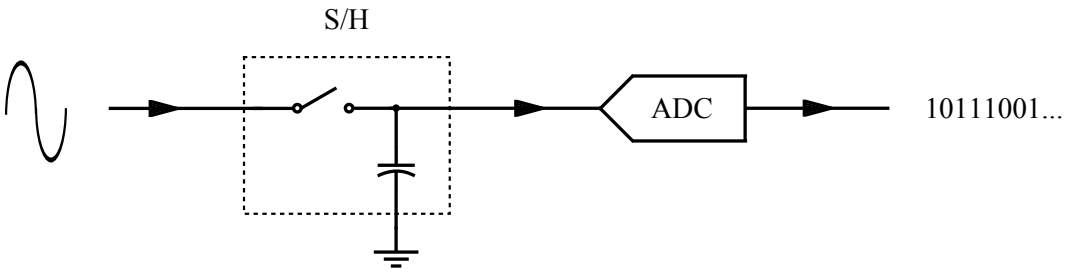

Figure 1.1: *Continuous analog signals are converted into digital form using a sample-and-hold (S/H) circuit and an analog-to-digital converter (ADC).*

The sampling rate f_S is defined as the number of samples acquired per second:

$$f_S = \frac{1}{t_S} \tag{1.1}$$

where t_S is the interval of time between each sample. The maximum sampling rate is determined by the speed of the S/H circuit and ADC. To achieve a high bandwidth with real-time sampling, a high sampling rate is essential. Conversely with equivalent-time sampling, a significantly lower sampling rate can still achieve the same high bandwidth.

1.3 Real-Time Sampling

Digital storage oscilloscopes employ real-time sampling, a technique where the sampler operates at a high sampling rate to acquire enough samples in a single sweep to accurately represent the input signal [8]. For this reason, DSOs have the ability to capture transient signals. Furthermore, an external trigger signal is not required. The sampling rate required to sufficiently represent a band-limited analog signal in a digital form is governed by the Nyquist-Shannon sampling theorem. The sampling theorem states that the maximum frequency component f_{max} present within the analog signal must be less than the Nyquist frequency f_N [6]:

$$f_{max} < f_N \tag{1.2}$$

where the Nyquist frequency f_N (not to be confused with Nyquist rate) is defined as half of the sampling rate f_S:

$$f_N = \frac{1}{2} f_S \tag{1.3}$$

The sampling theorem also requires the samples to be equally spaced [9]. Provided that the sampling theorem is satisfied, the digitised signal can be

accurately reconstructed into the original analog form. In figure 1.2(a), an analog signal is sufficiently sampled by meeting the Nyquist-Shannon criteria. When f_{max} approaches f_N (but still within the Nyquist requirements) as in figure 1.2(b), the samples become widely spaced. Interpolation can be used for "filling in the dots" between samples to reproduce the continuous input signal [8].

In the case of undersampling, where $f_{max} \geq f_N$, a phenomenon known as aliasing will occur. Aliasing is the transformation of a high frequency component into a lower frequency component, resulting in a false interpretation of the signal. Figure 1.2(c) is an example of a sinewave signal that is falsely represented by a constant dc level due to aliasing. Figure 1.2(d) is another example of when undersampling causes transformation into a lower frequency alias. Aliasing can be prevented by subjecting the input signals to an anti-alias (low-pass) filter prior to sampling, to ensure any frequency components at or

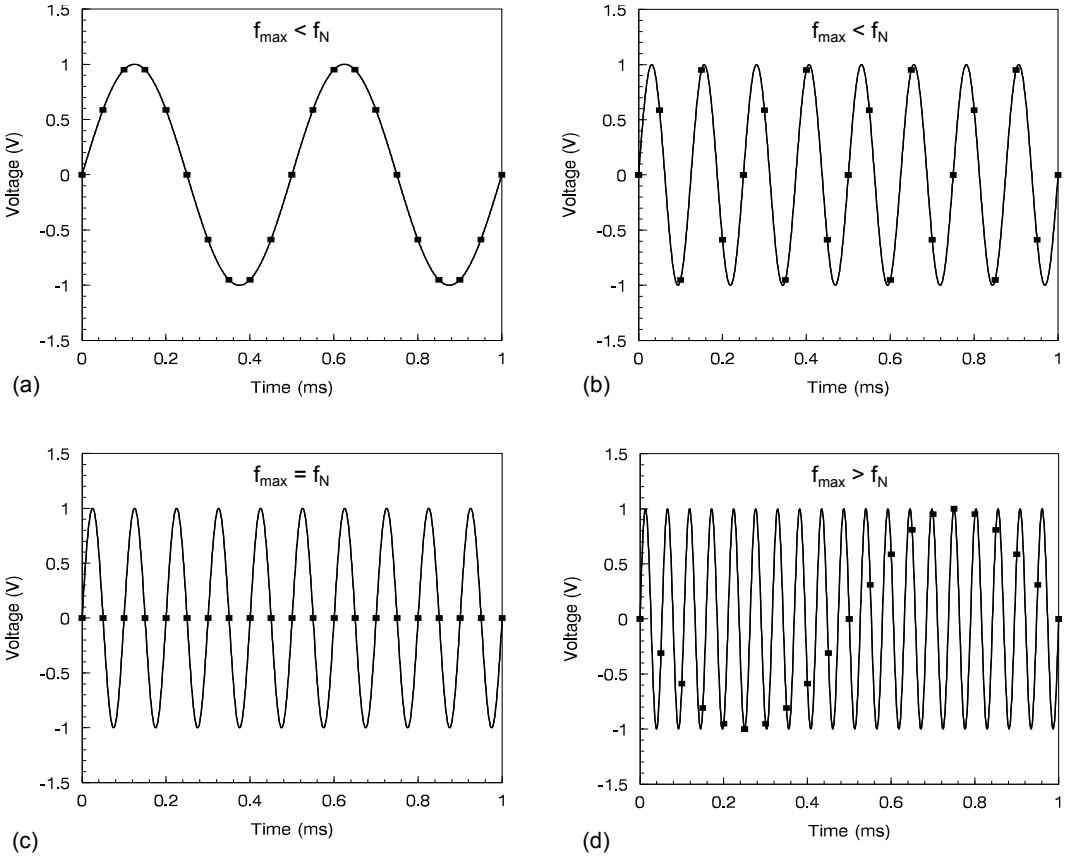

Figure 1.2: *(a) and (b) illustrate signals that are sampled according to the Nyquist-Shannon sampling theorem where $f_{max} < f_N$. In (c), $f_{max} = f_N$, and so the analog signal is aliased as a dc signal. When $f_{max} > f_N$ as in (d), the acquired waveform is aliased and transforms into a lower frequency.*

above the Nyquist frequency are attenuated [10].

1.3.1 Real-time DSO Front-End Architecture

The front-end architecture of a typical real-time DSO is shown in figure 1.3. The high impedance input is protected from over-voltage with fast acting Schottky diodes. A wideband amplifier allows for adjustable gain and offset and must operate over the entire bandwidth of the instrument [8]. The signal is then sampled and quantised with real-time sampling.

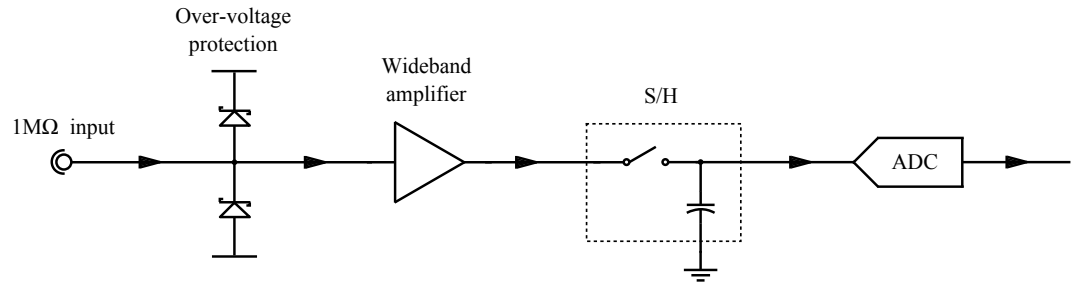

Figure 1.3: *In a conventional DSO, the input signal is fed into a wideband amplifier prior to sampling. Fast acting Schottky diodes protect the input from over-voltage.*

1.4 Equivalent-Time Sampling

Equivalent-time sampling is a technique for the measurement of signals with frequency components higher than the sample rate, which would otherwise be aliased using real-time sampling. The input signal must be periodic and an external synchronous signal is required to trigger the sampler [11]. A clock recovery module is used in situations where a synchronous trigger is unavailable [12]. In figure 1.4 a repetitive waveform is sampled with equivalent-time sampling. A trigger signal initially starts the acquisition of the first sample. After a re-arm time t_{arm}, the sampler waits for the next trigger signal and then adds a precise delay Δt before acquiring the next sample. This process repeats until the entire waveform is acquired, where the time between each sample is equivalent to Δt. The value of Δt depends on the total number of acquired points N and the measurement window time T_w:

$$\Delta t = \frac{T_w}{N-1} \tag{1.4}$$

Although not directly obvious, the Nyquist-Shannon sampling criteria still applies. However for equivalent-time sampling, the Nyquist frequency f_N does

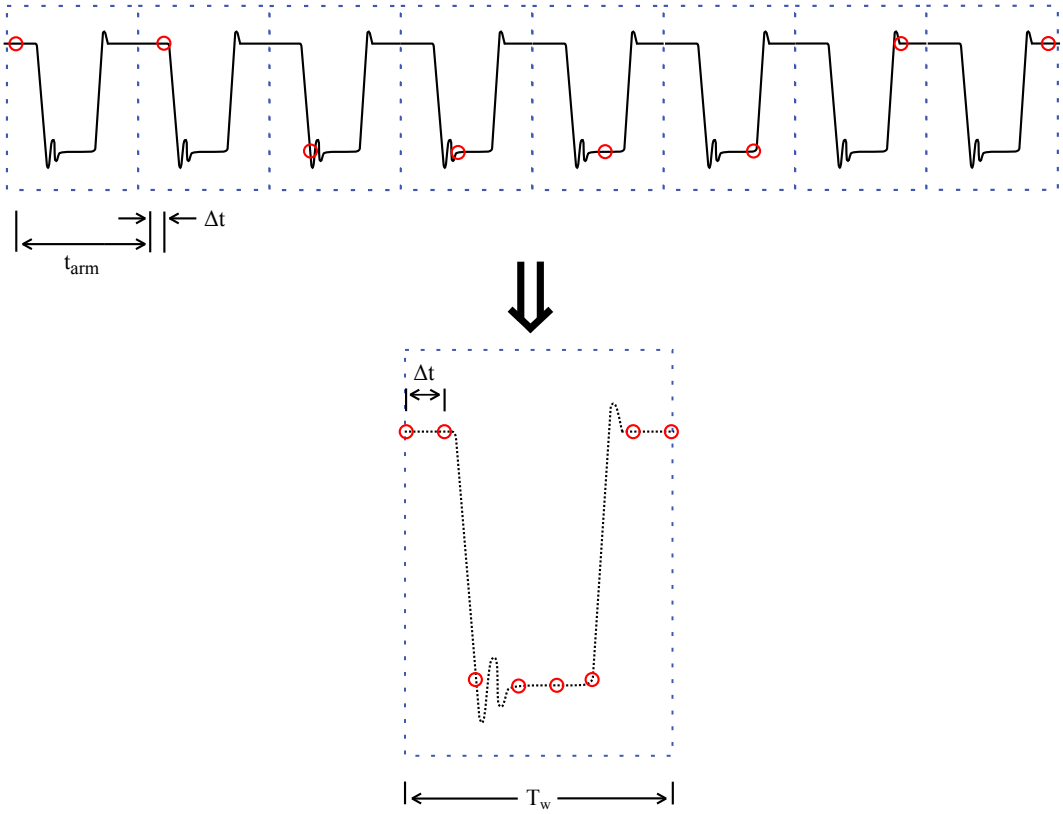

Figure 1.4: *Top: A periodic signal is sampled with equivalent-time sampling. Bottom: The acquired samples are reconstructed so that the period of time between each sample is equivalent to* Δt.

not depend on the sample rate, but instead depends on Δt:

$$f_N = \frac{1}{2\Delta t} = \frac{N-1}{2T_w} \tag{1.5}$$

Provided the condition in 1.2 is met, aliasing will not occur.

1.4.1 Sampling Oscilloscope Front-End Architecture

The front-end architecture of a typical equivalent-time sampling oscilloscope is shown in figure 1.5. A 50Ω input is fed directly into a S/H circuit followed by an amplifier and a high resolution ADC. Due to the low sampling rate, only a low bandwidth amplifier is required. However, because the input is fed directly into the S/H circuit without any prior amplification or attenuation as with real-time DSOs, the sampling gate must handle the full dynamic range. For this reason the maximum measurable input signal is typically less than 1 V peak-to-peak [13]. Furthermore, over-voltage protection is not available as protection diodes add capacitance and would limit bandwidth. This restricts

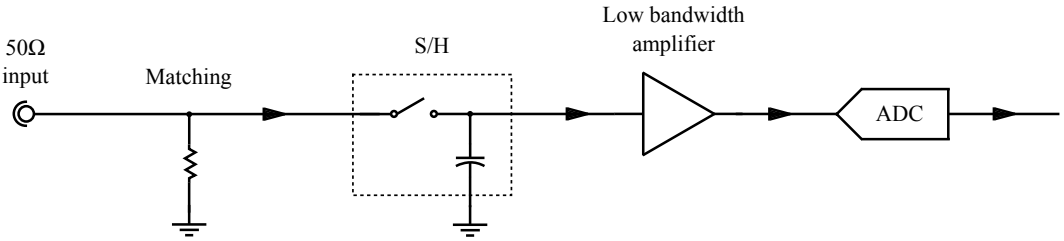

Figure 1.5: *An equivalent-time sampling oscilloscope samples the input signal prior to any amplification or attenuation.*

the maximum allowed voltage at the input to about ±2 V [3].

1.4.2 Sample-and-Hold Circuits

There are numerous designs for the sampling gates used in the front-end of modern digital oscilloscopes [14]–[18]. Real-time DSOs usually integrate the S/H circuit in CMOS, while sampling oscilloscopes typically employ discrete components such as diodes. Various Tektronix sampling oscilloscopes use a bridge of fast acting Schottky diodes [14], similar to the configuration shown in figure 1.6(a). The direction of current in sources I_{S1} and I_{S2} is alternated

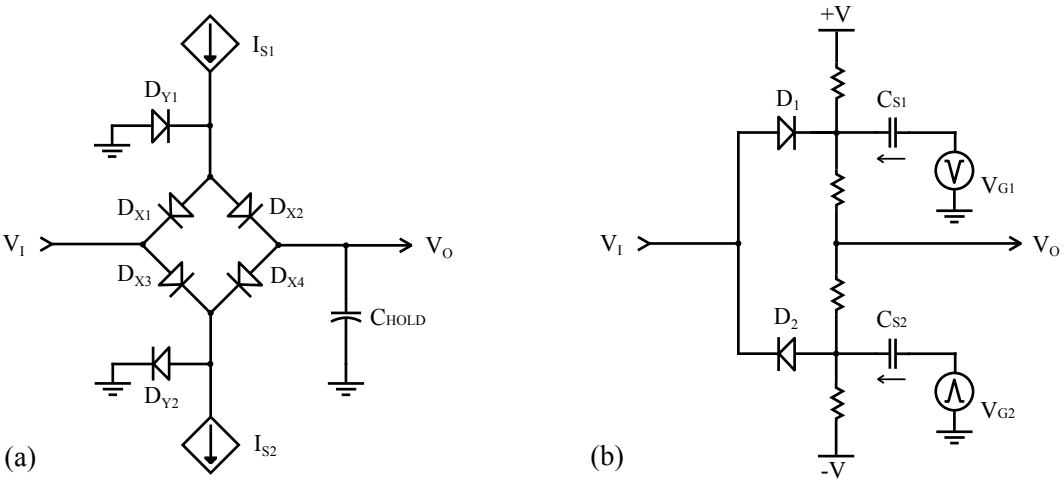

Figure 1.6: *Two common sampling gate designs used in equivalent-time sampling oscilloscopes. (a) Diode bridge configuration, (b) Two-diode sampler.*

causing the diodes to switch between forward and reverse biasing states. When the direction of current is as shown in the figure, diodes D_{X1}–D_{X4} are forward biased while D_{Y1} and D_{Y2} are reverse biased. Since forward biased diodes have low small-signal resistance [19], a low impedance path is formed between the input and holding capacitor C_{HOLD}. The holding capacitor then charges up to some fraction of the input voltage V_I. When the currents from I_{S1} and I_{S2} are reversed, diodes D_{Y1} and D_{Y2} become forward biased, thus transferring

the current to ground. The diodes D_{X1}–D_{X4} become reverse biased, leaving the holding capacitor isolated from the input signal.

Figure 1.6(b) is another common sample-and-hold circuit design similar to what is found in modern sampling oscilloscopes [15]. It works in a similar fashion to the diode bridge configuration, but requires only two diodes. The diodes are normally reverse biased, isolating the input from the sampling capacitors C_{S1} and C_{S2}. A pulse from voltage sources V_{G1} and V_{G2} forward bias the diodes, providing a low impedance path from the input to the sampling capacitors. The sampling capacitor C_{S1} will charge up to some fraction of $V_I + V_{G1}$. The sampling capacitor C_{S2} will charge up to some fraction of $V_I - V_{G2}$. As a result of the resistive divider, the output voltage V_O will equal V_I.

1.4.3 Analog-to-Digital Converters

Real-time DSOs require high speed ADCs to cope with the high acquisition rate and storage of samples. This generally limits the ADC resolution to 8-bits [20]. On the other hand, sampling oscilloscopes employ ADCs with much lower sampling rates and so higher resolutions are obtainable [11]. A resolution between 14 and 16-bits is common [3]–[5].

Chapter 2

RF Transmission Lines

2.1 Overview

A transmission line is a medium used to transfer energy from one location to another. Coaxial cable, hollow waveguide, and microstrip are examples of different transmission media commonly used in radio frequency (RF) systems. Unlike dc and low frequency types such as mains power lines, RF transmission lines must support higher frequency currents, where the propagation of electromagnetic waves must be considered. At these frequencies where the wavelength becomes comparable with or less than the length of the transmission line, various conditions must be taken into account to ensure adequate energy transfer.

2.2 Travelling Waves

As depicted in figure 2.1, the energy generated by a voltage source V_S is transferred to a load impedance Z_L in the form of an incident wave. If there is an impedance mismatch between the transmission line and the load, a reflected wave will propagate in the opposite direction towards the source. The propagation velocity for an electromagnetic wave travelling along a transmission line can be computed from

$$v_p = \frac{c}{\sqrt{\epsilon_r \mu_r}} \tag{2.1}$$

where c is the speed of light in a vacuum (3.0×10^8 ms^{-1}), ϵ_r is the relative permittivity of the dielectric material, and μ_r is the relative permeability of the dielectric material. For a hollow waveguide where air is the dielectric, v_p is approximately equal to c. For a coaxial cable where a solid Teflon dielectric

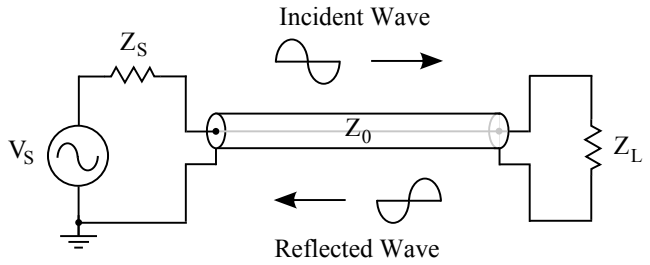

Figure 2.1: *Incident and reflected waves on a transmission line.*

is often used, v_p is approximately 69% of c [21].

The wavelength is related to the propagation velocity by

$$\lambda = \frac{v_p}{f} \tag{2.2}$$

where f is the frequency of the applied signal. A transmission line with an electrical length of more than $\frac{\lambda}{4}$ is classed as a long line [22], where the propagation of electromagnetic waves must be considered. Conversely, shorter electrical lengths are called short lines and can be simply characterised with Ohm's law.

2.3 Characteristic Impedance

Any transmission line that supports an electromagnetic wave has a characteristic impedance Z_0.[1] The characteristic impedance is the ratio of voltage to current for a wave travelling in one direction along a transmission line [23]. The characteristic impedance of an ideal transmission line is independent of the line's length, operating frequency, and load attached [22]. A transmission line is often characterised using the distributed element model [23] as shown in figure 2.2. The transmission line is replaced with a pair of perfect conductors and a continuous distribution of R's, L's, G's, and C's. For an infinitely long transmission line where travelling waves propagating in only one direction can exist,

$$Z_0 = \sqrt{\frac{R + j\omega L}{G + j\omega C}} \tag{2.3}$$

where R, L, G, and C are defined per unit length, and $\omega = 2\pi f$. If the

[1] Coaxial cable typically used in general low-power RF applications such as test and measurement, has a characteristic impedance of 50 Ω.

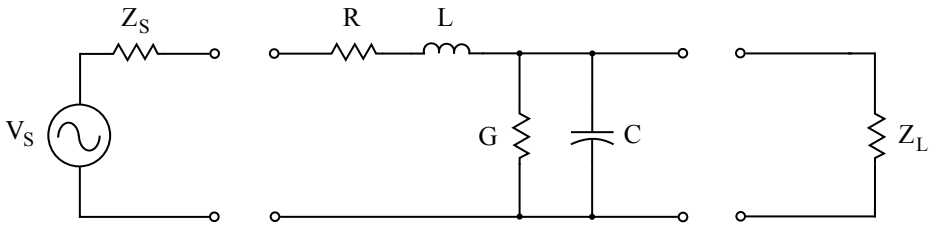

Figure 2.2: *The distributed element model for a transmission line between a source and load.*

transmission line is assumed to be lossless, Z_0 can be approximated to:

$$Z_0 \simeq \sqrt{\frac{L}{C}} \tag{2.4}$$

2.4 Non-Resonant Lines

A non-resonant line is a transmission line with electromagnetic waves propagating in only one direction. A transmission line that is infinite in length can be considered non-resonant [22], as the wave generated by the source will only ever see the characteristic impedance of the line and therefore no reflections can form in the opposite direction. A more practical example of a non-resonant line is a transmission line (finite in length) that is properly terminated with a load impedance equal to the characteristic impedance:

$$Z_L = Z_0 \tag{2.5}$$

In this case the load impedance is said to be matched with the characteristic impedance, where all energy is absorbed by the load with nothing reflected.

2.5 Resonant Lines

A resonant line is a transmission line where there exists electromagnetic waves propagating in opposite directions to one another - an incident wave travelling toward the load and a reflected wave heading back toward the source [22] as was shown in figure 2.1. This situation arises when the impedance of the load differs from the characteristic impedance of the transmission line:

$$Z_L \neq Z_0 \tag{2.6}$$

The superposition of the incident and reflected waves is a standing wave. A pure standing wave is produced when all of the energy from the incident wave is reflected, forming a stationary wave on the transmission line where only the amplitude varies with time. A partial standing wave is produced when only part of the incident wave is reflected, resulting in a combination of a standing wave and travelling wave. The voltage standing wave ratio (VSWR) is defined as the ratio of the maximum to minimum voltages of a standing wave:

$$\text{VSWR} = \frac{V_{max}}{V_{min}} \tag{2.7}$$

The VSWR measurement is limited because there is no phase information [23]. The complex reflection coefficient Γ is a better measure of the system performance as it includes phase information. Γ is the ratio of the reflected voltage V_{ref} to the incident voltage V_{inc} [24] and is related to the load impedance by

$$\Gamma = \frac{V_{ref}}{V_{inc}} = \frac{Z_L - Z_0}{Z_L + Z_0} \tag{2.8}$$

Γ can range from 1 for a $Z_L = \infty$, to -1 for a $Z_L = 0$. For a matched load where $Z_L = Z_0$, $\Gamma = 0$. The magnitude of Γ is related to VSWR by

$$|\Gamma| = \frac{VSWR - 1}{VSWR + 1} \tag{2.9}$$

A load impedance will generally be characterised by its reflection coefficient at many frequencies. A vector network analyser (VNA) is an instrument most commonly used to measure $\Gamma(f)$, however a time domain reflectometer (TDR) has its advantages as will be discussed in subsequent chapters.

Chapter 3

Time-Domain Reflectometry

3.1 Overview

Time-domain Reflectometry (TDR) is a well-known technique for the analysis of electronic systems [25]–[27]. It is typically used to characterise and locate the position of a discontinuity or termination along an RF transmission line. A transient voltage step is transmitted to the discontinuity and a wave is reflected corresponding to the mismatched impedance. Through analysis of the reflected wave, the discontinuity can be characterised by its equivalent circuit.

3.2 Measurement System

A modern TDR instrument consists of a wide bandwidth oscilloscope (typically an equivalent-time sampling type) with a built-in step generator as depicted in figure 3.1. A transmission line with a characteristic impedance Z_0 connects the device-under-test (shown as a load with impedance Z_L) to the TDR. A positive going voltage step is transmitted through the transmission line toward the load and the incident and reflected waves are monitored on the oscilloscope.

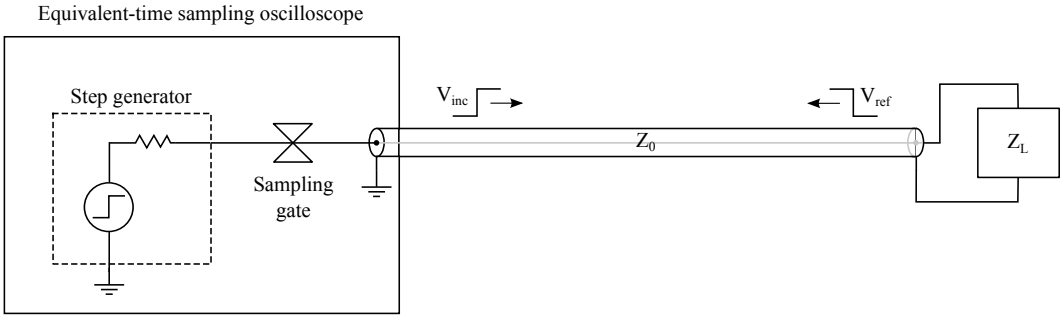

Figure 3.1: *A TDR set-up to measure the load impedance Z_L.*

3.3 Analysis of a Resistive Load

A resistive load impedance (purely real) can be easily identified and characterised using TDR. As was discussed in chapter 2, if an incident wave encounters a change in impedance on a transmission line i.e. a mismatch where $Z_L \neq Z_0$, a reflected wave will be produced. In the case where the transmission line is terminated with $Z_L = Z_0$, no reflection will occur. An example waveform for an arbitrary resistive load as viewed on the oscilloscope is shown in figure 3.2. In the same figure the equivalent circuit is shown.

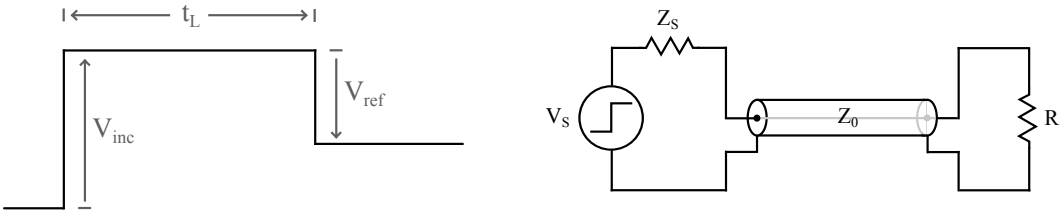

Figure 3.2: *A typical waveform resulting from a resistive load R. The equivalent circuit of the termination is simply a load resistor R.*

The load impedance Z_L can be computed by rearranging equation 2.8:

$$Z_L = Z_0 \frac{1+\Gamma}{1-\Gamma} = Z_0 \frac{1+(V_{ref}/V_{inc})}{1-(V_{ref}/V_{inc})} \tag{3.1}$$

where V_{inc} and V_{ref} are the amplitudes of the incident and reflected waves measured directly from the oscilloscope display. The location of the load at a distance D relative to the TDR is found by

$$D = \frac{v_p t_L}{2} \tag{3.2}$$

where t_L is the time for the wave to propagate to the load and back again as viewed on the oscilloscope. Waveforms for a variety of loads are shown in figure 3.3. The load impedance can be derived from each waveform using equation 3.1. A short or open circuit Z_L is determined by the polarity of the reflected waveform when it is equal in magnitude to the incident waveform. As for the load with an impedance equivalent to the characteristic impedance, no refection is present as all energy is absorbed by the load. For resistive loads where $R < Z_0$, the reflection is a fraction of the incident voltage and has negative polarity. Similarly, for resistive loads where $R > Z_0$, the reflection is a fraction of the incident voltage but has positive polarity.

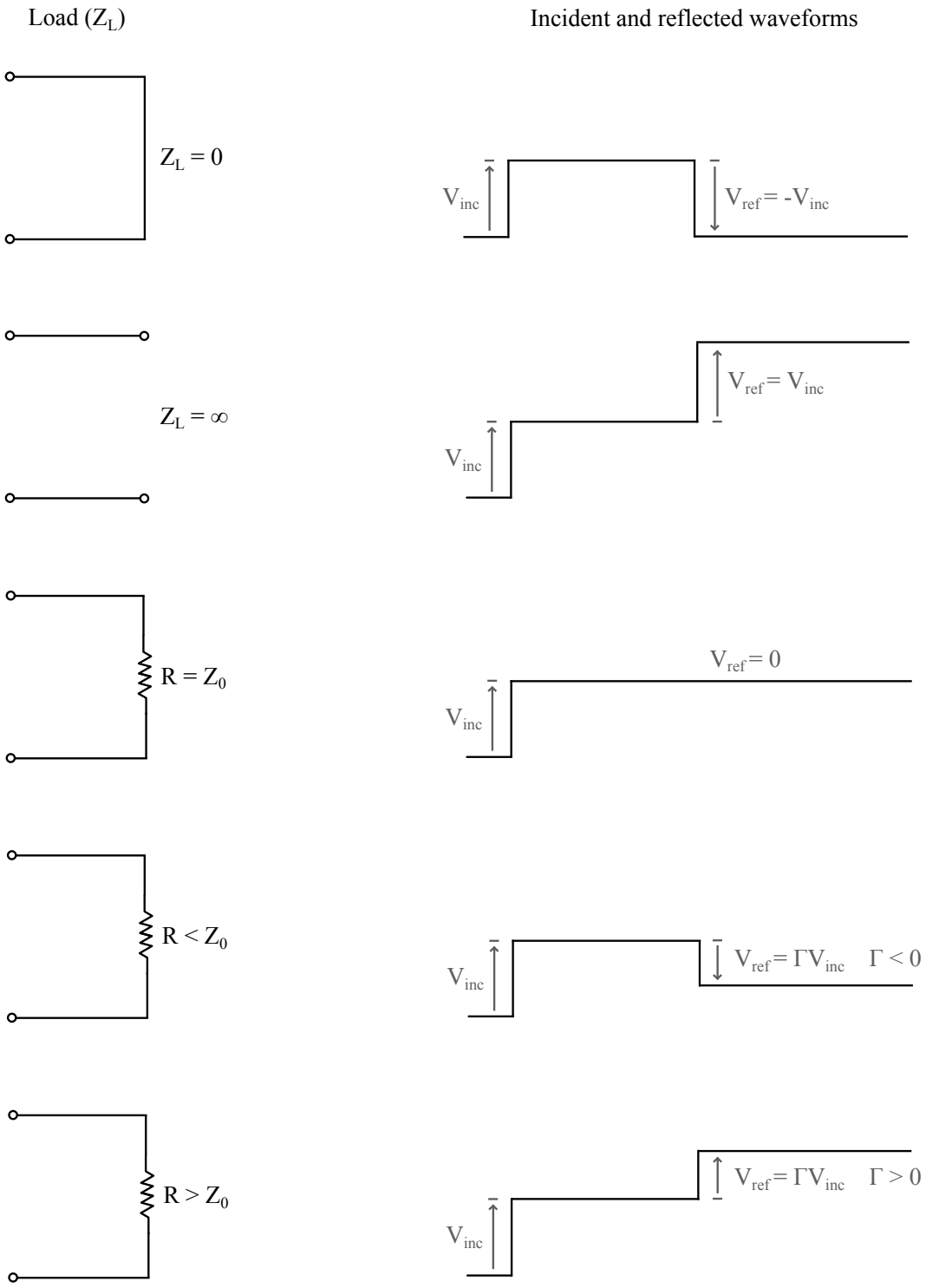

Figure 3.3: *Waveforms to be expected from a variety of load impedances.*

3.4 Analysis of a Complex Load

Complex loads have reactive elements that store and release energy over time [28]. As a result, the reflection from a complex load exhibits an exponential function with a time constant τ corresponding to the amount of resistive and reactive elements within the load [23]. Through measurement of V_{inc}, V_a, V_b, and τ, an equivalent circuit for the load can be established.

3.4.1 Example Waveform: Inductive Load

Figure 3.4 is an example of a typical waveform resulting from a complex load.

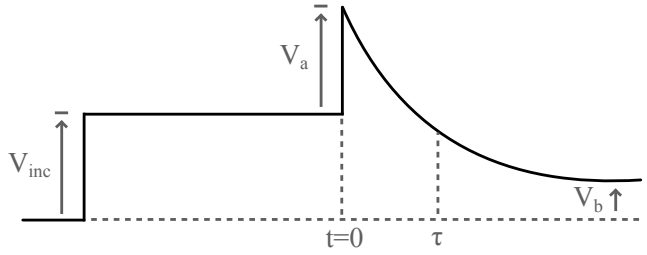

Figure 3.4: *A typical waveform resulting from an inductive load.*

To simplify calculations, t is set to 0 at the start of the reflection. The exponentially decaying waveform is an indicator the load has inductive reactance.

Series R-L Load

If $V_a = V_{inc}$, then $Z_L(t = 0) \rightarrow \infty$ and so the load may only contain series elements as depicted in figure 3.5. The value of V_b is approximated at the level where the exponential flattens out (inductor is low impedance) and corresponds to the resistive element R_s of the load.

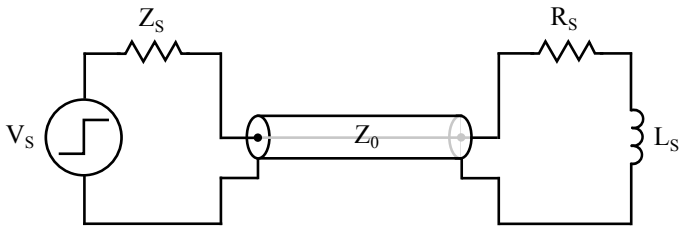

Figure 3.5: *A series R-L load attached to a transmission line.*

Substitution of R_s into equation 2.8 yields

$$\frac{V_b - V_{inc}}{V_{inc}} = \frac{R_s - Z_0}{R_s + Z_0} \tag{3.3}$$

Rearranging for V_b gives

$$V_b = V_{inc}\left(\frac{R_s - Z_0}{R_s + Z_0} + 1\right) \tag{3.4}$$

Solving for the series resistance R_s gives

$$R_s = Z_0 \frac{V_b/V_{inc}}{2 - V_b/V_{inc}} \tag{3.5}$$

The series inductance L_s can be determined by measuring the time constant τ_s. The voltage across the series circuit at $t \geq 0$ is

$$V_{RL} = V_b + (V_{inc} + V_a - V_b)e^{\frac{-t}{\tau}} \tag{3.6}$$

For the series circuit in figure 3.5, the time constant is

$$\tau_s = \frac{L_s}{R_s + Z_0} \tag{3.7}$$

and so the series inductance L_s is just

$$L_s = \tau_s(R_s + Z_0) \tag{3.8}$$

Parallel R-L Load

If $V_a < V_{inc}$, then $Z_L(t = 0)$ is finite and so the load must contain shunt elements as shown in figure 3.6. Also as $t \to \infty$, the inductor acts as a short circuit and so $V_b \to 0$.

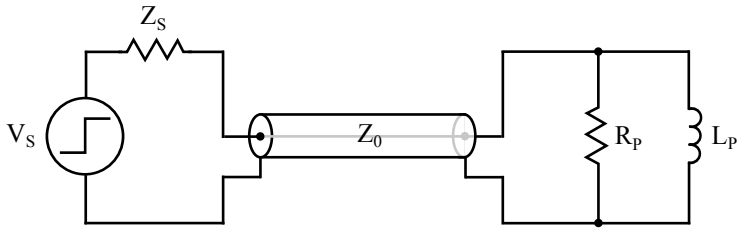

Figure 3.6: *A parallel R-L load attached to a transmission line.*

The value of V_a corresponds to the value of R_p by

$$V_a = V_{inc}\frac{R_p - Z_0}{R_p + Z_0} \tag{3.9}$$

Solving for the parallel resistance R_p gives

$$R_p = Z_0\frac{1 + V_a/V_{inc}}{1 - V_a/V_{inc}} \tag{3.10}$$

The voltage across the inductor at $t \geq 0$ is

$$V_L = (V_{inc} + V_a)e^{\frac{-t}{\tau}} \tag{3.11}$$

For the circuit in figure 3.6, the time constant is

$$\tau_p = \frac{L_p}{R_p \parallel Z_0} = \frac{L_p(R_p + Z_0)}{R_p Z_0} \tag{3.12}$$

and so the parallel inductance L_p is just

$$L_p = \frac{\tau_p R_p Z_0}{R_p + Z_0} \tag{3.13}$$

3.4.2 Example Waveform: Capacitive Load

Figure 3.4 is another example of a typical waveform resulting from a complex load. The waveform exhibits a charging exponential; an indicator the load has capacitive reactance.

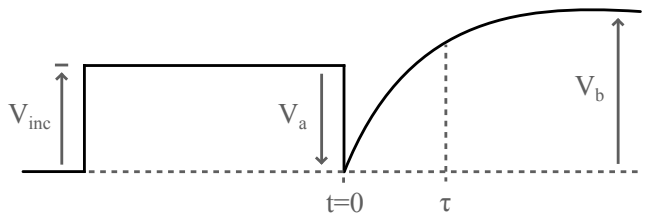

Figure 3.7: *A typical waveform resulting from a capacitive load.*

Series R-C Load

If $V_a > -V_{inc}$, then $Z_L(t{=}0) > 0$ and so the load must contain series elements as shown in figure 3.8. Also as $t \to \infty$, the capacitor acts as an open circuit

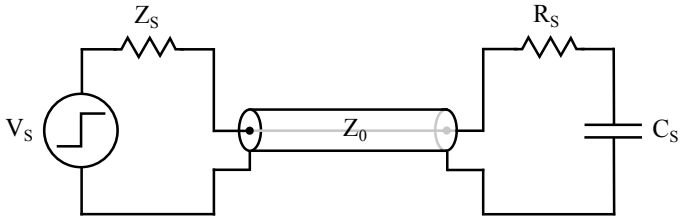

Figure 3.8: *A series R-C load attached to a transmission line.*

and so $V_b \to 2V_{inc}$. The value of V_a corresponds to the value of R_s by

$$V_a = V_{inc}\frac{R_s - Z_0}{R_s + Z_0} \tag{3.14}$$

Solving for the series resistance R_s gives

$$R_s = Z_0\frac{1 + V_a/V_{inc}}{1 - V_a/V_{inc}} \tag{3.15}$$

The series capacitance C_s can be determined by measuring the time constant τ_s. The voltage across the series circuit at $t \geq 0$ is

$$V_{RC} = V_{inc} + V_a + (V_b - V_a - V_{inc})(1 - e^{\frac{-t}{\tau}}) \tag{3.16}$$

For the series circuit in figure 3.6, the time constant is

$$\tau_s = (R_s + Z_0)C_s \tag{3.17}$$

and so the series capacitance C_s is just

$$C_s = \frac{\tau_s}{R_s + Z_0} \tag{3.18}$$

Parallel R-C Load

If $V_a = -V_{inc}$, then $Z_L(t = 0) = 0$ and so the load must contain a shunt capacitance as depicted in figure 3.9. The value of V_b is approximated at the

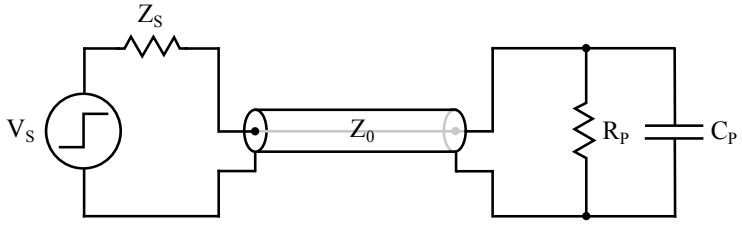

Figure 3.9: *A parallel R-C load attached to a transmission line.*

level where the exponential flattens out (capacitor is high impedance) and corresponds to the resistive element R_p of the load. V_b is just

$$V_b = V_{inc}\left(\frac{R_p - Z_0}{R_p + Z_0} + 1\right) \tag{3.19}$$

The parallel resistance R_p is

$$R_p = Z_0 \frac{V_b/V_{inc}}{2 - V_b/V_{inc}} \tag{3.20}$$

The voltage across the capacitor at $t \geq 0$ is

$$V_C = V_b(1 - e^{\frac{-t}{\tau}}) \tag{3.21}$$

For the circuit in figure 3.9, the time constant is

$$\tau_p = (R_p \parallel Z_0)C_p = \frac{R_p C_p Z_0}{R_p + Z_0} \tag{3.22}$$

and so the parallel capacitance C_p is just

$$C_p = \frac{\tau(R_p + Z_0)}{R_p Z_0} \tag{3.23}$$

Chapter 4

Time-Domain Reflectometry Applications

4.1 Overview

Besides the measurement of simple load impedances, TDR is also useful in other fields of application. A selection of applications found in recent literature are summarised below.

4.2 Characterisation of an Antenna

The input impedance of an antenna is traditionally measured in the frequency-domain with a vector network analyser (VNA) [29]. The VNA performs a frequency sweep of a sinusoidal test-signal to the antenna-under-test, monitoring the forward and reverse travelling waves and computing the complex reflection coefficient Γ as a function of frequency [30]. High accuracy in the characterisation of microwave devices can be achieved, however for antennas, an anechoic chamber is necessary to prevent interference from parasitic reflections and outside noise [31]. Such a facility is expensive and often impractical in most cases.

Microwave devices can also be characterised using a TDR. To transform the time-domain measurements into the frequency-domain, a computer is necessary to window the measured data, along with pre-processing algorithms and the discrete Fourier transform (DFT). Manufacturers of modern TDRs often provide supplementary software packages that compute the frequency-domain parameters directly [3]–[5].

A TDR is generally less expensive than a VNA [32], and since the energy in the test signal is localised, the effect from discontinuities such as connectors can be removed through time windowing [31]. For the measurement of antennas, TDR is especially advantageous. Time windowing facilitates the exclusion of parasitic reflections prior to frequency-domain transformation, hence eliminating the need for an expensive anechoic chamber [33].

4.2.1 Acquisition in the Time-Domain

For a linear time-invariant device such as a passive antenna, the system response $y(t)$ is defined as the convolution of the DUT response $h(t)$ and the input excitation signal $x(t)$ [34]:

$$y(t) = h(t) * x(t) \tag{4.1}$$

where "$*$" denotes the convolution operation. $y(t)$ and $x(t)$ are measurable quantities and can be used to determine the DUT time-domain response $h(t)$. Computation of the DUT frequency-domain response $H(j\omega)$ is achieved through the discrete Fourier transform (DFT).

System Response $y(t)$

When a voltage step containing multiple harmonics is incident on an antenna, a portion of energy corresponding to the system response will reflect back toward the source, while another portion of energy will radiate away from the antenna into space. Nearby objects can interfere with the measured system response by reflecting electromagnetic energy back toward the antenna as shown in figure 4.1.

The time t_l between the departure of the voltage step at the TDR to the arrival

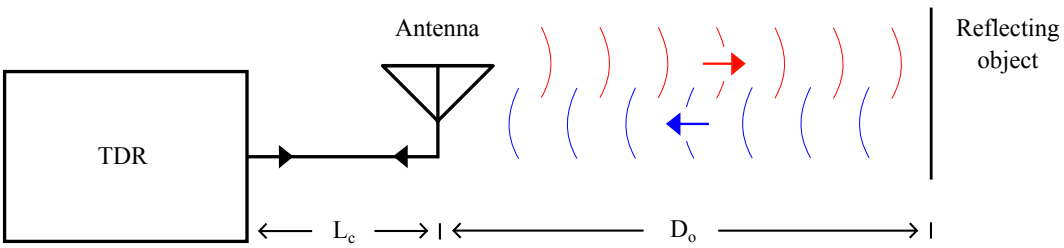

Figure 4.1: *Spurious reflections from a nearby object will interfere with the measured system response.*

of the antenna reflection at the TDR is found by rearranging equation 3.2:

$$t_l = \frac{2L_c}{v_p} \tag{4.2}$$

Similarly, the travel time t_0 for an electromagnetic wave to propagate to and from an object in free space is given by

$$t_0 = \frac{2D_0}{c} \tag{4.3}$$

where D_0 is the distance from the antenna to the nearest reflecting object. A typical waveform reflected by an antenna is shown in figure 4.2.

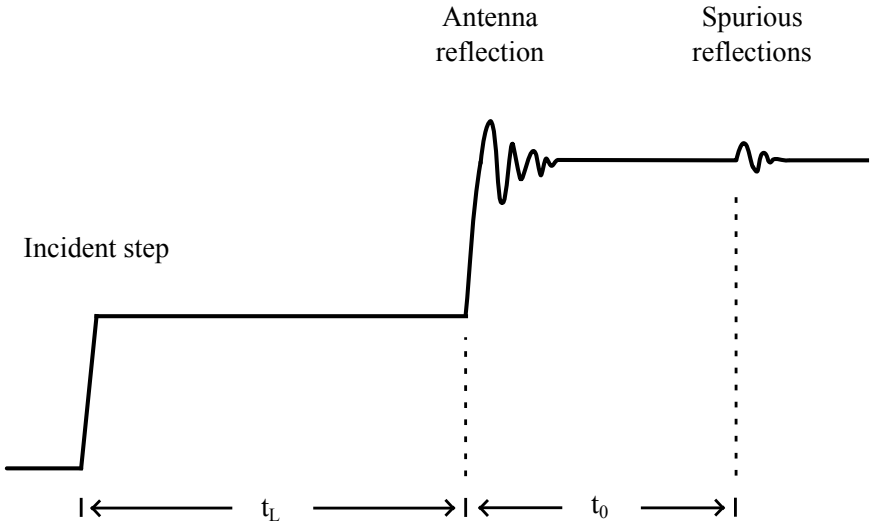

Figure 4.2: *A typical waveform to be expected when measuring an antenna.*

The portion of the waveform containing the antenna reflection must be windowed with a gating function to exclude the incident voltage step and spurious reflections contained in the measurement [33]. The gating function, also known as a Dirichlet window, multiplies the time-domain response by a value of one over the region of interest, and zero outside of the region [35]. The region of interest is shaded in figure 4.3. Exclusion of the incident step and cable delay from the time window, results in a reference plane extended to the end of the cable.

The minimum window time must be at least enough to allow the antenna reflection to settle to a steady-state before ending [36]. This ensures that no information is lost regarding the antenna response. The settling time will vary between antennas and so must be determined through measurement.

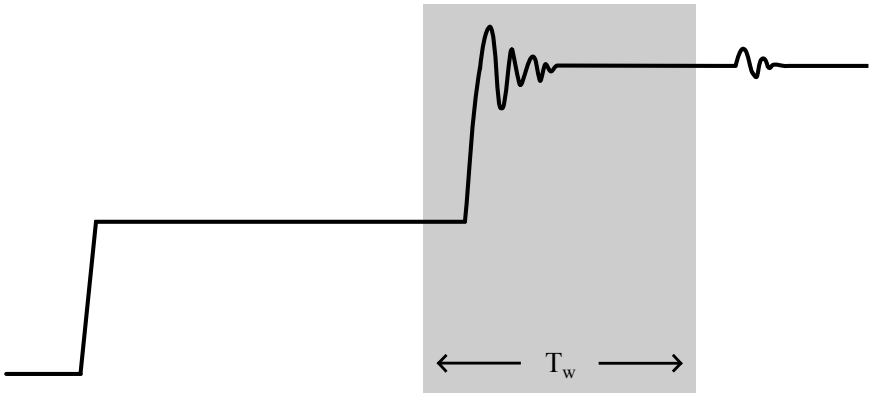

Figure 4.3: *A Dirichlet window is applied to the waveform to exclude the incident step and spurious reflections.*

The maximum window time T_w to exclude unwanted spurious reflections can be computed by

$$T_w = 2\left(\frac{L}{v_p} + \frac{D_0}{c}\right) \tag{4.4}$$

where L is a small portion of cable included in the measurement window that is necessary for subsequent frequency-domain transformation [33], [37].

The Incident Signal $x(t)$

The incident signal $x(t)$ is measured as the reflection produced by a short-circuit ($\Gamma = -1$) connected at the reference plane (in place of the antenna). Alternatively, an open-circuit ($\Gamma = +1$) can be measured but the effects of electromagnetic fringing cause the reflection coefficient to deviate away from $+1$ thus reducing the reliability of the measurement [38]. The measurement must adhere to the same time windowing parameters as used in the measurement of the system response $y(t)$.

Number of Points and Averaging

The sampling interval Δt needs to be small enough to adequately capture the rise time of the incident and reflected signals [39]. As described by equation 1.4, increasing the record length (number of points N) for a given time window reduces Δt and therefore improves accuracy of the measurement. Averaging of the measurements will also improve accuracy by reducing the effect of random noise [39] and extending the dynamic range [40]. However, as a consequence the time required to obtain N points increases.

4.2.2 Pre-Processing: Nicolson Algorithm

The DFT is an algorithm that transforms discrete time-domain signals into the frequency-domain. It considers the signal to be periodic, where the last sample of the period is the first sample in the subsequent period [41]. A problem arises when the start and end samples differ in amplitude, as is the case for the windowed signal in figure 4.3. This causes the DFT to process a truncated signal as shown in figure 4.4.

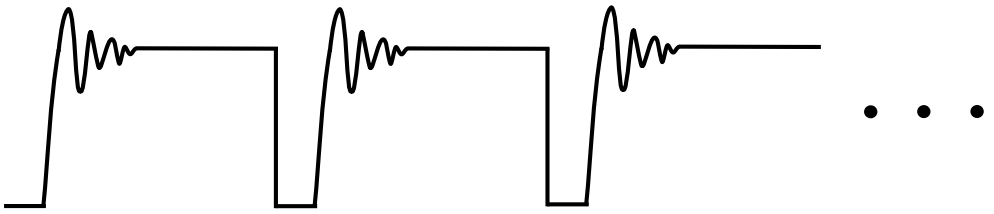

Figure 4.4: *Application of the DFT causes truncation error in the original signal.*

Truncation error produces spectral leakage in the frequency domain, a phenomenon where energy appears to leak out of the original spectrum and into other frequencies [42]. Numerous windowing techniques that aim to reduce spectral leakage are available, each with advantages and disadvantages. The well-known Nicolson algorithm is commonly used for dealing with step-like signals [33], [38], [43]. A linear ramp is subtracted from the original signal resulting in a waveform with start and end points equivalent to zero. The ramp function $r(i)$ is defined as

$$r(i) = f(0) + i\left(\frac{f(N-1) - f(0)}{N}\right), \qquad i = 0, \cdots, N-1 \tag{4.5}$$

where $f(i)$ represents the original signal. An example of a step-like signal is shown in figure 4.5(a). Figure 4.5(b) illustrates the effect of the Nicolson algorithm on the same waveform. A side effect of the Nicolson algorithm is the loss of dc information. Needless to say, for the measurement of microwave devices, dc information is often redundant anyway.

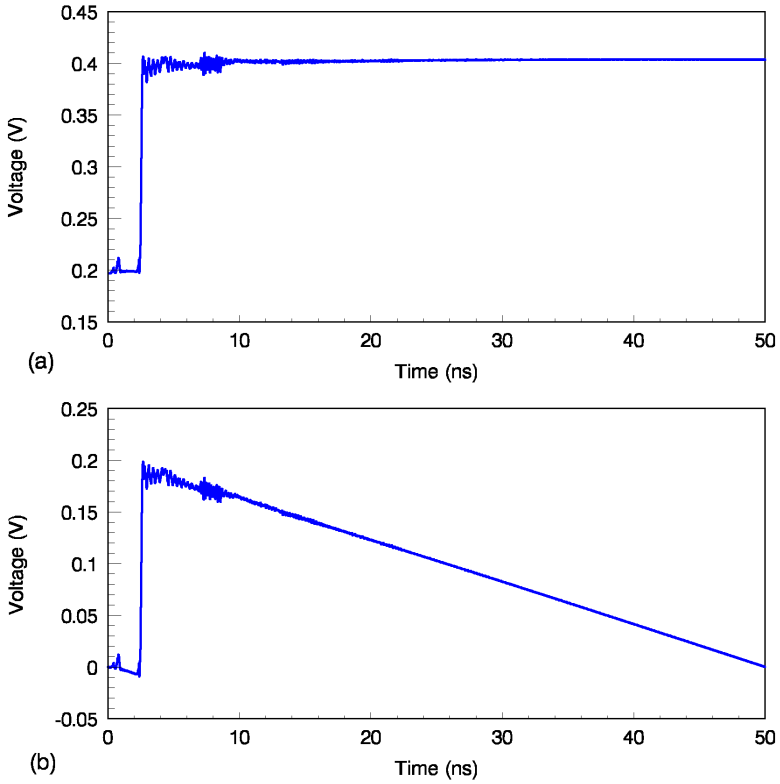

Figure 4.5: *(a) An example of a waveform reflected by an antenna. (b) A linear ramp is subtracted from the original waveform, leaving the start and end points with zero amplitude.*

4.2.3 Pre-Processing: Zero Padding

As a consequence of the DFT, the resolution[1] of the frequency-domain transformation is governed by the length of the time window [38]:

$$\Delta f = \frac{1}{T_w} \tag{4.6}$$

To improve the resolution without having to increase the length of the time window, zero padding can be employed. Zero padding is the process of adding zero valued data samples to the end of a sampled signal [44]. Other than improving resolution, zero padding has no effect on the spectral content (provided the aforementioned Nicolson algorithm has been applied). The waveform from figure 4.5(b) is zero padded and is shown in figure 4.6.

[1]The Δf spacing between each frequency bin.

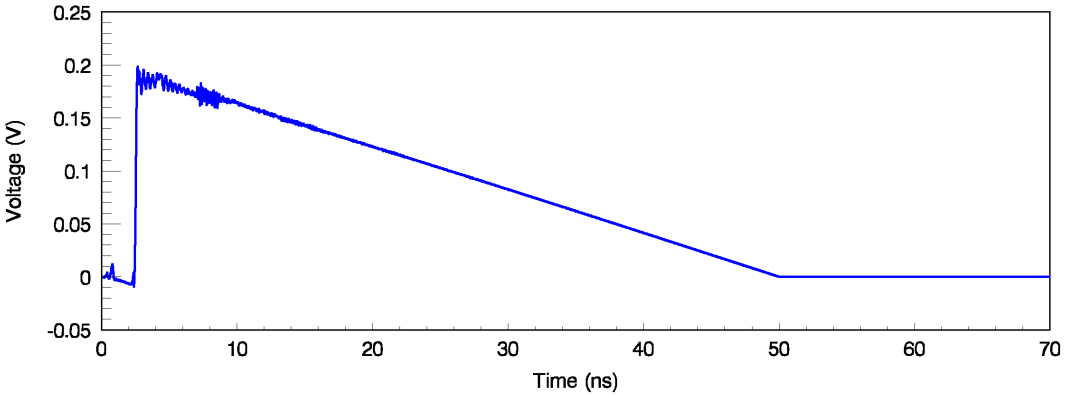

Figure 4.6: *Zero valued data samples are appended to the end of the waveform in order to improve resolution in the frequency-domain transformation.*

4.2.4 Frequency-Domain Transformation

As described by equation 4.1, the time-domain system response $y(t)$ is defined as the convolution of the DUT response $h(t)$ and the input excitation signal $x(t)$. In the frequency-domain, convolution transforms into multiplication [34]:

$$Y(j\omega) = H(j\omega)X(j\omega) \tag{4.7}$$

where $Y(j\omega)$, $H(j\omega)$, and $X(j\omega)$ denote the frequency-domain forms of $y(t)$, $h(t)$, and $x(t)$ respectively. The DUT response $H(j\omega)$ is also commonly referred to as the reflection scattering parameter $S_{11}(j\omega)$ or the reflection coefficient $\Gamma(j\omega)$. Therefore the antenna response in the frequency-domain is

$$S_{11}(j\omega) = \frac{Y(j\omega)}{X(j\omega)} \tag{4.8}$$

where the frequency-domain responses are computed from the DFT of each windowed and padded time-domain waveform:

$$Y(j\omega) = \mathrm{DFT}[y(t)] \tag{4.9}$$

$$X(j\omega) = \mathrm{DFT}[x(t)] \tag{4.10}$$

Finally, the antenna impedance $Z_{DUT}(j\omega)$ is computed by

$$Z_{DUT}(j\omega) = Z_0 \frac{1 + S_{11}(j\omega)}{1 - S_{11}(j\omega)} \tag{4.11}$$

It is important to mention that for small values of $Y(j\omega)$ and $X(j\omega)$, any small error can cause significantly large error in the result of equation 4.8. This limits

the system bandwidth to frequencies where sufficient energy is available in the input excitation signal [34].

4.2.5 Bandwidth

According to [45], the 3 dB bandwidth of the TDR system[2] can be approximated by

$$BW = \frac{0.35}{t_r} \tag{4.12}$$

where t_r is the overall system rise time. t_r can be approximated[3] as the combined rise times of the sampling oscilloscope t_{scope} and the step generator t_{gen} [46]:

$$t_r = \sqrt{t_{scope}^2 + t_{gen}^2} \tag{4.13}$$

The sampling period Δt should be small enough to capture at least five samples on the fastest transition as recommended by [38]:

$$\Delta t < \frac{t_r}{5} \tag{4.14}$$

4.3 Characterisation of Transmission Lines

Low-loss transmission lines are imperative to ensure adequate SNR in high-speed digital systems [32]. Impedance matching is also crucial. Reflections due to a discontinuity in impedance can cause pulses to coincide with subsequent pulses, leaving them indistinguishable from one another–a phenomenon also known as inter-symbol interference (ISI) [47].

Transmission lines can be characterised with a TDR. By using the method described in section 3.4, analysis of the reflection produced by the device under test (DUT) will yield an equivalent circuit and values for "lossy" components.

4.3.1 Root Impulse Energy Method

An alternative approach is described in [45] where transmission line loss is measured with the Root Impulse Energy (RIE) method. It requires measurement of the voltage reflections produced by two identical transmission lines, each with different lengths l_{long} and l_{short}, terminated with open-circuits. The

[2] It is assumed the TDR has a Gaussian response.
[3] The calculation does not take into account the effect from cables and connectors.

RIE (E) is then computed for each voltage waveform $V(t)$ by

$$E = \sqrt{\int \left(\frac{d}{dt}V(t)\right)^2 dt} \tag{4.15}$$

The formula includes the derivative of $V(t)$ (the reflected step), which is in fact the impulse response [48]. The impulse response is preferable over the step response as it encompasses a much wider bandwidth [49].

The loss per unit length Λ_{dB} is proportional to the ratio of the RIE computed for each transmission line[4]:

$$\Lambda_{\mathrm{dB}} = \frac{1}{2(l_{long} - l_{short})} 20 \log_{10} \left(\frac{E_{long}}{E_{short}}\right) \tag{4.16}$$

4.3.2 Capacitance Extraction

Another application of TDR is described in [50] where TDR is used to measure the capacitance of interconnect structures in CMOS devices. It involves acquisition of the reflection produced by the DUT as well as the reflection from an open-circuit, followed by computation of the integral:

$$C = \frac{1}{2Z_0 V_s} \int \left(V_{open}(t) - V_{DUT}(t)\right) dt \tag{4.17}$$

where $V_{open}(t)$ is the reflection from an open-circuit, $V_{DUT}(t)$ is the reflection from the DUT, and V_s is the amplitude of the incident voltage step. Although limited to the measurement of capacitance, complicated analysis as required by the aforementioned method is avoided.

4.4 Measurement of the Dielectric Properties of Materials

A dielectric is a non-conductive material that becomes polarised when an electric field is applied [51]. Typical applications include capacitors, transmission lines, and piezoelectric devices. Measurement of the material's ability to store and dissipate energy can yield intrinsic properties unique to that material. For example, water has a high permittivity relative to most other materials,

[4]The formula takes into account that a pulse will propagate through a length of cable twice before arriving at the oscilloscope.

making it easy to detect with electromagnetic waves. For this reason dielectric measurements are useful for the evaluation of moisture content in porous material such as soil [52], [53] and food [54], [55].

In [56], a method is described to measure the complex permittivity ϵ and permeability μ of a material as a function of frequency. The test set-up employs a TDR to transmit a pulse through a coaxial cable and into a coaxial line filled with the material under test. The end of the coaxial line is attached to a short length of coaxial cable terminated with a short-circuit.

The acquisition of four different reflections is necessary for determining the dielectric properties:

(i) a reflection $V_{inc1}(t - t_0)$ from a short-circuit connected in place of the coaxial line;

(ii) a reflection $V_A(t - t_0)$ with the coaxial line and material under test inserted;

(iii) a reflection $V_{inc2}(t - t_1)$ with an empty coaxial line, resulting from the short-circuit connected at the end of the cable;

(iv) a reflection $V_B(t - t_1)$ with the coaxial line and material under test inserted.

Each reflection is windowed in time to exclude all other reflections from the acquisition. The Fourier transform is then computed for each windowed reflection and the S-parameters are derived. A 1-port measurement would normally reveal only the reflection scattering parameter $S_{11}(f)$, however, time windowing has allowed measurement of the doubly-transmitted signal to give $S_{21}^2(f)$. The permittivity and permeability are then derived from the S-parameters.

Chapter 5

Impulse TDR

5.1 Overview

All aforementioned applications of TDR employ a voltage step as the stimulus signal. As a consequence of the Fourier transform, the energy in the spectrum of a voltage step falls with increasing frequency. For the measurement of band-pass microwave devices, most of the energy in the step is wasted and so the dynamic range becomes limited.

On the other hand, an ideal impulse (Dirac delta) test signal has a theoretically flat bandwidth where energy is evenly distributed over all frequencies. In this chapter the advantages of making impulse TDR measurements are explored where the stimulus signal is impulse-like rather than step-like as used in conventional TDR.

5.2 Time-Domain Comparisons to Step TDR

Figure 5.1 illustrates a variety of simulated waveforms for common load conditions on a characteristic line impedance, Z_0, in the well-known case of a TDR built using a step stimulus signal, compared with the case of an impulse stimulus signal. The waveforms contain the incident stimulus signal that is applied to the load impedance, Z_L, followed by a signal reflected back to the TDR. The waveforms in the middle column of the figure should be familiar as were discussed in chapter 3. In the right-hand column, in the case of the impulse reflected by the resistive load, the waveform is as one would expect–a change in amplitude according to the level of mismatch. However, in the case of the impulse signal incident upon a complex load, the reflected waveform is neither

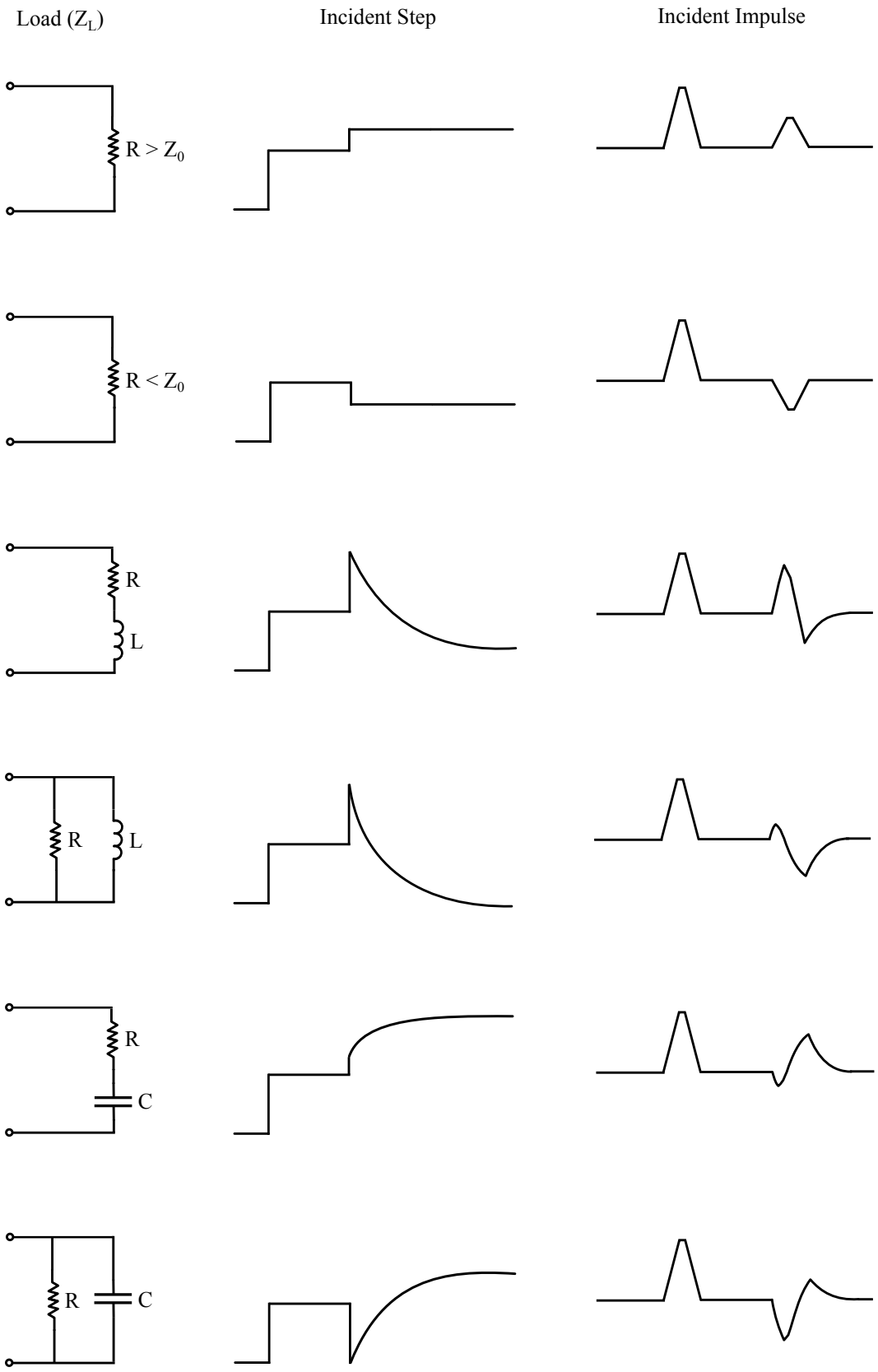

Figure 5.1: *Comparison of visual displays to be expected for a variety of common load circuits in the case of conventional step TDR and the proposed impulse TDR.*

familiar nor obvious. This difference occurs because in the step case there is more emphasis on energy at low frequencies, resulting in waveforms that resemble the classic transient response waveforms for R-C and R-L circuits. For this reason, impulse TDR is not likely to replace step TDR in the analysis of simple discontinuities on a transmission line.

5.3 Fourier Transform of the Stimulus Signal

5.3.1 Ideal Impulse

The unit impulse (Dirac delta) function in figure 5.2(a) is defined as having zero amplitude for all time except at $t = 0$, where it has infinite amplitude [10]:

$$\delta(t) = \begin{cases} 0, & t \neq 0 \\ \infty, & t = 0 \end{cases} \tag{5.1}$$

as well as containing unit area:

$$\int_{-\infty}^{\infty} \delta(t)\, dt = 1 \tag{5.2}$$

The Fourier transform of the unit impulse is

$$\mathrm{F}[\delta(t)] = 1 \tag{5.3}$$

Therefore, an ideal impulse has a flat frequency response as shown in figure 5.2(b). Although the unit impulse is a theoretical construct and cannot physically exist, it is used as a limiting case for when the width of a pulse approaches zero.

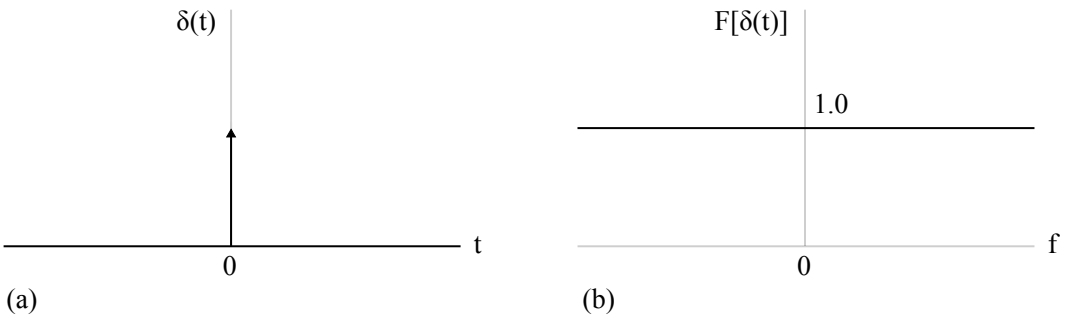

Figure 5.2: *(a) Dirac delta function in the time-domain. (b) Frequency spectrum of the Dirac delta function.*

5.3.2 Practical Impulse

Derived from the convolution of two rectangular ("rect") functions, the trapezoid function in figure 5.3 provides an approximation of a realistic impulse with finite rise and fall times [57]:

$$u(t) = \frac{1}{\tau}\,\mathrm{rect}\left(\frac{t}{\tau}\right) \otimes A\,\mathrm{rect}\left(\frac{t}{T}\right) \tag{5.4}$$

where T is the full width at half maximum (FWHM) and τ is the rise/fall time from 0 to 100% of the amplitude A. The Fourier transform of $u(t)$ is given by

$$\mathrm{F}[u(t)] = AT\,\mathrm{sinc}(f\tau)\,\mathrm{sinc}(fT) \tag{5.5}$$

where sinc is defined as:

$$\mathrm{sinc}(x) = \frac{\sin(\pi x)}{\pi x} \tag{5.6}$$

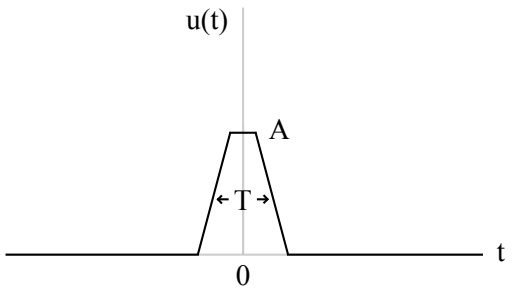

Figure 5.3: *The trapezoid function provides an approximation of a realistic impulse.*

5.3.3 Ideal Step

The Heaviside unit step function in figure 5.4(a) is defined as

$$H(t) = \begin{cases} 1, & t > 0 \\ \frac{1}{2}, & t = 0 \\ 0, & t < 0 \end{cases}$$

This function represents an ideal voltage step[1] which is immediately elevated to a constant level at a definite time [58]. The Fourier transform of $H(t)$ is given by

$$\mathrm{F}[H(t)] = \frac{1}{j2\pi f} + \frac{1}{2}\delta(f) \tag{5.7}$$

[1]Note the derivative of the Heaviside step is the Dirac delta [58].

The response is shown in figure 5.4(b). It varies as the reciprocal of frequency and so approaches zero amplitude as frequency tends to infinity. This theoretical construct cannot physically exist because a realistic step waveform has a finite rise time.

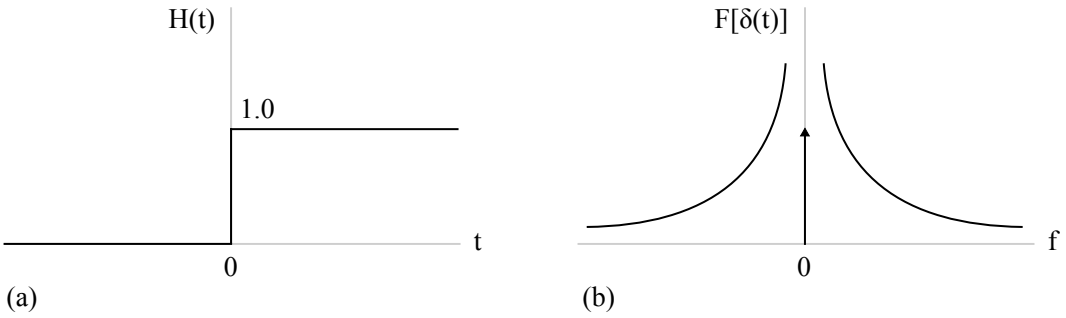

Figure 5.4: *(a) Unit step function in the time-domain. (b) Frequency spectrum of the unit step.*

5.3.4 Practical Step

The Fourier transform for the step function $s(t)$ with finite rise time in figure 5.5 is given by

$$\mathrm{F}[s(t)] = A\frac{1}{j2\pi f}\,\mathrm{sinc}(f\tau) \tag{5.8}$$

where τ is the rise time from 0 to 100% of the amplitude A.

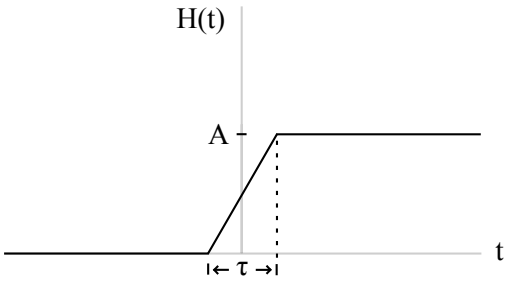

Figure 5.5: *A practical step with finite rise time.*

5.3.5 Spectra

The Agilent U9391C impulse generator produces impulses with a typical FWHM of 23 ps [59]. The rise/fall time from 0 to 100% of the amplitude is estimated as 18 ps (5 ps flat-top). By inserting these parameters into equation 5.5, the Fourier transform of a unit amplitude impulse was simulated in Matlab. Similarly, the Fourier transform of an ideal step (equation 5.7) and some realistic

step waveforms (equation 5.8) were simulated to be compared with the impulse. The spectra for each stimulus signal is shown in figure 5.6. It can be seen that even the realistic, limited impulse signal contains more energy than an ideal step for frequencies above about 7.5 GHz. When the step waveform is not ideal but similar to what is available today [3]–[5], the comparison becomes even more favorable, as can be seen in the same figure.

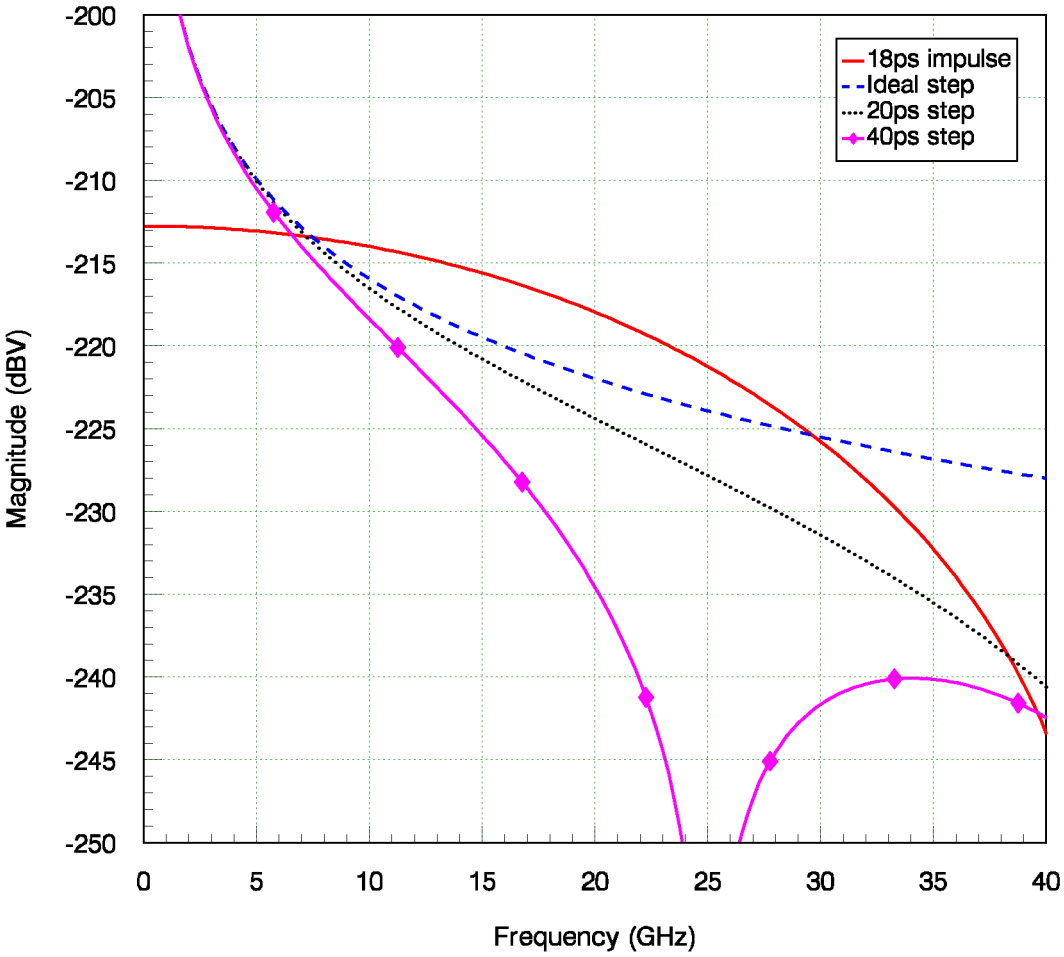

Figure 5.6: *The Fourier transforms of an ideal unit step, some practical step-like signals, and a practical trapezoidal pulse of unit amplitude. The unit for magnitude is dBV, namely the voltage relative to 1 Volt.*

5.4 Hardware

The schematic for an impulse-style TDR is shown in figure 5.7. The set-up features an Agilent U9391C impulse generator with a 23 ps pulse width [60]–[62], a 100 MHz RF source, a dc to 26.5 GHz power divider, and an 18 GHz TDR operating in oscilloscope mode.

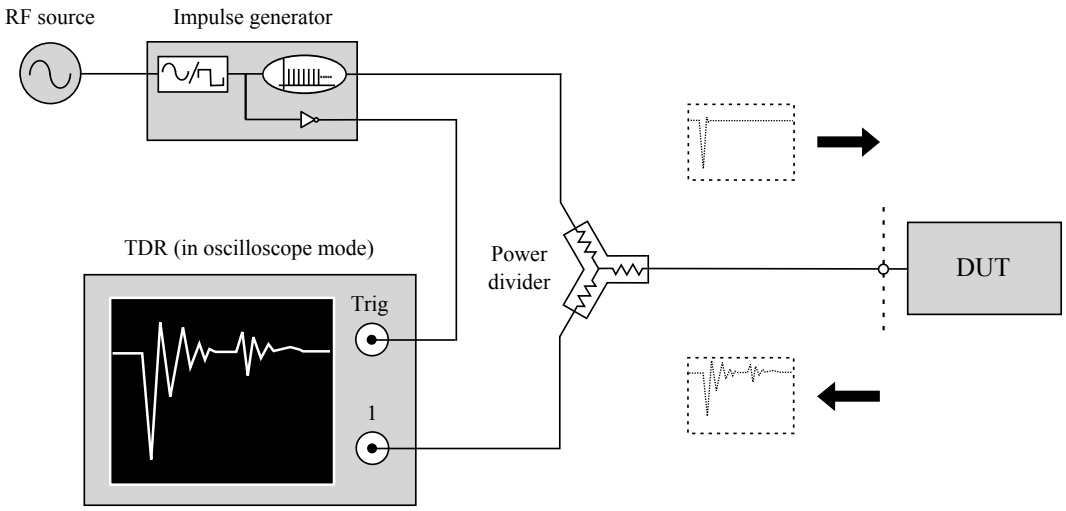

Figure 5.7: *An impulse TDR set-up for the measurement of microwave devices. A generated impulse is transferred to the DUT, resulting in a reflection that is monitored on the TDR. The dashed line represents the reference plane at the DUT connector.*

The impulse generator, also called a comb generator in frequency-domain parlance, produces a series of −400 mV impulses that are split between the DUT and oscilloscope via a resistive divider. The temporal spacing between each impulse is set by the frequency of the RF source and the generator's internal frequency divider [59]. When an impulse arrives at the DUT, unless the DUT has an impedance equivalent to the characteristic impedance of the system, the DUT will reflect a voltage signal back toward the resistive divider and into the oscilloscope to be measured. Due to high bandwidth requirements, an equivalent-time sampling oscilloscope is employed where triggering is supplied by an external signal from the impulse generator. A photograph of the impulse TDR set-up in the laboratory is shown in 5.8.

5.4.1 Component Losses

The cable connecting each component in figure 5.7 is 1.5 ft in length. Table 5.1 summarises the insertion loss expected at various frequencies of operation. A full list of specifications can be found in appendix F.

A generated impulse that is to be incident upon the DUT will pass through four lengths of cable before arriving at the oscilloscope. This results in a combined cable loss of approximately 4 dB at the highest rated frequency. A signal passing through the power divider will be split equally, leaving each

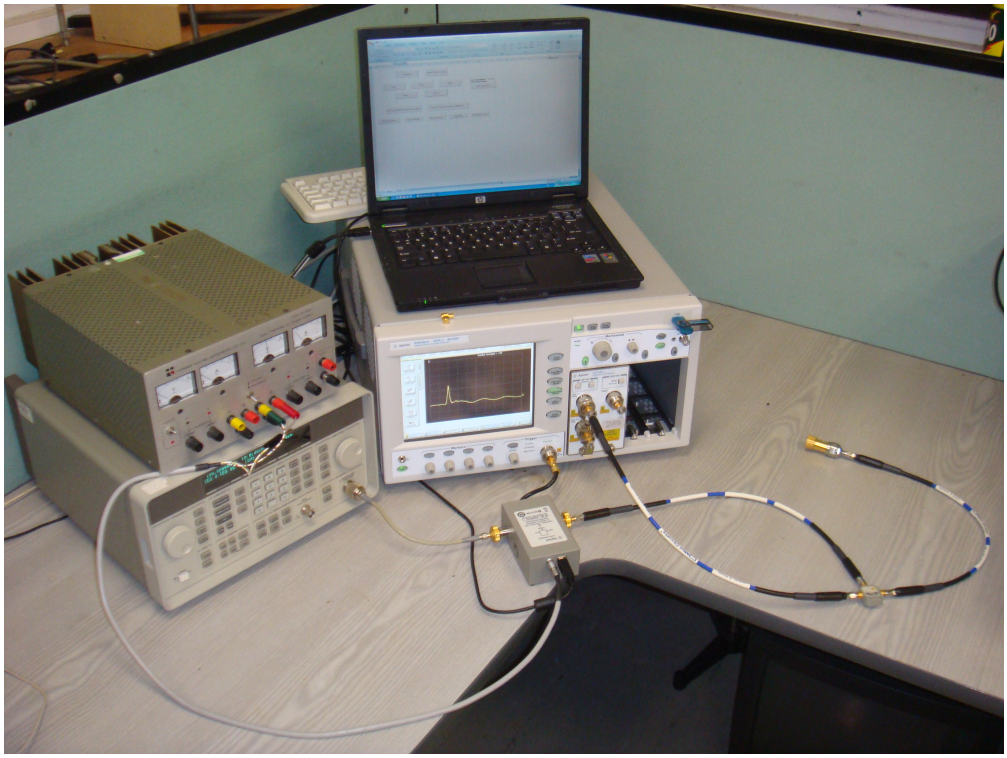

Figure 5.8: *The impulse TDR set-up in the laboratory. The impulse generator is supplied with +15VDC from a bench top power supply. A notebook PC is required to initiate the impulse generator and control the frequency divider.*

Table 5.1: *Typical insertion loss in a 1.5ft length of Mini-Circuits CBL-1.5FT-SMSM+ SMA cable.*

Frequency (GHz)	**dc–2.5**	**2.5–6.0**	**6.0–12.0**	**12.0–18.0**
Insertion Loss (dB)	0.25	0.4	0.7	1.0

output signal 6 dB down. The impulse will travel through the divider twice before arriving at the oscilloscope, adding 12 dB of attenuation. As a result of the combined cable and divider losses, the impulse will experience a minimum of 4 dB + 12 dB = 16 dB of attenuation (assuming the DUT has a $|\Gamma| = 1$).

5.4.2 System Rise Time

The impulse[2] as measured directly at the output of the generator is in figure 5.9. A magnified display of the same signal is shown in figure 5.10. The

[2]The impulse from the Agilent U9391C generator contains harmonics well beyond the 18 GHz bandwidth of the oscilloscope, making it impossible to display the full amplitude of the impulse. For this reason, the impulse in figure 5.9 attains only about 63% of its true amplitude. Simulations reveal that even a 190 GHz bandwidth system would report the impulse to be 95% of its true amplitude.

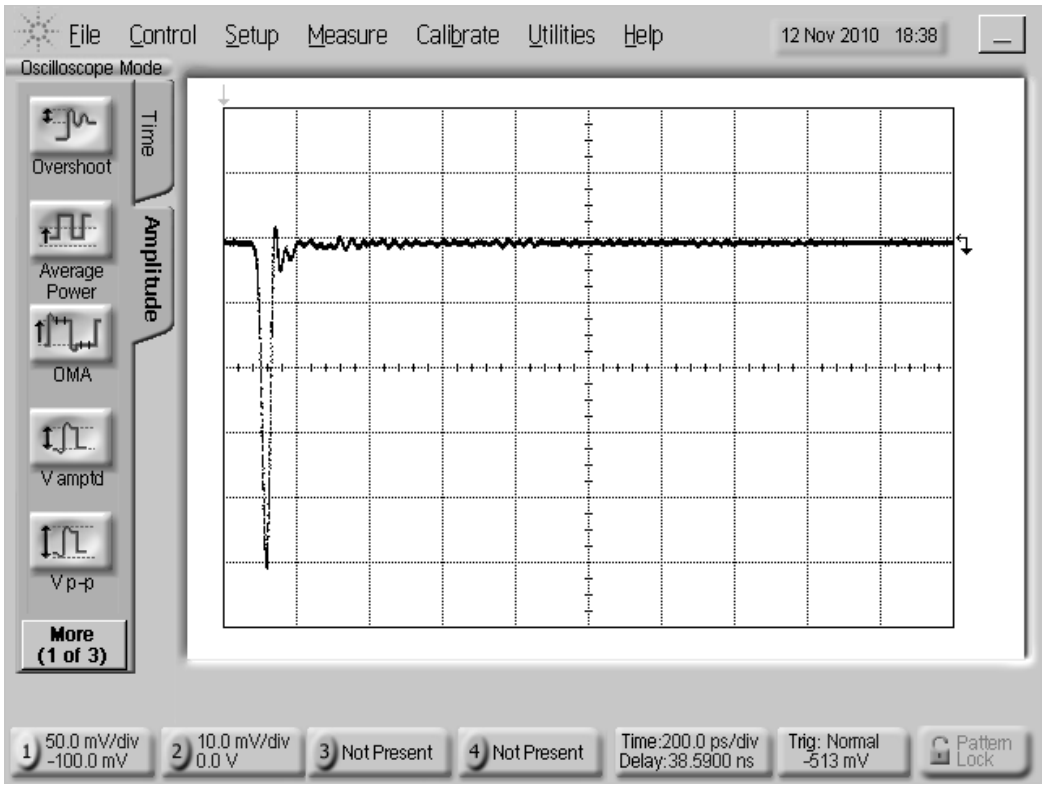

Figure 5.9: *A screen capture of an impulse produced by the Agilent U9391C generator as displayed on the oscilloscope.*

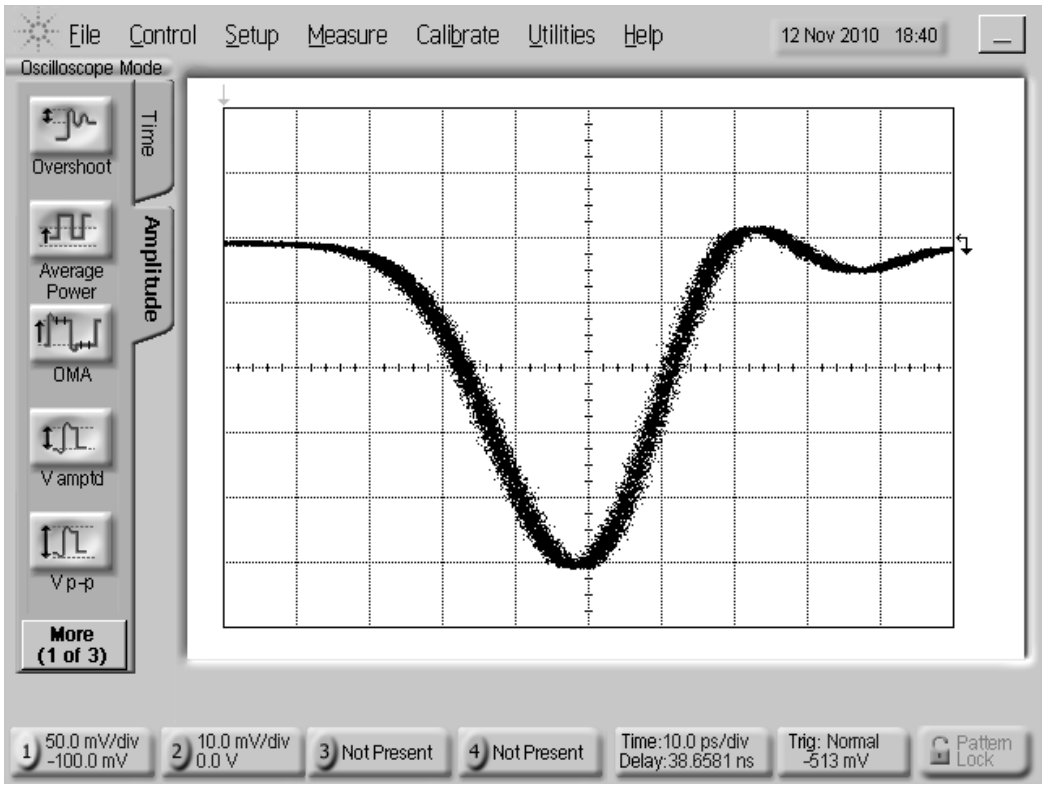

Figure 5.10: *A magnified view of the impulse as displayed on the oscilloscope. No averaging has been applied to remove jitter.*

measured rise time is 18 ps and the pulse width at FWHM is 24 ps. A plot of the impulse spectra can be found in appendix C.

Chapter 6

Impulse TDR: Characterisation of an Antenna

6.1 Overview

In chapter 4 the application of TDR to the measurement of antennas was discussed. It was shown through post-processing and transformation of time-domain data, an antenna could be characterised by the reflection scattering parameter $S_{11}(f)$ without the need of an anechoic chamber as required with VNA measurements.

The extra bandwidth gained with impulse TDR would be especially advantageous for the measurement of antennas, especially wideband and ultra-wideband (UWB) types. In this chapter, the performance of impulse TDR will be assessed through measurement of a wideband antenna. Comparisons will be made with measurements obtained using step TDR and a VNA.

6.2 Experimental Set-up

The DUT was a horizontally polarised wideband sector antenna intended for 802.11a applications. The manufacturer specifies an operating frequency range of 5.47-5.85 GHz with a 50 Ω nominal impedance [63]. Measurements were performed with the impulse TDR, step TDR, and VNA. A description of each test set-up follows.

6.2.1 Impulse TDR

A photograph of the equipment set-up to measure the antenna is shown in figure 6.1. The N-type connector at the reference plane was held secure with a heavy retort stand. This was to prevent unwanted effects from cable movement between each measurement procedure. In [33], the optimal time window to obtain highest accuracy in S_{11} was found to be between 30–35 ns. With this knowledge, the antenna was positioned according to equation 4.4 where no objects or walls were within 5.5 meters, allowing up to 40 ns worth of spurious-free reflections.

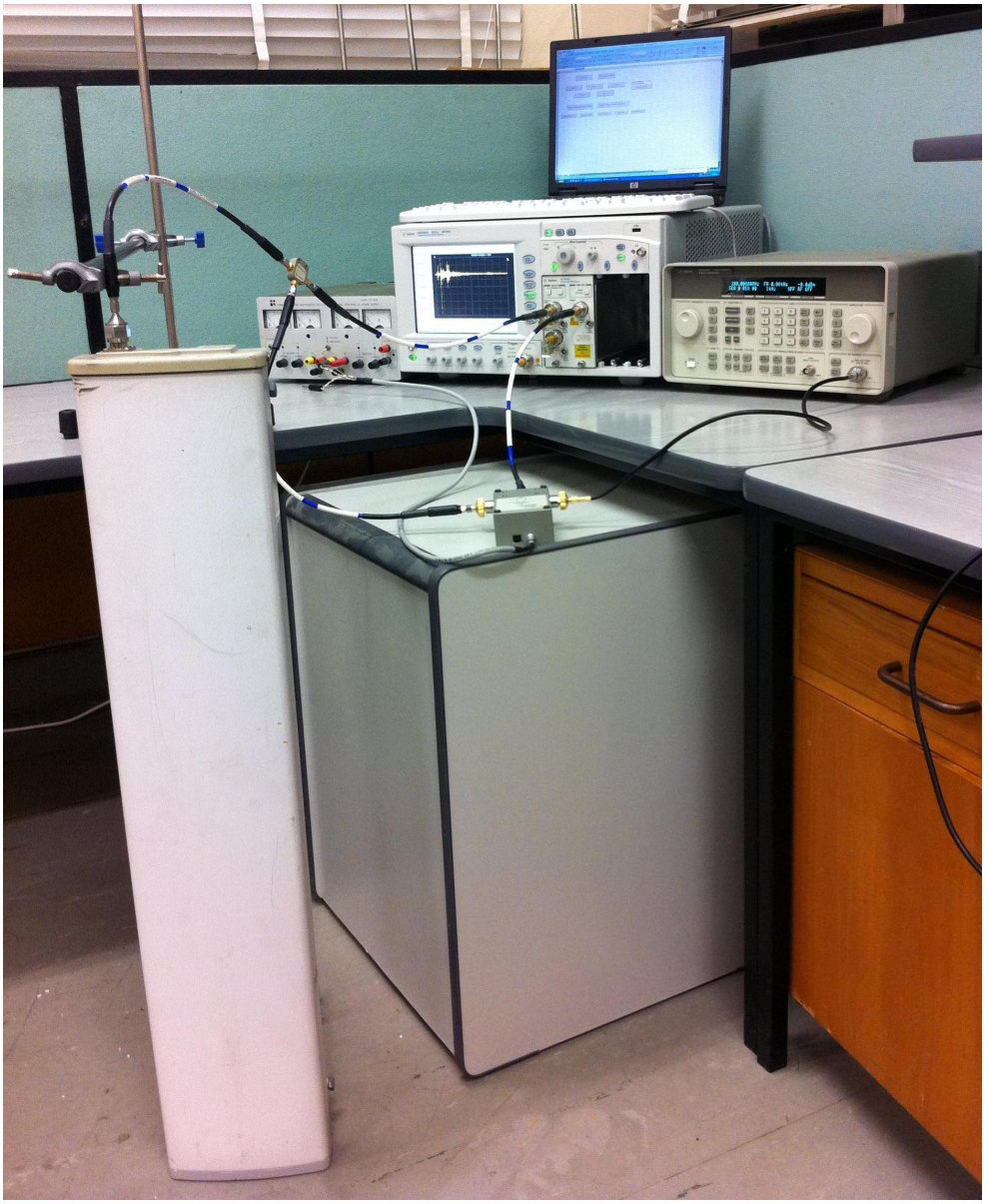

Figure 6.1: *The impulse TDR is set-up in the laboratory to perform measurements on the windband antenna.*

6.2.2 Step TDR

A step-type TDR was set-up with a similar configuration to figure 5.7 but with the impulse source replaced with a 50 Ω dummy load and the mainframe set in TDR mode. The simulus signal was provided by the TDR's internal step generator. A schematic of the step TDR is shown in figure 6.2. The power divider was included to replicate the conditions of the impulse TDR set-up so that fair comparisons between techniques could be made. A 2 dB attenuator was also inserted between the oscilloscope channel and the divider, to further reduce the step signal to a similar amplitude produced in the impulse TDR set-up. The combined rise time of the oscilloscope and step generator is rated as $t_r = 40$ ps [64].

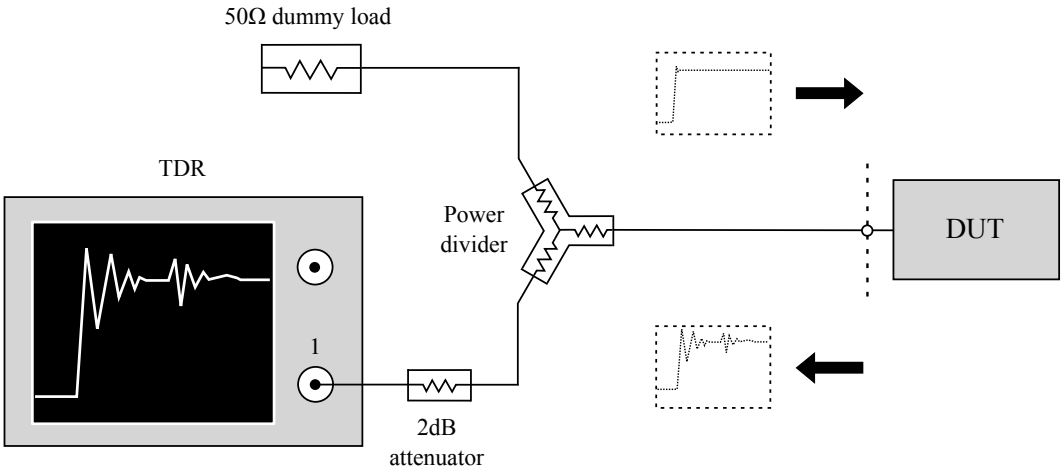

Figure 6.2: *The step TDR set-up. The power divider, dummy load, and attenuator are included to replicate the conditions of the impulse TDR set-up. The dashed line represents the reference plane at the DUT connector.*

6.2.3 VNA Reference

Calibrated measurements up to 9 GHz were acquired using a VNA, where the antenna was situated outdoors to simulate an anechoic-type environment. This provided an adequate reference measurement for comparison with the TDR measurements.

6.2.4 List of Equipment

A summary of the equipment employed in each measurement set-up is listed in table 6.1.

Table 6.1: *A list of the equipment employed in each measurement set-up.*

Type	Details	iTDR	TDR	VNA
Agilent U9391C impulse (comb) generator	10 MHz to 26.5 GHz	•		
Agilent 8648B signal generator	9 kHz to 2 GHz	•		
Agilent 11636B power divider	dc to 26.5 GHz, 7.5 dB IL	•	•	
Agilent 86100C oscilloscope mainframe	14-bit ADC, 16384 pts	•	•	
Agilent 54754A TDR module	2-CH 18 GHz, 200 mV step	•	•	
Laird SAH58-120-16-WB Antenna	5.47-5.85 GHz, 50 Ω	•	•	•
Mini-Cir. CBL-1.5FT-SMSM+ SMA Cable x5	dc to 18 GHz, 1 dB IL	•	•	•
Agilent 85032F Calibration Kit	dc to 9 GHz, Type-N	•	•	•
Mini-Cir. 2dB Attenuator SMA	dc to 18 GHz		•	
Agilent E8358A VNA	300 kHz to 9 GHz			•

6.3 Measurements of the Antenna

An antenna reference measurement was acquired over 2.5–9.0 GHz using the VNA. The magnitude of the reflection scattering parameter $|S_{11}(f)|_{\mathrm{dB}}$ is plotted in figure 6.3.

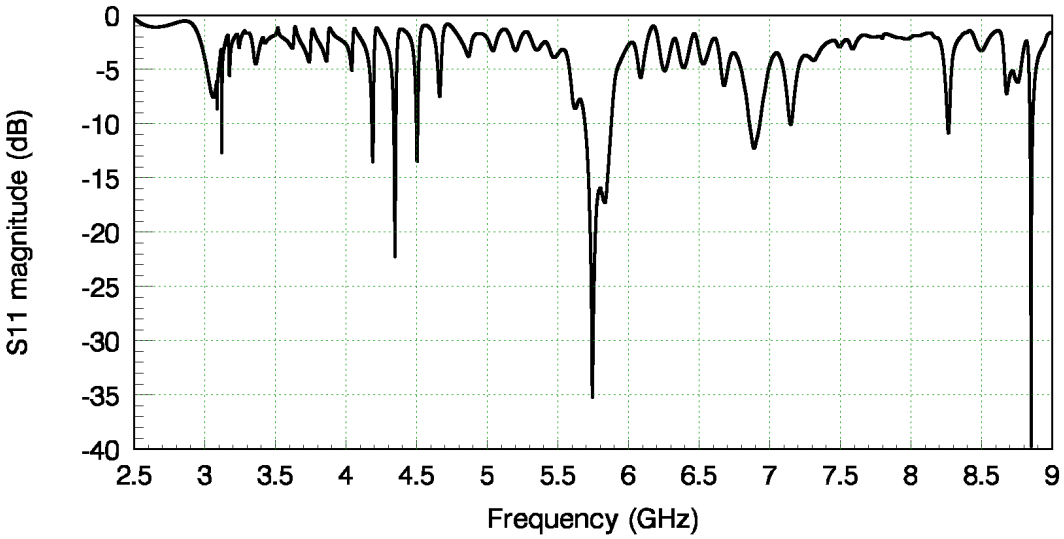

Figure 6.3: *A VNA reference measurement for the wideband antenna.*

The same measurement is shown in figure 6.4, but with the frequency axis limited to the working range of the antenna. The drop in magnitude between 5.59–5.90 GHz (−6 dB bandwidth) is where the antenna is radiating the most energy. This is somewhat outside of the specified operating range of 5.47–5.85 GHz.

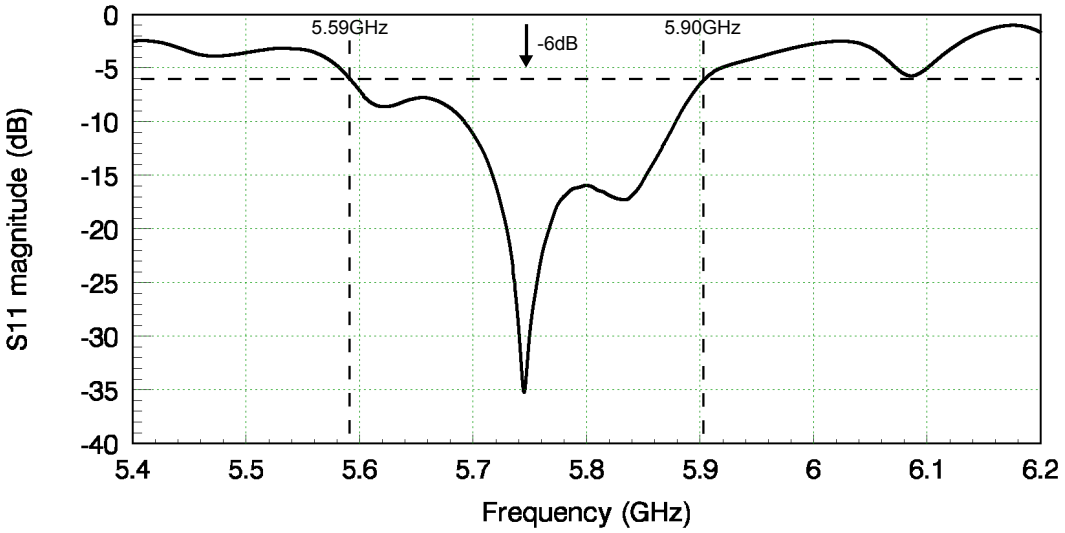

Figure 6.4: *A VNA reference measurement, limited to the working frequency range of the wideband antenna.*

6.3.1 Acquisition Using Impulse TDR

As discussed in chapter 4, two time-domain measurements are necessary for the subsequent frequency-domain processing: A reference waveform reflected from a short-circuit and the waveform reflected by the antenna. These measurements were acquired with the record length maximised to 16384 points over a 50 ns window to satisfy equation 4.14. The majority of the jitter and random noise visible on the oscilloscope display was minimised by averaging 1024 times.

Shown in figure 6.5(a) is the reference waveform derived from a short-circuit connected at the reference plane. The large spike corresponds to the reflected impulse (inverted in amplitude), followed by a small amount of oscillatory behaviour characteristic of the non-ideal short-circuit. The short-circuit was replaced with the wideband antenna and its reflection was measured as shown in figure 6.5(b). The first peak corresponds to the mismatch between the transmission line and the antenna connector. A feed cable within the antenna housing introduced a small delay prior to the actual antenna reflection. The next portion of the waveform corresponds to the resonant behaviour of the antenna.

With the Dirichlet window in Matlab, the acquired measurements were windowed with various lengths ranging from 15–50 ns. Each rectangular window contained the essential data that corresponded to the DUT response, and provided a reference plane extended to the end of the cable where the DUT was

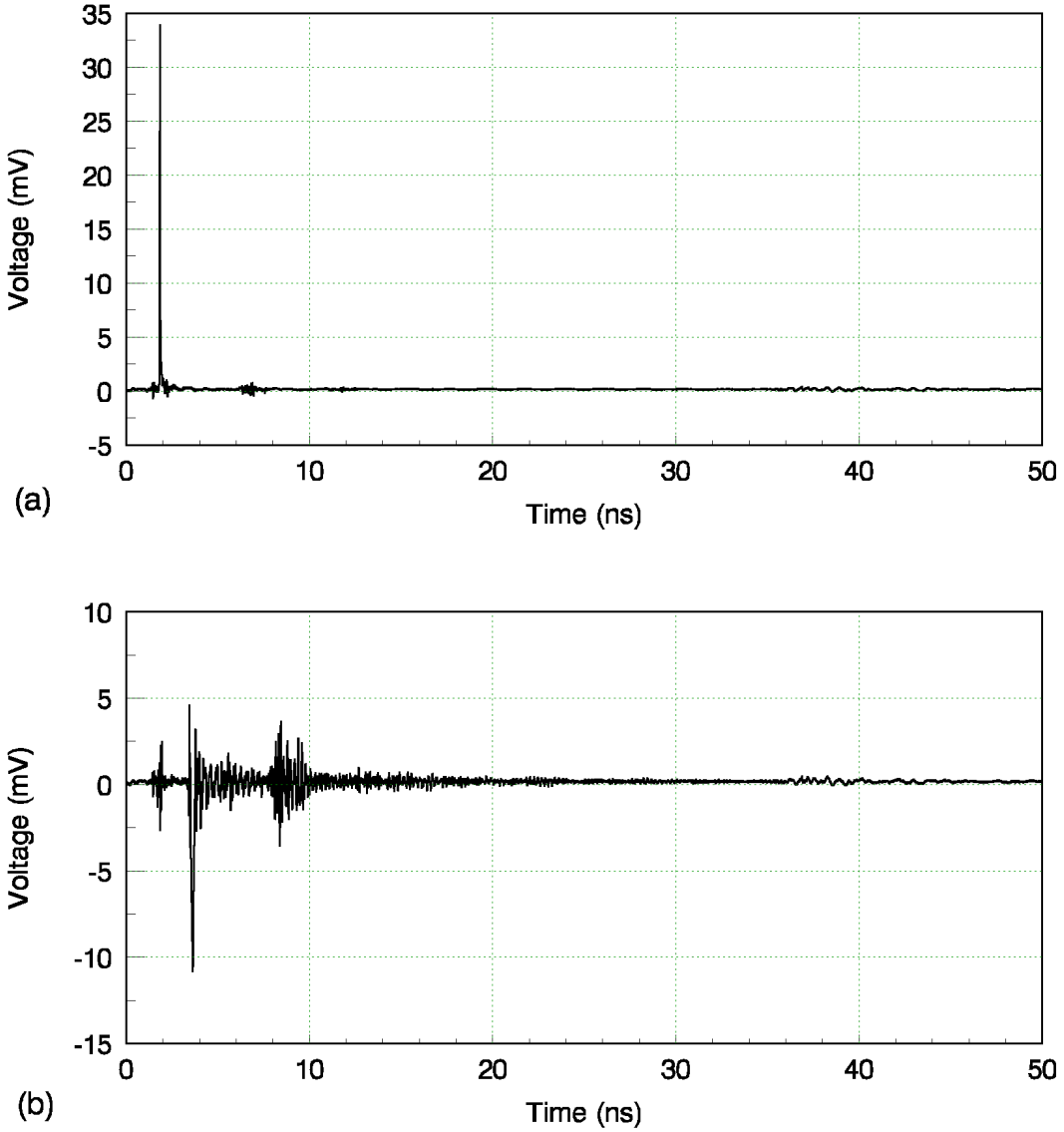

Figure 6.5: *Plot of the reflected signal seen by the impulse TDR when the (a) short-circuit is connected at the reference plane (b) wideband antenna is connected at the reference plane.*

to be attached. The purpose of obtaining multiple sets of data was to establish the optimal time window T_w subsequent to frequency-domain transformation.

6.3.2 Acquisition Using Step TDR

The same process was followed for the acquisition of the step-type TDR measurements. The reference reflection derived from a short-circuit connected at the reference plane is shown in figure 6.6(a). Similarly, the reflection from the wideband antenna connected at the reference plane is shown in figure 6.6(b).

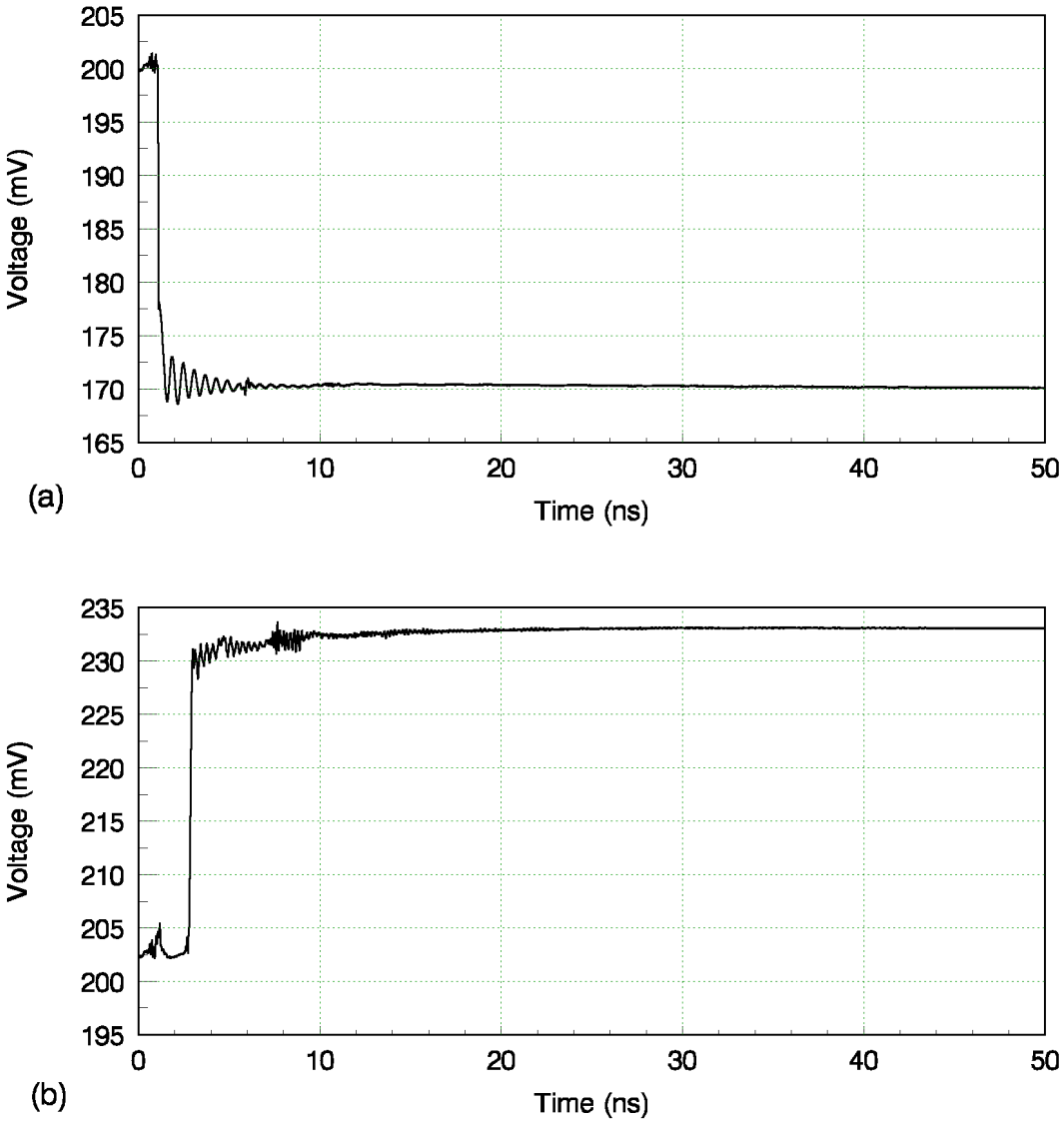

Figure 6.6: *Plot of the reflected signal seen by the step TDR when the (a) short-circuit is connected at the reference plane (b) wideband antenna is connected at the reference plane.*

6.3.3 Frequency-Domain Transformation

The time-domain data from the impulse TDR and step TDR was processed with the Nicolson algorithm to avoid truncation error, along with 200 ns of zero-padding to guarantee a frequency resolution of at least 5 MHz. The discrete Fourier transform (DFT) was computed for both the reference reflection and the DUT reflection, resulting in $V_{ref}(f)$ and $V_{DUT}(f)$ respectively. The reflection scattering parameter $S_{11}(f)$ was then computed with equation 4.8 for frequencies between 2.5-9.0 GHz. This was repeated for each of the 15–50 ns windowed data sets. In figure 6.7 a flow chart summarises the computer program necessary for processing the acquired data files from the oscilloscope

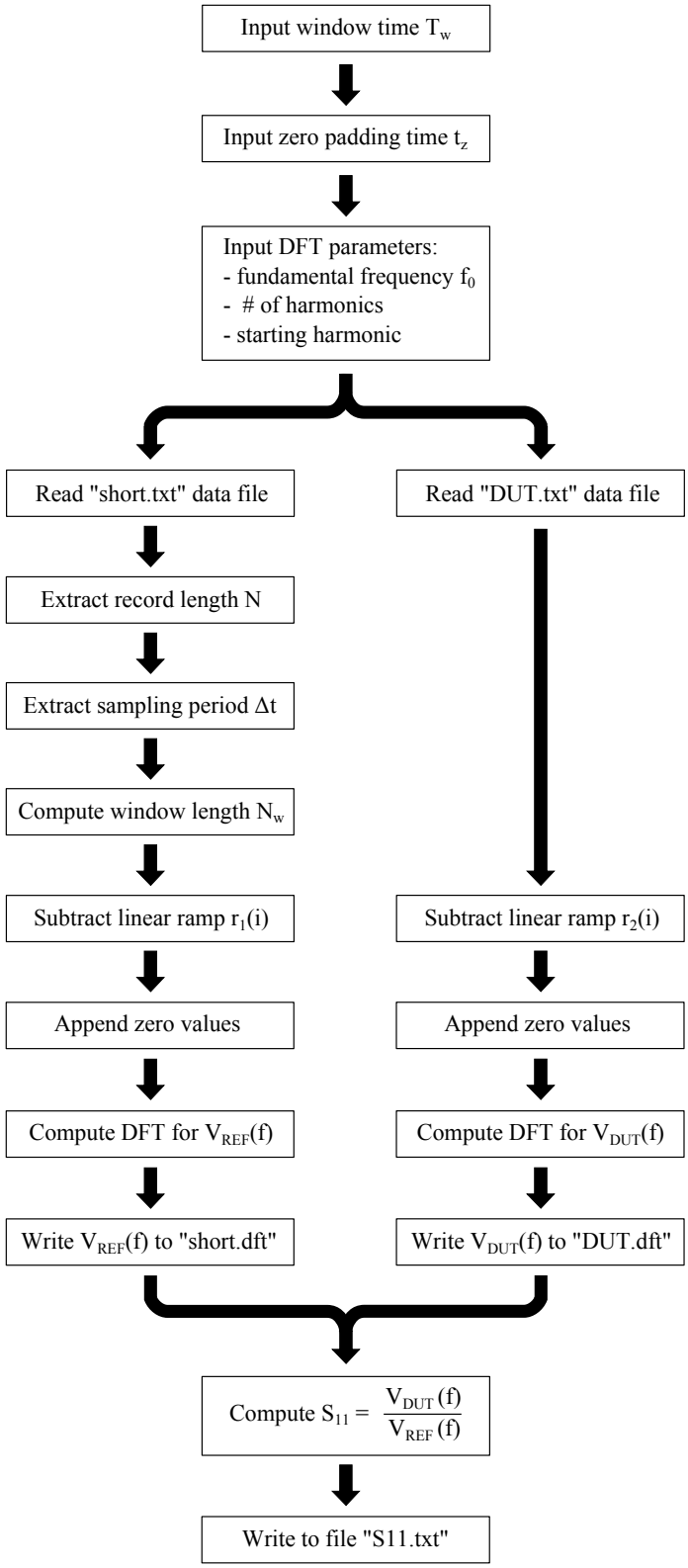

Figure 6.7: *Flow chart of the data processing program implemented in Matlab.*

and producing an S_{11} data file. The program was implemented in Matlab, due primarily to the extensive libraries available such as the DFT.

6.3.4 Evaluation of the Time Window Length

The root mean square error ($RMSE$) between the VNA $S_{11-VNA}(f)$ reference and each TDR $S_{11-TDR}(f)$ measurement was calculated by

$$RMSE = \sqrt{\frac{1}{n}\sum_{f(min)}^{f(max)}(|S_{11-VNA}(f)| - |S_{11-TDR}(f)|)^2} \tag{6.1}$$

but limited to the working range of the antenna where $f(min) = 5.4\,\text{GHz}$, $f(max) = 6.2\,\text{GHz}$, and n being the number of harmonics between 5.4–6.2 GHz.

The $RMSE$ was evaluated for each data set with T_w ranging from 15–50 ns (0 ns start time). A plot of the $RMSE$ versus T_w between the VNA reference and each TDR measurement is shown in figure 6.8. Overall, the impulse TDR has significantly less error than the step TDR. In both cases the error is largest when $T_w < 25\,\text{ns}$, a region where the oscillations had not yet reached

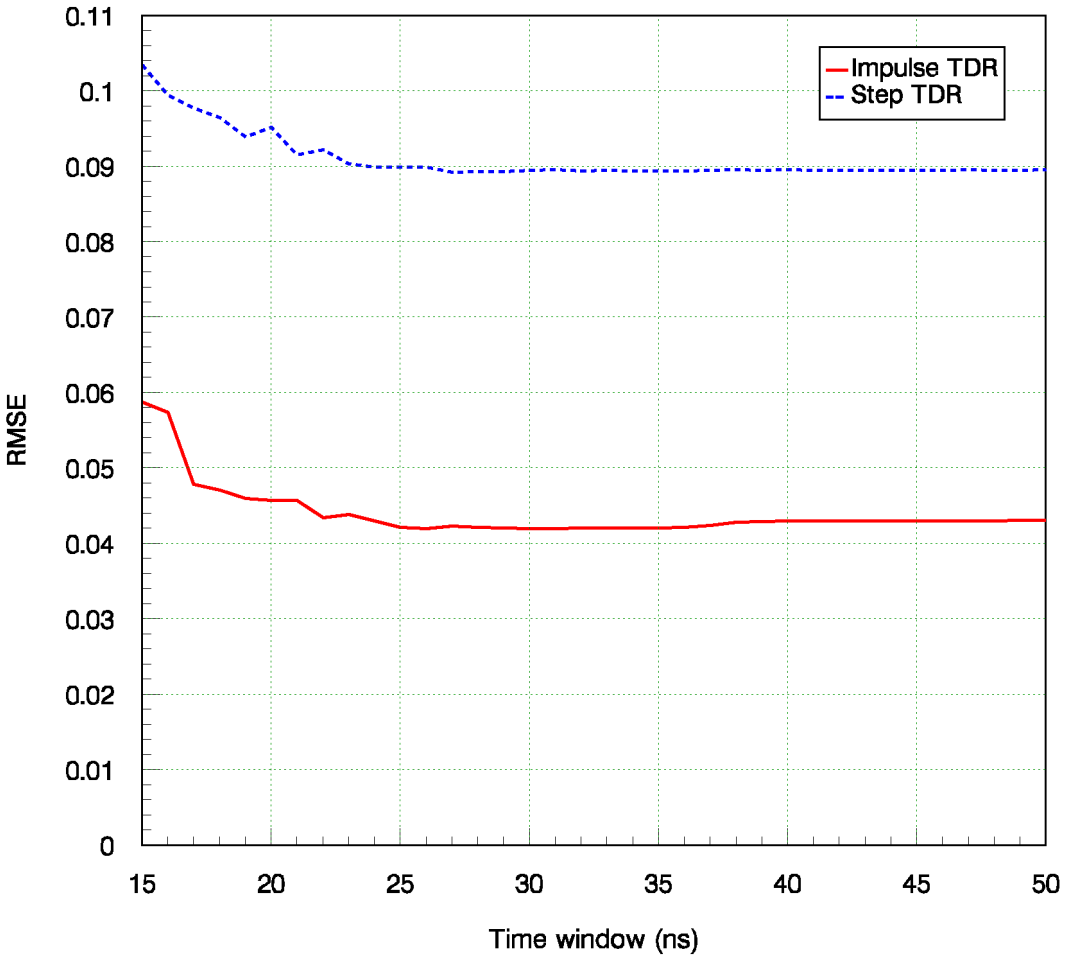

Figure 6.8: *The RMSE between the VNA reference and each TDR measurement.*

a steady-state as can be verified in figure 6.5(b). The slight increase of error in only the impulse TDR trace when $T_w > 38\,\text{ns}$, suggests the impulse TDR had either a slight impedance mismatch or had a high enough sensitivity to detect spurious reflections from nearby objects. Since the calculation for the 40 ns upper time window limit in section 6.2 was only an approximation, the latter may be a reasonable explanation.

Therefore, the time window necessary to ensure a steady-state condition is reached while limited to block spurious reflections from nearby objects is anywhere between $25\,\text{ns} < T_w < 38\,\text{ns}$. A 31 ns time window was chosen for the subsequent analysis. This corresponds to the shaded portion as shown in the antenna reflection in figure 6.9.

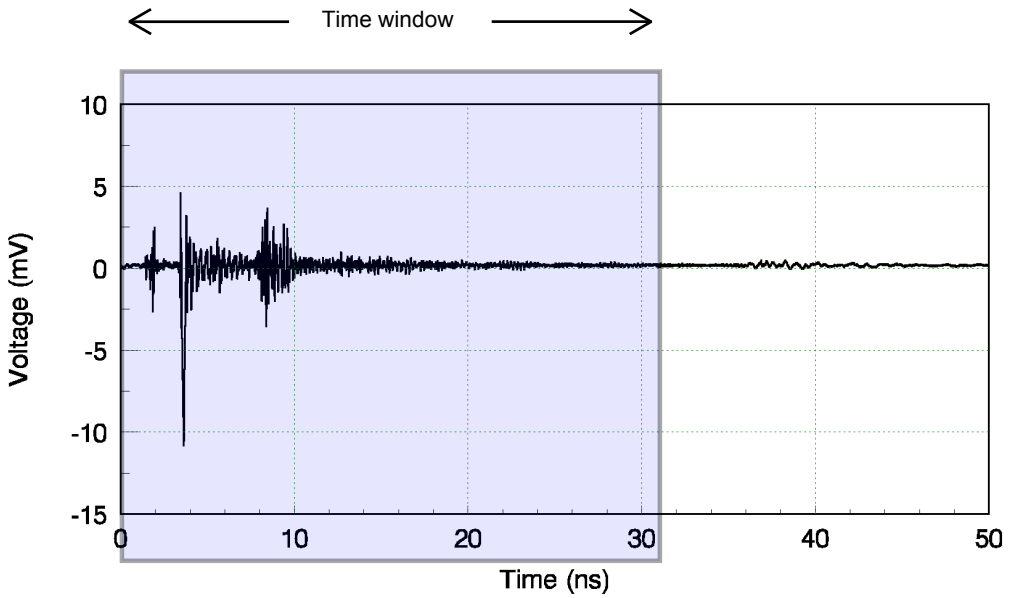

Figure 6.9: *Plot of the reflected signal seen by the impulse TDR when the wideband antenna is connected at the reference plane. The shaded region corresponds to the optimal time window chosen for subsequent analysis.*

6.3.5 $|S_{11}|$ Characterisation

The $|S_{11}(f)|_{\text{dB}}$ response obtained by both the impulse TDR and step TDR systems were plotted against the VNA reference as shown in figure 6.10. The same measurement is shown in 6.11 but with the frequency axis limited to the working range of the antenna. It is apparent the impulse TDR is most appropriate for measuring the antenna as compared with the step TDR. Needless to say, however, the superior dynamic range of the VNA is evident where the magnitude drops to $-35\,\text{dB}$.

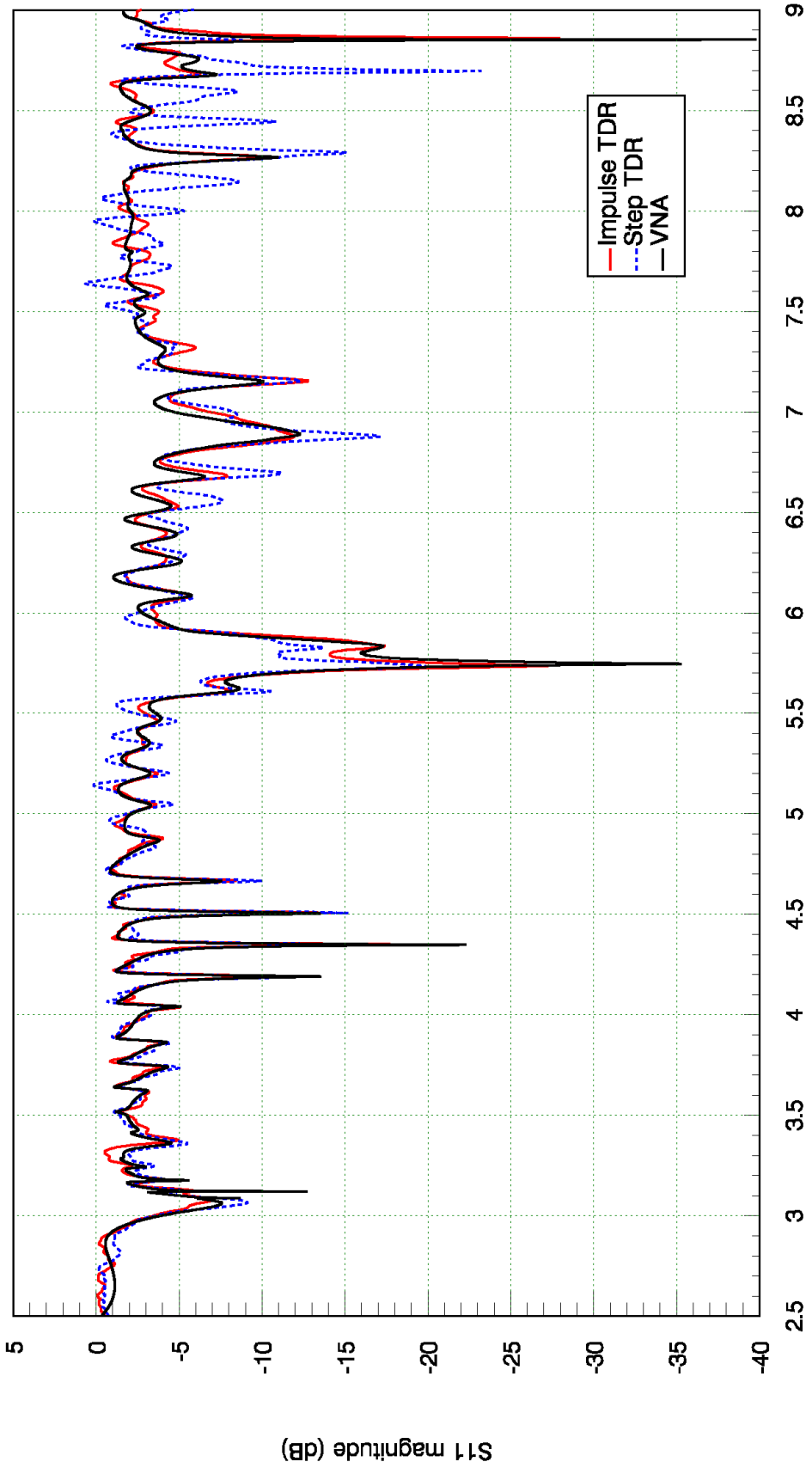

Figure 6.10: *Comparison of* $|S_{11}(f)|_{\mathrm{dB}}$ *measurements made by the impulse TDR, step TDR, and VNA, up to 9GHz.*

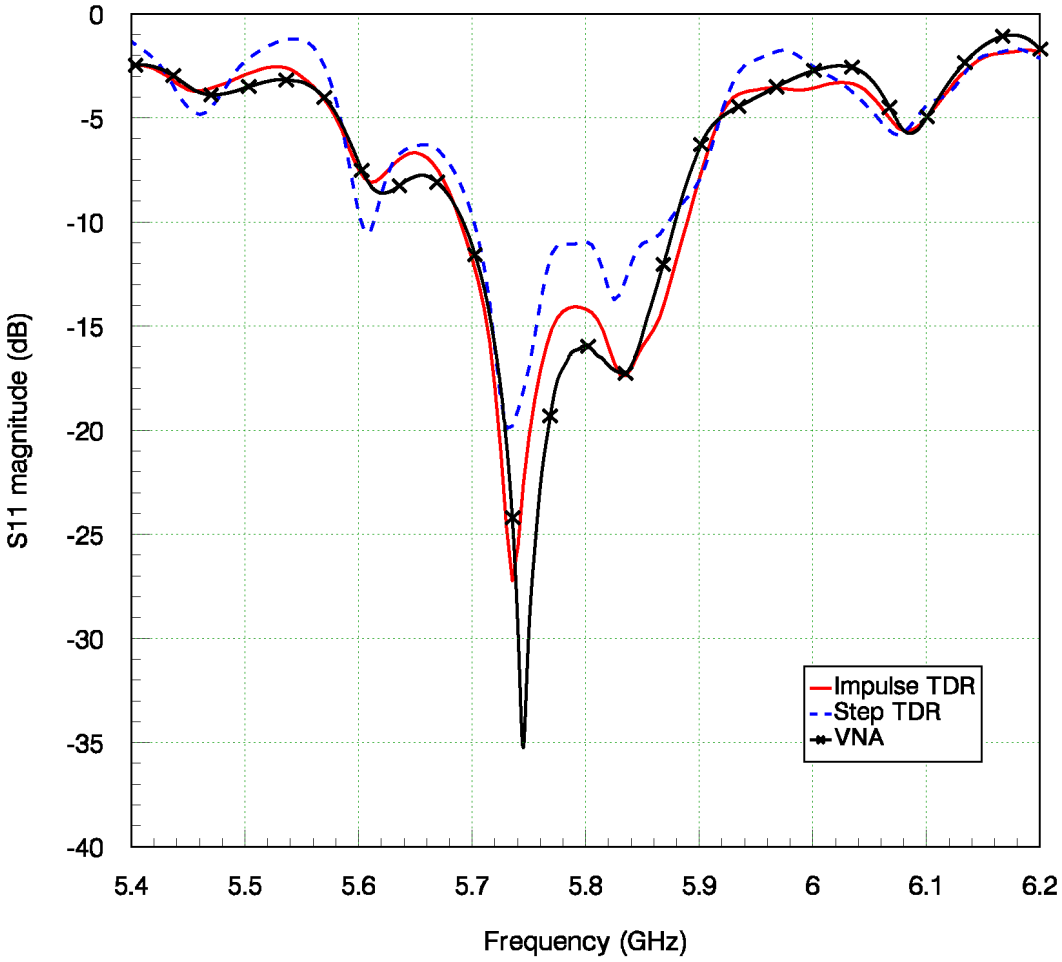

Figure 6.11: *Comparison of $|S_{11}(f)|_{\mathrm{dB}}$ measurements made by the impulse TDR, step TDR, and VNA, limited to the working frequency range of the antenna.*

6.3.6 Signal Spectra

The spectra measured in the reference short reflections for both the impulse TDR and step TDR systems[1] are shown in figure 6.12(a). Similarly, the spectra present in the antenna reflection for each TDR system are shown in figure 6.12(b). The noise floor was determined by measuring the noise present in the system with the signal source disabled. It is apparent from both figures that the energy in the impulse TDR reflection exceeds the energy in the step TDR reflection above about 3.3 GHz.

A plot of the signal-to-noise ratio (SNR) for each TDR system is shown in figure 6.13. Another plot that highlights the difference in SNR between the

[1]The spectra in figure 5.6 were computed from the continuous Fourier transform of single transient signals, whereas the various spectra in figure 6.12 were computed from the discrete Fourier transform of periodic waveforms. This difference results in the magnitudes of each figure to be scaled slightly differently.

impulse TDR and step TDR is in figure 6.14. The 23 ps impulse TDR has a significantly higher SNR compared with the Agilent 54754A 40 ps step TDR for frequencies above 3.3 GHz. This is especially evident at 7.5 GHz, where the impulse TDR exceeds the step TDR by 20 dB.

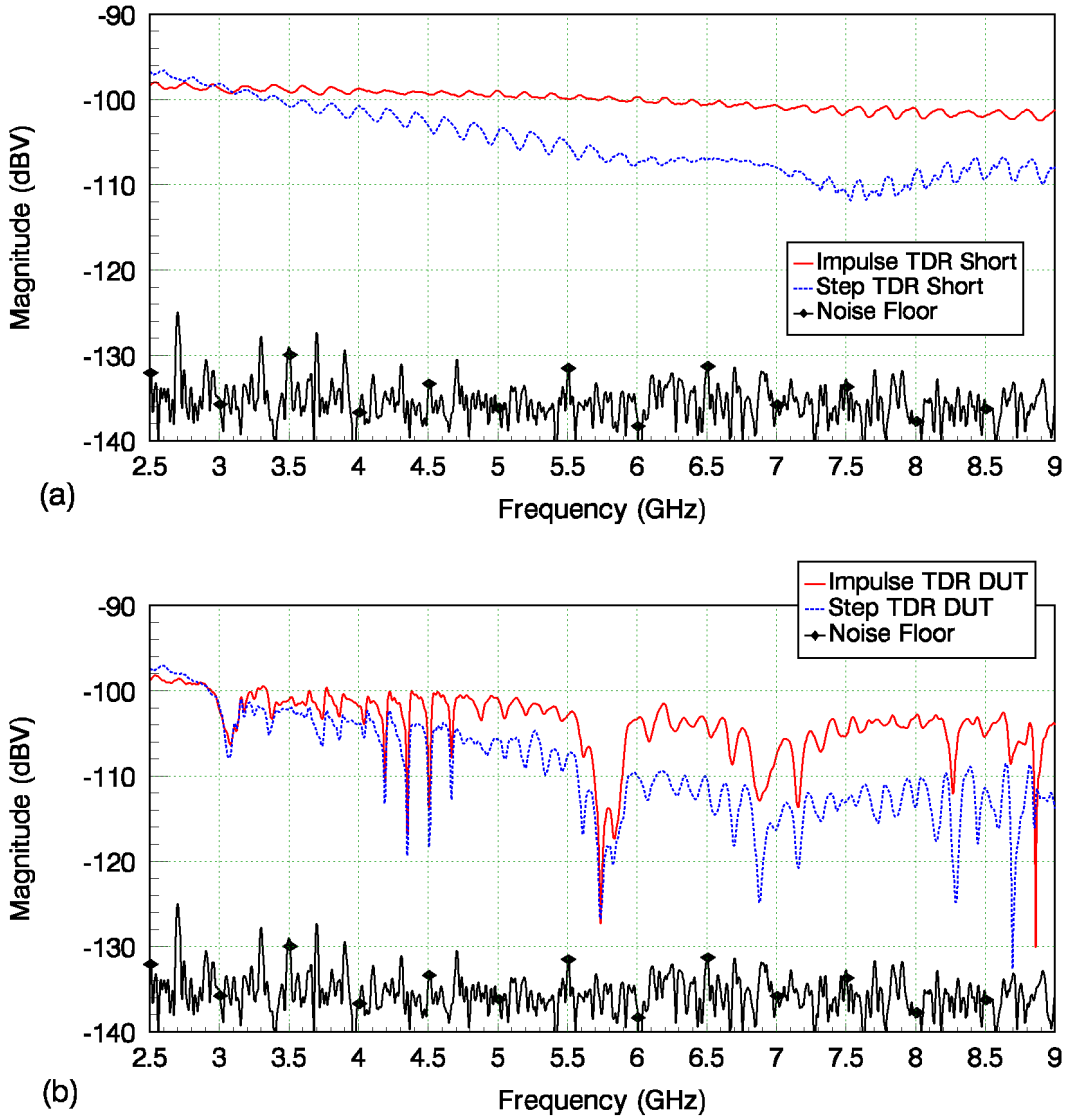

Figure 6.12: *The frequency spectra for the impulse TDR and step TDR measurements when the (a) reference short was connected at the reference plane (b) DUT (antenna) was connected at the reference plane.*

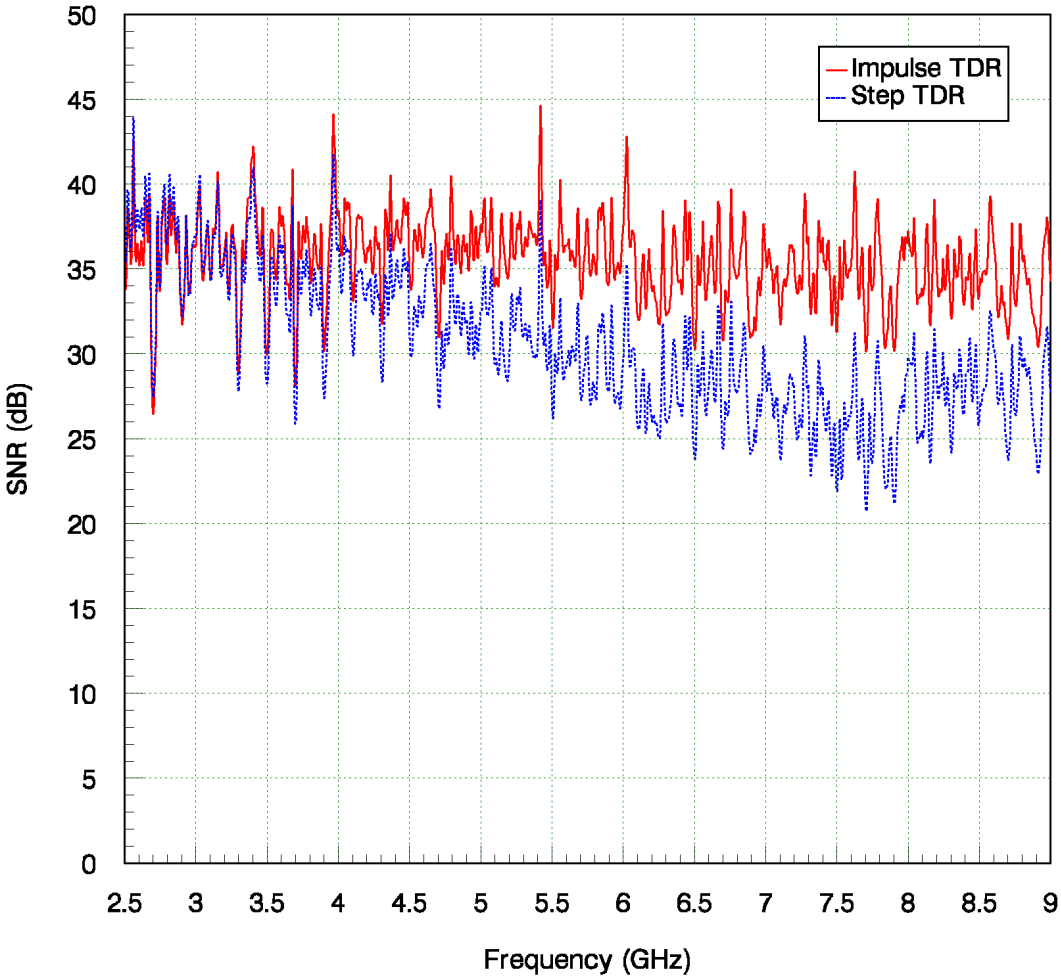

Figure 6.13: *The SNR of the 23ps impulse TDR and the 40ps step TDR when the oscilloscope is averaging 1024 times.*

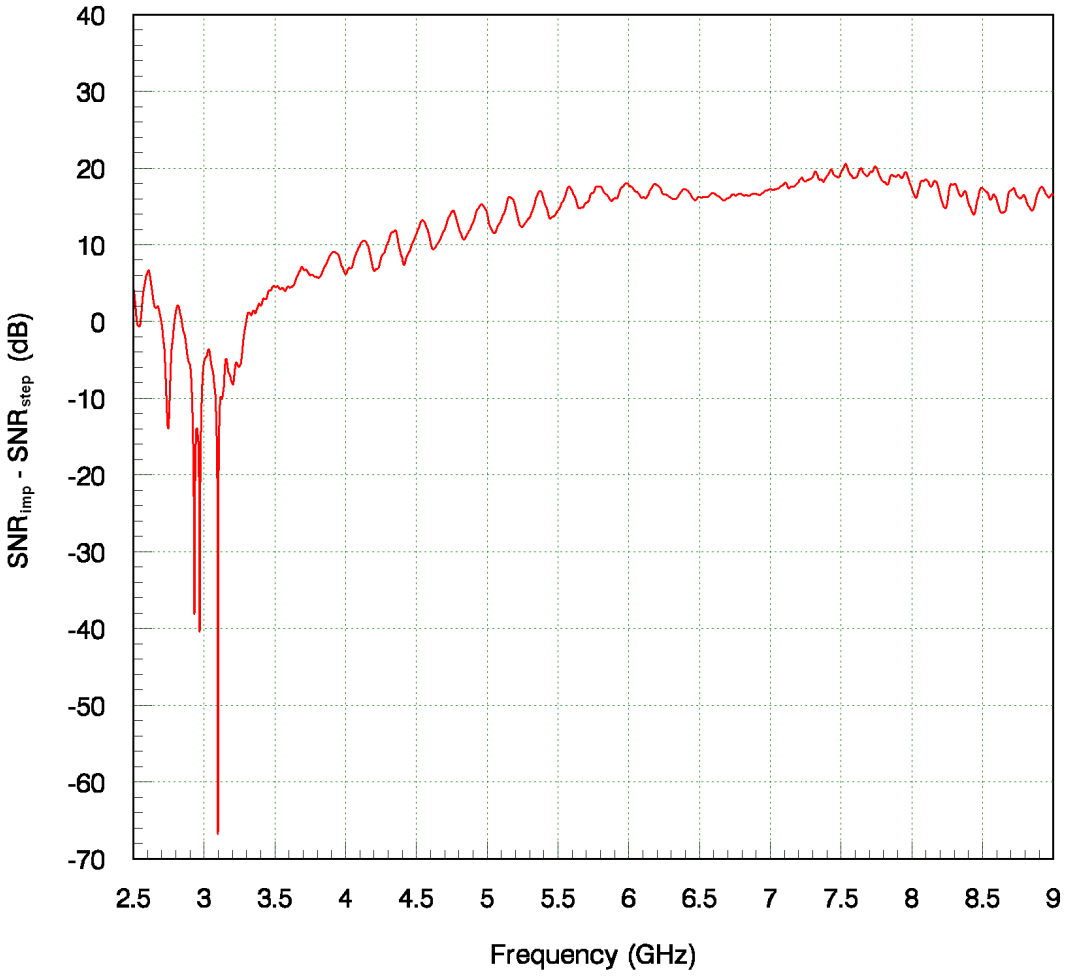

Figure 6.14: *The difference in SNR between each TDR system. Positive values indicate a higher SNR for the impulse TDR, whereas negative values indicate a higher SNR for the step TDR.*

6.3.7 Variance

The variance $\sigma^2(f)$ between the VNA $|S_{11}(f)|$ reference and each TDR $|S_{11}(f)|$ measurement was calculated by

$$\sigma^2(f) = (|S_{11-VNA}(f)| - |S_{11-TDR}(f)|)^2 \tag{6.2}$$

A plot of the linear variance measured between 2.5–9.0 GHz is shown in figure 6.15. Since the rate at which SNR falls with frequency is higher for the step TDR (figure 6.13), it comes with no surprise that the impulse TDR measurement contains less variance than the step TDR measurement, especially above 5.0 GHz.

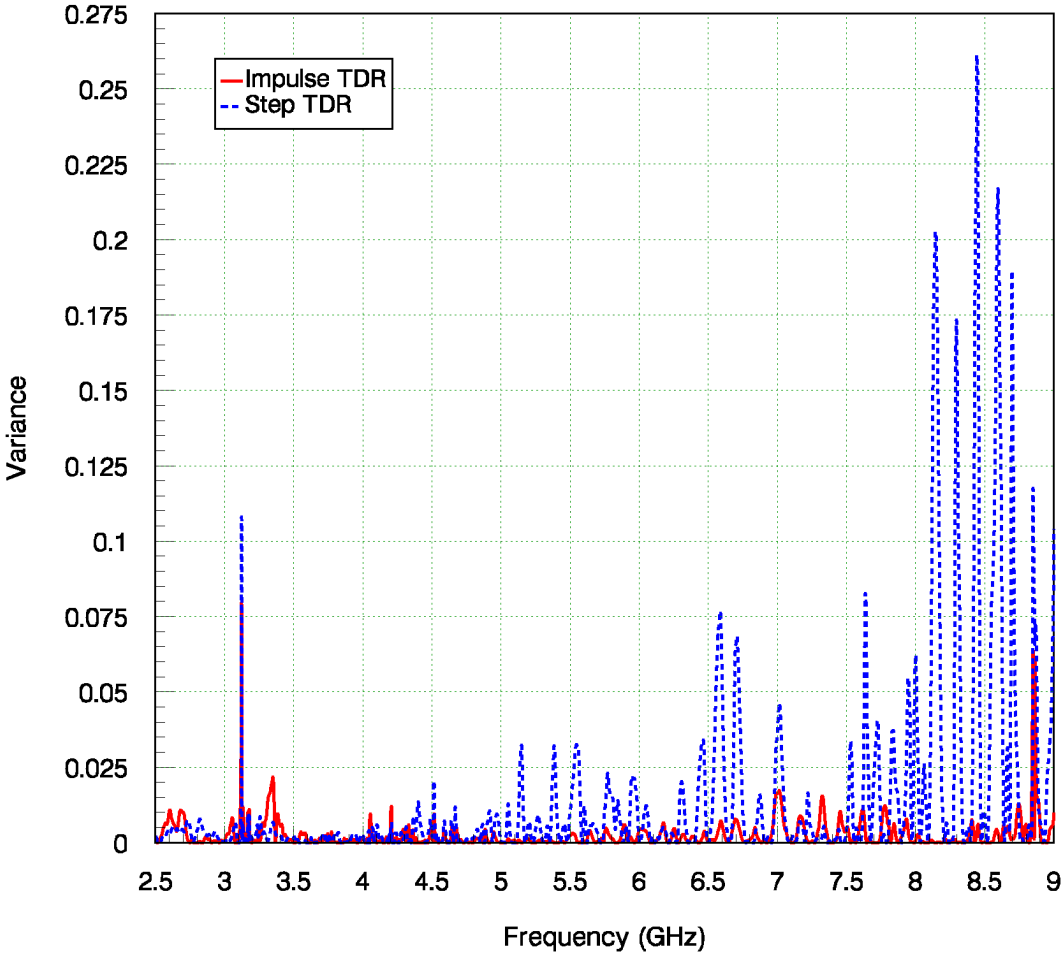

Figure 6.15: *Variance measured to 9GHz between each TDR system response and the VNA reference.*

Chapter 7

Discussion

Impulse TDR does not have an intuitive or informative display, making it less desirable for conventional measurements in the time-domain. However, when the measurements are transformed into the frequency-domain, for example, to compute the reflection scattering parameter $S_{11}(f)$ of an antenna, the impulse version of TDR contains more energy than even an ideal step version of TDR above 7.5 GHz. As a consequence, a higher SNR is achieved and the dynamic range is improved. In fact, through practical measurement of the signal spectra it was shown the 23 ps impulse signal contained more energy than the 40 ps step signal down to 3.1 GHz.

Recommendations for the application of impulse TDR, step TDR, and VNA measurement techniques, are summarised in Table 7.1. The numerical value for each parameter will vary with circumstance and so only trends are given. The last column is relevant only to the measurement of antennas.

Table 7.1: *Comparison of measurement techniques.*

Technique	**Bandwidth**	**Dynamic range**	**Equipment cost**	**Anechoic chamber**
Impulse TDR	Med	Med	Med	No
Step TDR	Low	Low	Med	No
VNA	High	High	High	Yes

7.1 Suggestions For Improvement

7.1.1 Hardware

The dynamic range could be vastly improved if the impulse generator was located prior to the sampling gate as shown in figure 7.1. This arrangement

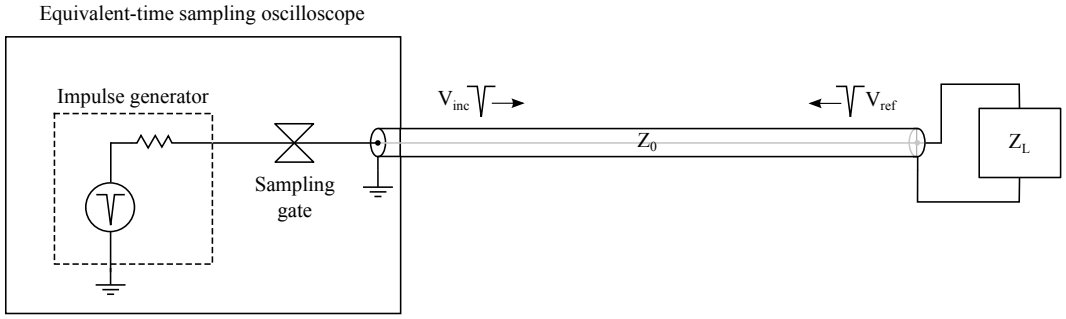

Figure 7.1: *The impulse generator is located prior to the sampling gate, eliminating the need for the power divider.*

would eliminate the need for the lossy power divider, closely resembling the conventional step TDR back in figure 3.1. A modification to the hardware within the Agilent 54754A TDR module would be necessary.

7.1.2 Reference Measurement

The VNA reference measurement was performed outdoors with the antenna pointed towards the sky. This was to reduce spurious reflections and hence simulate an anechoic-type environment. However, higher accuracy could be achieved if the measurement was performed within an anechoic chamber [65], minimising any effects from external sources of interference. Furthermore, with access to a higher bandwidth VNA, the performance of impulse TDR could be assessed beyond 9 GHz.

7.1.3 Advanced Calibration

The impulse TDR could employ a more advanced short-open-load (SOL) calibration scheme for de-embedding parasitics and discontinuities, hence improving the accuracy of the $S_{11}(f)$ measurement. As a result however, the calibration becomes a time-consuming procedure as is the case for a VNA calibration. For further reading see [66]–[72].

7.2 Suggestions For Future Research

With the improved dynamic range at higher frequencies, impulse TDR could replace step TDR in the measurement of:

- transmission lines [45] and interconnects [50];
- the complex permittivity ϵ and permeability μ of materials using dielectric measuring probes [51], [56];
- the moisture content in soil [52], [53];
- the moisture content in food [54], [55].

Impulse TDR may also be advantageous when the user is looking for precision in spatial localisation, say in a connector or similar in-line structure, as the increased energy at higher frequencies can help.

Chapter 8

Conclusion

This thesis has presented impulse time-domain reflectometry or "impulse TDR" (ITDR). A review has been given of equivalent-time sampling, RF transmission line theory, and traditional TDR, along with some of its more recent applications, to provide a full theoretical background. In particular, the application of TDR to the measurement of antennas is of interest, because of the band-pass nature of the measurement, and the cost advantages it confers over vector network analyser (VNA) methods.

This thesis has shown impulse TDR to be superior to the traditional step TDR for characterising band-pass microwave systems. This superiority arises from the higher spectral content of impulse waveforms above the crossover frequency where the falling response of a step, ideal and practical, is exceeded by the less-steeply falling response of a practical impulse.

An impulse TDR was constructed and demonstrated. The instrument employs the latest impulse-generator technology in conjunction with an 18 GHz equivalent-time sampling oscilloscope. The proposition of this thesis has been verified by comparing theoretical prediction with simulated and measured performance for both the step and impulse cases applied to the characterisation of an antenna. In addition, results were compared with measurements made with a VNA, the traditional instrument used in antenna characterisation studies.

A manuscript describing the advantages of impulse TDR to the characterisation of antennas (see appendix A) has been accepted for publication by the IEEE in Microwave and Wireless Components Letters. A manuscript detailing the use of impulse TDR and the differences between this and step TDR (see

appendix B) has been accepted for presentation at the Asia-Pacific Microwave Conference in December 2011. These are world-class venues for the reporting of microwave research.

It is hoped that through the information presented in this thesis, the benefits of impulse TDR are realised and new applications emerge.

Appendix A

Published Journal Article

The following manuscript was published by the IEEE Microwave and Wireless Components Letters [73].

Measurement of Antennas and Microwave Components Using Time-Domain Reflectometry of a Voltage Impulse

Steven McCabe, *Student Member, IEEE,* and Jonathan Scott, *Senior Member, IEEE*

***Abstract*—Band-pass microwave systems such as ultra-wideband (UWB) antennas are traditionally characterized in the frequency-domain through a vector network analyzer (VNA) in an anechoic chamber. A recent study proved antennas could be accurately measured in the time-domain using a step-function time-domain reflectometer (TDR), without the need for an anechoic chamber. We propose a new advance in the TDR characterization method. An impulse generator is employed in place of the step generator in a TDR set-up. The advantage conferred by this change is that more energy is available beyond a given frequency than with a step, and so a higher signal-to-noise ratio (SNR) is achieved. The theoretical result is compared with measurement.**

***Index Terms*—Antenna measurements, frequency-domain (FD) analysis, pulse measurements, time domain reflectometry (TDR), transient response.**

I. Introduction

TIME-DOMAIN reflectometry (TDR) is a well-known technique in electronic and optical systems [1]–[4]. It has recently been used successfully in the characterization of antennas in [5] and [6]. The motivation behind this is twofold: A TDR is less costly than a vector network analyzer (VNA) [5], but more importantly the time-localization of the energy in the test signal means that the user can dispense with the anechoic chamber that is required for antenna measurements with a sinewave exciting signal.

The traditional stimulus signal in a TDR is a voltage step. The energy in a step signal falls with increasing frequency. In the situation where the device under test (DUT) is interesting in only a limited high bandwidth, as with antennas, most of the energy in the step is wasted and the dynamic range of the measurement is limited. On the other hand, an impulse test signal has a theoretically flat bandwidth. In this paper, we explore the advantages of making impulse TDR measurements, similar to a traditional TDR but employing an impulse-like signal instead of a step-like signal. The work is timely because a high-quality impulse generator has become available [7]–[9]. This allows us to compare theory with measurement.

II. Fourier Transform of the Stimulus Signal

The unit impulse (Dirac delta) function is defined as having zero amplitude for all time except at $t = 0$, where it has infinite amplitude:

$$\delta(t) = \begin{cases} 0, & t \neq 0 \\ \infty, & t = 0 \end{cases}$$

The Fourier transform for the unit impulse is

$$\mathrm{F}[\delta(t)] = 1 \tag{1}$$

An ideal impulse has a flat frequency response. Although the unit impulse is a theoretical construct and does not physically exist [10], it is used as a limiting case when the width of a pulse approaches zero. Derived from the convolution of two rectangular ("rect") functions, the trapezoid function provides an approximation of a realistic impulse with finite rise and fall times [11]:

$$u(t) = \frac{1}{\tau}\,\mathrm{rect}\left(\frac{t}{\tau}\right) \otimes A\,\mathrm{rect}\left(\frac{t}{T}\right) \tag{2}$$

where A is the trapezoid amplitude, T is the full width at half maximum (FWHM), and τ is the rise/fall time from 0 to 100% of the amplitude. The Fourier transform of $u(t)$ is given by

$$\mathrm{F}[u(t)] = AT\,\mathrm{sinc}(f\tau)\,\mathrm{sinc}(fT) \tag{3}$$

The Heaviside unit step function is defined as

$$H(t) = \begin{cases} 1, & t > 0 \\ \frac{1}{2}, & t = 0 \\ 0, & t < 0 \end{cases}$$

This function represents an ideal voltage step which is immediately elevated to a constant level at a definite time [12]. The Fourier transform of $H(t)$ is given by

$$\mathrm{F}[H(t)] = \frac{1}{j2\pi f} + \frac{1}{2}\delta(f) \tag{4}$$

The response varies as the reciprocal of frequency and so approaches zero amplitude as frequency tends to infinity. This theoretical construct does not physically exist because a realistic step waveform has a finite rise time. The Fourier transform for a step function $s(t)$ with finite rise time is given by

$$\mathrm{F}[s(t)] = A\frac{1}{j2\pi f}\,\mathrm{sinc}(f\tau) \tag{5}$$

where τ is the rise time from 0 to 100% of the amplitude A. Fig. 1 presents a number of spectra that will be compared

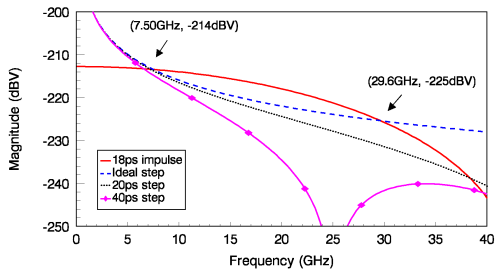

Fig. 1. The Fourier transforms of an ideal unit step, some practical step-like signals, and a practical trapezoidal pulse of unit amplitude. The unit for magnitude is dBV, namely the voltage relative to 1 Volt.

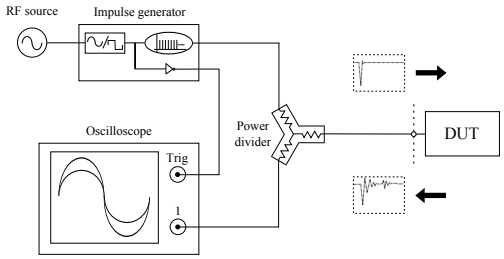

Fig. 2. An impulse TDR set-up for the measurement of microwave devices. A generated impulse is transferred to the DUT, resulting in a reflection that is monitored on the TDR. The dashed line represents the reference plane at the DUT connector.

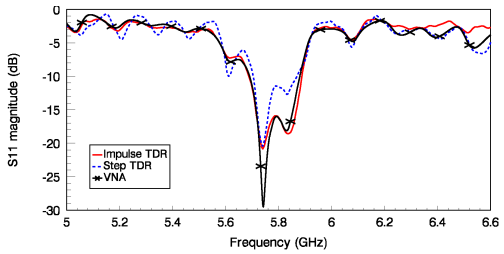

Fig. 3. Comparison of $|S_{11}(f)|_{\mathrm{dB}}$ measurements made by the impulse TDR, step TDR, and VNA, limited to the working frequency range of the wide-band antenna. The superior dynamic range of the VNA is evident where the magnitude drops to almost $-30\,\mathrm{dB}$.

with the spectrum of an ideal step (Heaviside unit step) that appears as the dashed line. The new impulse source generates impulses with a typical FWHM of $23\,\mathrm{ps}$ [13]. The rise/fall time is estimated as $18\,\mathrm{ps}$ ($5\,\mathrm{ps}$ flat-top). By inserting these parameters in (3), the Fourier transform of a unit amplitude impulse was simulated in Matlab. This function can now be compared with the unit step from (4) and some realistic step waveforms from (5) in Fig. 1. It can be seen that even the realistic, limited impulse signal contains more energy than an ideal step for frequencies above about $7.5\,\mathrm{GHz}$. When the step waveform is not ideal, but similar to what is practically available today, the comparison becomes even more favorable, as can be seen in the same figure.

III. Measured Results

An impulse-style TDR was constructed as shown in Fig. 2. The set-up features an impulse generator with a $23\,\mathrm{ps}$ pulse width [7]–[9], a DC to $26.5\,\mathrm{GHz}$ power divider, and an $18\,\mathrm{GHz}$ TDR operating in oscilloscope mode [14]. The DUT was a Wide-Band sector antenna designed to operate between 5.47-$5.85\,\mathrm{GHz}$. A step-type TDR set-up was constructed using a similar configuration but with the impulse source replaced with a $50\,\Omega$ dummy load and the mainframe set in TDR mode. The divider was included to replicate the conditions of the impulse TDR set-up so that fair comparisons between techniques could be made. An attenuator was also inserted between the oscilloscope channel and the divider, to further reduce the step signal to a similar amplitude produced in the impulse TDR set-up. Calibrated measurements were acquired using a VNA, where the DUT was situated outdoors to provide an accurate reference for comparison with the TDR measurements.

A. Acquisition in the Time-Domain

Two time-domain measurements were employed in the subsequent frequency-domain processing: A reference waveform reflected from a short, and the waveform reflected by the antenna. Averaged measurements taken by the impulse TDR set-up were windowed with the Dirichlet window in Matlab, to remove the incident portion of the signal and to remove spurious reflections as required for subsequent frequency-domain processing as reported in [5]. The rectangular window contained the essential data that corresponded to the DUT response, and provided a reference plane extended to the end of the cable where the DUT was to be attached. The length of the time window was chosen so that there was sufficient time for the antenna's reflection to settle, while limited to block out spurious reflections caused by the presence of objects near the antenna. Initially, a $35\,\mathrm{ns}$ acquisition window was chosen as endorsed in [5]. The same process was followed for the acquisition of the step TDR measurements.

B. Transformation to the Frequency-Domain

The zero-padding operation was employed to ensure adequate frequency resolution, along with the application of the Nicolson algorithm to avoid truncation error [3]. A computer program computed the discrete Fourier transform (DFT) for both the reference reflection and DUT reflection, resulting in $V_{ref}(f)$ and $V_{DUT}(f)$. The reflection scattering parameter $S_{11}(f)$ was then computed by $S_{11}(f) = V_{DUT}(f)/V_{ref}(f)$ for frequencies between 2.0-$9.0\,\mathrm{GHz}$. The DUT $|S_{11}(f)|_{\mathrm{dB}}$ response obtained by both the impulse TDR and step TDR methods, were plotted against the VNA reference as shown in Fig. 3. The frequency range shown is constrained to the antenna's specified operating range.

C. Variance

A plot of the $|S_{11}(f)|$ variance measured between the TDR measurements and the VNA reference are shown in Fig. 4.

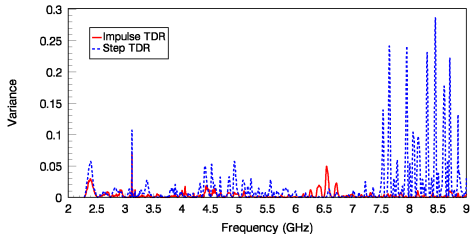

Fig. 4. $|S_{11}(f)|$ variance measured to 9 GHz between each TDR system response and the VNA reference.

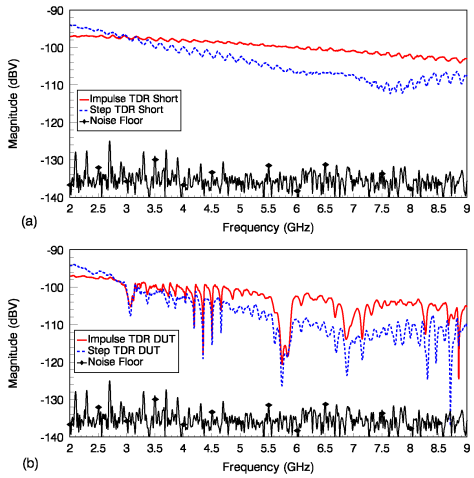

Fig. 5. The frequency spectra for the impulse TDR and step TDR measurements when the (a) reference short was connected at the reference plane (b) DUT was connected at the reference plane. The noise floor was determined by measuring the noise present in the system with the signal source disabled.

The frequency axis is limited to the 9.0 GHz bandwidth of the VNA. The impulse TDR measurement clearly contains less variance than the step TDR measurement, especially above 7.0 GHz.

D. Dynamic Range

The spectra measured in the reference short reflections for both the impulse TDR and step TDR systems are shown in Fig. 5(a). Similarly, the spectra present in the DUT reflection for each TDR set-up are shown in Fig. 5(b). It is apparent from both figures that the energy in the impulse TDR reflection exceeds the energy in the step TDR reflection above about 3.1 GHz. Beyond 3.1 GHz the 23 ps impulse TDR offers a significant improvement in SNR compared with the Agilent 54754A 40 ps step TDR. Recommendations for the application of impulse TDR, step TDR, and VNA measurement techniques, are summarized in Table I. The numerical value for each parameter will vary with circumstance and so only trends are given.

TABLE I
COMPARISON OF MEASUREMENT TECHNIQUES

Technique	Bandwidth	Dynamic range	Equipment cost	Anechoic chamber
Impulse TDR	Med	Med	Med	No
Step TDR	Low	Low	Med	No
VNA	High	High	High	Yes

IV. Conclusion

In the situation where the user will post-process reflection waveform data, for example, to determine S-parameters, the impulse version of TDR is superior at frequencies above 7 GHz. It may also be advantageous when the user is looking for precision in spatial localization, say in a connector or similar in-line structure, as the increased energy at higher frequencies can help.

Acknowledgement

The authors wish to acknowledge the support of Agilent Technologies Component Test Division for the supply and detailed support of equipment. Thanks are also due to Skynet Data Communications Technology Ltd for the supply of equipment and support.

References

[1] C. Chiu, W. Chen, K. Liao, B. Chen, Y. Teng, G. Huang, and L. Wu, "Pad characterization for CMOS technology using time domain reflectometry", in *Proc. IEEE Int. RF and Microwave Conf.*, in Kuala Lumpur, Dec. 2008, pp. 215-217.

[2] M. Harper, N. Ridler, and M. Salter, "Comparison between root-impulse-energy and vector network analyzer methods for measuring loss on printed circuit boards", in *ARFTG Microwave Measurement Symp.*, in Portland, OR, 2008, pp. 20-25.

[3] A. Cataldo, L. Catarinucci, L. Tarricone , F. Attivissimo, and A. Trotta, "A TD-FD combined method for enhancing reflectometry measurements in liquid quality monitoring", in *Proc. IEEE Instrum. Meas. Tech. Conf.*, in Warsaw, May. 2007, pp. 1-5.

[4] M. Gerding, T. Musch, and B. Schiek, "A novel approach for a high-precision multitarget-level measurement system based on time-domain reflectometry" *IEEE Tran. Microw. Theory Tech.*, vol. 54, no. 6, pp. 2768-2773, Jun. 2006.

[5] A. Cataldo, G. Monti, E. De Benedetto, G. Cannazza, L. Tarricone, and L. Catarinucci, "Assessment of a TD-based method for characterization of antennas", *IEEE Trans. Instrum. Meas.*, vol. 58, no. 5, pp. 1412-1419, May. 2009.

[6] R. Tamas, G. Caruntu, and D. Popa, "A time-domain measuring technique for ultra-wide band antennas", *Microwave and Optical Technology Letters*, vol. 53, no. 2, pp. 281-286, Feb. 2011.

[7] J. Scott and D. Gunyan, "Pulse generator", US patent number *7,423,470*, Sep, 2008.

[8] J. Scott and M. Hoy, "Group-delay measurement of frequency-converting devices using a comb generator", *IEEE Trans. Instrum. Meas.*, vol. 59, no. 11, pp. 3012-3017, Nov. 2010.

[9] P. Blockley, D. Gunyan, and J. Scott, "Mixer-based, vector-corrected, vector/network analyzer offering 300kHz-20GHz bandwidth and traceable response", *IEEE Int. Microwave Symp.* in Long Beach, CA, Jun. 2005, pp. 1-4.

[10] S. Haykin and M. Moher, *Introduction to analog & digital communications, second edition*, John Wiley & Sons, Inc, pp. 42-49, 2007.

[11] D. Brandwood, *Fourier transforms in radar and signal processing*, Artech House, Inc., pp. 39-47, 2003.

[12] R. N. Bracewell, *The Fourier transform and its applications, third edition*, McGraw-Hill International Editions, pp. 61, 2000.

[13] *Agilent U9391C/F comb generators technical overview*, Agilent Technologies, [Online]. Available: http://www.home.agilent.com/agilent/product.jspx?pn=U9391C retrieved Jan 2010.

[14] *Agilent 54753A and 54754A TDR plug-in modules user guide*, Agilent Technologies, publication number 54753-97015, 2000.

Appendix B

Conference Paper (To be Published)

The following manuscript has been accepted for presentation at the IEEE Asia-Pacific Microwave Conference in December 2011.

Impulse TDR and its Application to Measurement of Antennas

Steven McCabe[1], Jonathan Scott[2]

Department of Engineering, The University of Waikato,
Gate 8 Hillcrest Road, Hamilton, New Zealand
[1]som1@waikato.ac.nz
[2]jonathanscott@ieee.org

***Abstract*—The traditional stimulus signal used in a time-domain reflectometer (TDR) is a voltage step. We propose an alternative technique, whereby an impulse generator is employed in place of the step generator in a TDR. The advantage conferred by "impulse TDR" is that more energy is available at higher frequencies than with conventional step TDR, and so a higher bandwidth and signal-to-noise ratio (SNR) is achieved. The theoretical result is compared with measurement.**

***Index Terms*—Antenna measurements, frequency-domain (FD) analysis, pulse measurements, time domain reflectometry (TDR), transient response.**

I. Introduction

Time-domain reflectometry (TDR) is a well-known technique that is typically used to measure the impedance of discontinuities as a function of time (or distance) in electronic systems [1]–[4]. A TDR instrument consists primarily of an oscilloscope and a test signal generator, where the test signal is traditionally a voltage step. As a consequence of the Fourier transform, the energy in the spectrum of a step falls with increasing frequency. On the other hand, an ideal impulse (Dirac delta) test signal has a theoretically flat bandwidth. In this paper, we explore the advantages of making impulse TDR measurements, similar to a traditional step TDR but employing an impulse-like signal instead of a step-like signal. The work is timely because a high-quality impulse generator has recently become commercially available [5]–[7]. This allows us to compare theory with measurement.

II. Time-Domain Comparisons Between Step TDR and Impulse TDR

Fig. 1 illustrates a variety of different waveforms for common load conditions on a characteristic line impedance, Z_0, in the well-known case of a TDR built using a step stimulus signal, compared with the case of an impulse stimulus signal. The waveforms contain the incident stimulus signal that is applied to the load impedance, Z_L, followed by some signal reflected back to the TDR. The middle column of the figure will be familiar to many practitioners. The waveforms that result from the various load circuits are "common sense" and easily remembered or worked out with some familiarity. However, the waveforms in the right-hand column, in the case of the impulse signal, are neither familiar nor obvious. This difference arises because the emphasis of energy on low frequencies in the step case results in waveforms that resemble the classic transient response waveforms for RC and RL circuits that are taught in junior circuit theory courses. No such familiar resemblance arises in the impulse case. For this reason, impulse TDR is not likely to replace step TDR in the analysis of simple discontinuities on a transmission line.

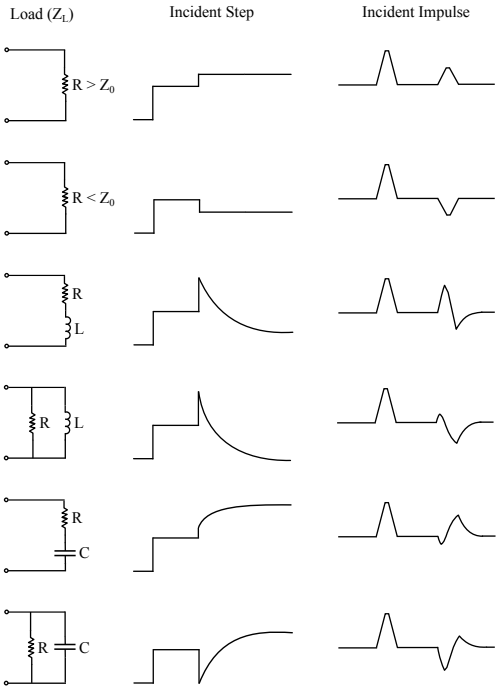

Fig. 1. Comparison of visual displays to be expected for a variety of common load circuits in the case of conventional step TDR and the proposed impulse TDR.

III. Fourier Transform of the Stimulus Signal

The unit impulse (Dirac delta) function is defined as having zero amplitude for all time except at $t = 0$, where it has infinite amplitude:

$$\delta(t) = \begin{cases} 0, & t \neq 0 \\ \infty, & t = 0 \end{cases}$$

The Fourier transform for the unit impulse is

$$\mathrm{F}[\delta(t)] = 1 \tag{1}$$

Therefore, an ideal impulse has a flat frequency response. Although the unit impulse is a theoretical construct and cannot physically exist [8], it is used as a limiting case for when the width of a pulse approaches zero. Derived from the convolution of two rectangular ("rect") functions, the trapezoid function provides an approximation of a realistic impulse with finite rise and fall times [9]:

$$u(t) = \frac{1}{\tau}\,\mathrm{rect}\left(\frac{t}{\tau}\right) \otimes A\,\mathrm{rect}\left(\frac{t}{T}\right) \tag{2}$$

where A is the trapezoid amplitude, T is the full width at half maximum (FWHM), and τ is the rise/fall time from 0 to 100% of the amplitude. The Fourier transform of $u(t)$ is given by

$$\mathrm{F}[u(t)] = AT\,\mathrm{sinc}(f\tau)\,\mathrm{sinc}(fT) \tag{3}$$

The Heaviside unit step function is defined as

$$H(t) = \begin{cases} 1, & t > 0 \\ \frac{1}{2}, & t = 0 \\ 0, & t < 0 \end{cases}$$

This function represents an ideal voltage step which is immediately elevated to a constant level at a definite time [10]. The Fourier transform of $H(t)$ is given by

$$\mathrm{F}[H(t)] = \frac{1}{j2\pi f} + \frac{1}{2}\delta(f) \tag{4}$$

The response varies as the reciprocal of frequency and so approaches zero magnitude as frequency tends to infinity. This theoretical construct cannot physically exist as a realistic step waveform has a finite rise time. The Fourier transform for a step function $s(t)$ with finite rise time is given by

$$\mathrm{F}[s(t)] = A\frac{1}{j2\pi f}\,\mathrm{sinc}(f\tau) \tag{5}$$

where τ is the rise time from 0 to 100% of the amplitude A.

Fig. 2 presents a number of spectra that will be compared with the spectrum of an ideal step (Heaviside unit step) that appears as the dashed line. The new impulse source generates impulses with a typical FWHM of 23 ps [11]. The rise/fall time is estimated as 18 ps (5 ps flat-top). By inserting these parameters in (3), the Fourier transform of a unit amplitude impulse with finite rise and fall times was simulated in Matlab. This can now be compared with the spectrum for the Heaviside unit step from (4) and some realistic step waveforms from (5) in Fig. 2. It can be seen that even the realistic, limited impulse signal contains more energy than an ideal step for frequencies above about 7.5 GHz. When the step waveform is not ideal, but similar to what is practically available today, the comparison becomes even more favorable, as can be seen in the same figure.

IV. Step TDR and Impulse TDR Measurements of an Antenna

Recent studies have demonstrated the successful use of step TDR to characterise the reflection scattering parameter $S_{11}(f)$ of antennas [12], [13]. The motivation behind this work is driven by the fact that a TDR is less expensive than a vector network analyser (VNA), but more importantly the time-localisation of the energy in the transient test signal means that the user can dispense with the anechoic chamber that is required for antenna measurements with a sinewave exciting signal. Subsequent sections describe the measurement of an antenna using the proposed impulse TDR and compare with measurements obtained using conventional step TDR and VNA methods.

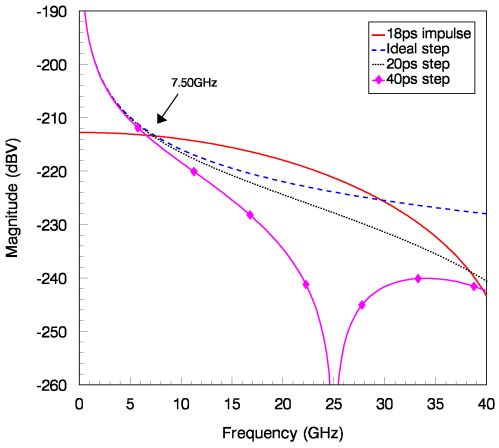

Fig. 2. The Fourier transforms of an ideal unit step, some practical step-like signals, and a practical trapezoidal pulse of unit amplitude. The unit for magnitude is dBV, namely the voltage relative to 1 Volt.

A. Measurement System

An impulse-style TDR was constructed as shown in Fig. 3. The set-up features an Agilent U9391C impulse generator, an Agilent 11636B divider, an Agilent 54754A TDR module, and an Agilent 86100C mainframe in oscilloscope mode. The device under test (DUT) was a Laird Technologies SAH58-120-16-WB wideband sector antenna. The antenna was designed to operate within the 5.47-5.85 GHz frequency range.

The impulse generator produces a series of impulses that are split between the DUT and oscilloscope via a resistive divider. The temporal spacing between each impulse is set by the frequency of the RF source and the generator's internal frequency divider [11]. When an impulse arrives at the DUT, unless the DUT has an impedance equivalent to the characteristic impedance of the system, the DUT will reflect a voltage signal back toward the resistive divider and into the oscilloscope to be measured. Due to high bandwidth requirements, an equivalent-time sampling oscilloscope is employed where triggering is supplied by an external signal from the impulse generator.

A step-type TDR set-up was constructed using a similar configuration but with the impulse source replaced with a 50Ω dummy load and the mainframe set in TDR mode. The divider was included to allow for fair comparison between the impulse

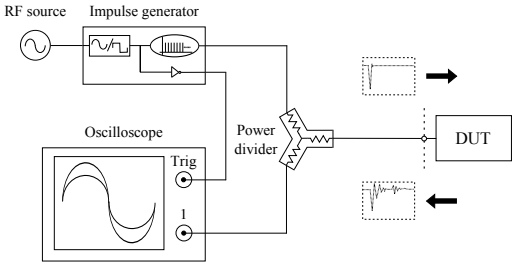

Fig. 3. The set-up for impulse TDR measurements. The dashed line represents the reference plane at the DUT connector.

TDR and step TDR techniques. An attenuator was also inserted between the oscilloscope channel and the divider, to further reduce the step signal to a similar amplitude produced in the impulse TDR set-up.

Calibrated measurements were acquired using a VNA, where the DUT was situated outdoors to provide an accurate reference for comparison with the TDR measurements.

B. Acquisition in the Time-Domain

Two time-domain measurements were employed in the subsequent frequency-domain processing: A reference waveform reflected from a short-circuit, and the waveform reflected by the antenna. Averaged measurements taken by the impulse TDR set-up were windowed with the Dirichlet window in Matlab, to remove the incident portion of the signal and to remove spurious reflections as required for subsequent frequency-domain processing as reported in [12]. The rectangular window contained the essential data that corresponded to the DUT response, and provided a reference plane extended to the end of the cable where the DUT was to be attached. The length of the time window was chosen so that there was sufficient time for the antenna's reflection to settle, while limited to block out spurious reflections caused by the presence of objects near the antenna. Initially, a $35\,\mathrm{ns}$ acquisition window was chosen as endorsed in [12].

Shown in Fig. 4(a) is the reference waveform derived from a short-circuit connected at the reference plane. The large spike corresponds to the reflected impulse, followed by some oscillatory behaviour characteristic of the short-circuit. The short-circuit was replaced with the wideband antenna, and its reflection was measured as shown in Fig. 4(b). The first peak corresponds to the mismatch between the transmission line and the antenna connector. A feed cable within the antenna housing introduced a small delay prior to the actual antenna reflection. The next portion of the waveform corresponds to the resonant behaviour of the antenna. It is clear the $35\,\mathrm{ns}$ acquisition window was sufficient in length as the waveform approaches a steady-state condition before the window ends.

The same process was followed for the acquisition of the step-type TDR measurements.

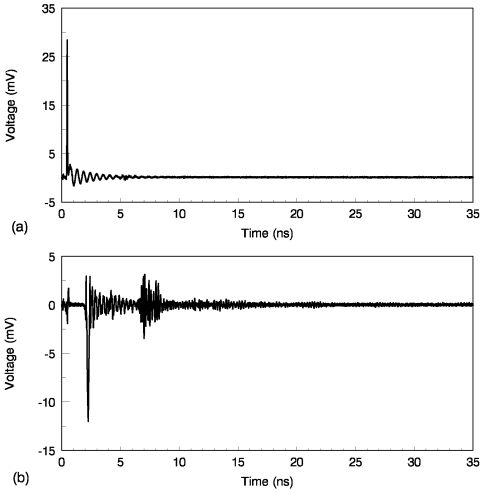

Fig. 4. Plot of the reflected signal seen by the impulse TDR when the (a) short-circuit is connected at the reference plane (b) wideband antenna is connected at the reference plane.

C. Transformation to the Frequency-Domain

Prior to frequency-domain transformation, the time-domain data was processed with the Nicolson algorithm to avoid truncation errors along with the zero-padding operation to ensure adequate frequency resolution [14]. A computer program computed the discrete Fourier transform (DFT) for both the reference reflection and DUT reflection, resulting in $V_{ref}(f)$ and $V_{DUT}(f)$. The reflection scattering parameter $S_{11}(f)$ was then computed by $S_{11}(f) = V_{DUT}(f)/V_{ref}(f)$ for frequencies between 5.4-$6.2\,\mathrm{GHz}$. The DUT $|S_{11}(f)|_{\mathrm{dB}}$ response obtained by both the impulse TDR and step TDR methods, were plotted against the VNA reference as shown in Fig. 5. The frequency range shown is constrained to the antenna's specified operating range. The root mean square error (RMSE) between the VNA and impulse TDR $|S_{11}(f)|$ measurements was calculated as 0.027, whereas the RMSE between the VNA and step TDR $|S_{11}(f)|$ measurements was 0.073. Therefore, the impulse TDR measurement follows the VNA reference more closely than does the step TDR measurement.

D. Dynamic Range

The spectra measured in the reflection from a short-circuit for both the impulse TDR and step TDR systems is shown in Fig. 6(a). Similarly, the spectra present in the DUT reflection for each TDR set-up is shown in Fig. 6(b). It is apparent from both figures that the energy in the impulse TDR reflection exceeds the energy in the step TDR reflection above about $3.1\,\mathrm{GHz}$. Beyond $3.1\,\mathrm{GHz}$ the $23\,\mathrm{ps}$ impulse TDR offers a significant improvement in SNR compared with the Agilent 54754A $40\,\mathrm{ps}$ step TDR. It is worth mentioning that the DFT treats the time-domain waveforms as periodic, resulting in

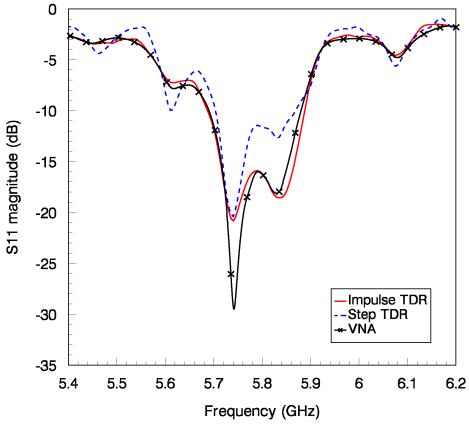

Fig. 5. Comparison of $|S_{11}(f)|_{\mathrm{dB}}$ measurements made by the impulse TDR, step TDR, and VNA, limited to the working frequency range of the wideband antenna.

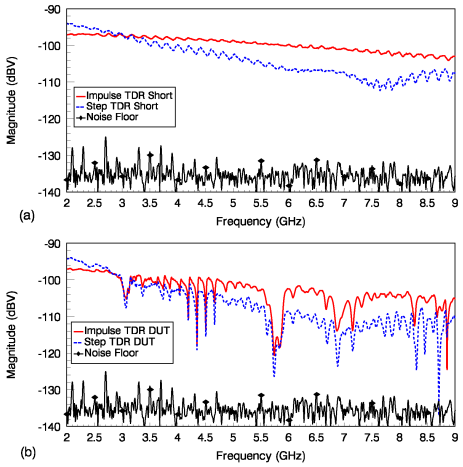

Fig. 6. The frequency spectra for the impulse TDR and step TDR measurements when the (a) reference short-circuit was connected at the reference plane (b) DUT was connected at the reference plane. The noise floor was determined by measuring the noise present in the system with the signal source disabled.

spectra that are scaled slightly different in magnitude than the spectra produced by the continuous Fourier transform of single transient signals in Fig. 2.

Recommendations for the application of impulse TDR, step TDR, and VNA measurement techniques, are summarised in Table I.

V. Conclusion

Impulse TDR does not have an intuitive or informative display, making it less desirable for conventional measurements. However, in the situation where the user will post-process reflection waveform data, for example, to determine S-parameters, the impulse version of TDR is superior at frequencies above 7.5 GHz. It may also be advantageous when the user is looking for precision in spatial localisation, say in a connector or similar in-line structure, as the increased energy at higher frequencies can help.

TABLE I
Comparison of Measurement Techniques

Technique	Bandwidth	Dynamic range	Equipment cost	Anechoic chamber
Impulse TDR	Med	Med	Med	No
Step TDR	Low	Low	Med	No
VNA	High	High	High	Yes

Acknowledgement

The authors wish to acknowledge the support of Agilent Technologies Component Test Division for the supply and detailed support of equipment. Thanks are also due to Skynet Data Communications Technology Ltd for the supply of equipment and support.

References

[1] *Time Domain Reflectometry Theory,* Agilent Technologies, USA, Application Note 1304-2, 2006. http://cp.literature.agilent.com/litweb/pdf/5966-4855E.pdf retrieved Jan 2010.

[2] M. Harper, N. Ridler, and M. Salter, "Comparison Between Root-Impulse-Energy and Vector Network Analyzer Methods for Measuring Loss on Printed Circuit Boards", in *ARFTG Microwave Measurement Symp.*, in Portland, OR, 2008, pp. 20-25.

[3] C. Chiu, W. Chen, K. Liao, B. Chen, Y. Teng, G. Huang, and L. Wu, "Pad Characterization for CMOS Technology Using Time Domain Reflectometry", in *Proc. IEEE Int. RF and Microwave Conf.*, in Kuala Lumpur, Dec. 2008, pp. 215-217.

[4] H. Songoro, M. Vogel, and Z. Cendes, "Keeping Time with Maxwell's Equations", *IEEE Microwave Magazine*, vol. 11, no. 2, pp. 42-49, Apr. 2010.

[5] J. Scott and D. Gunyan, "Pulse Generator", US patent number *7,423,470*, Sep, 2008.

[6] J. Scott and M. Hoy, "Group-Delay Measurement of Frequency-Converting Devices Using a Comb Generator", *IEEE Trans. Instrum. Meas.*, vol. 59, no. 11, pp. 3012-3017, Nov. 2010.

[7] P. Blockley, D. Gunyan, and J. Scott, "Mixer-Based, Vector-Corrected, Vector/Network Analyzer Offering 300kHz-20GHz Bandwidth and Traceable Response", *IEEE Int. Microwave Symp.* in Long Beach, CA, Jun. 2005, pp. 1-4.

[8] S. Haykin and M. Moher, "Introduction to Analog & Digital Communications, Second Edition", *John Wiley & Sons, Inc*, pp. 42-49, 2007.

[9] D. Brandwood, "Fourier Transforms in Radar and Signal Processing", *Artech House, Inc.*, pp. 39-47, 2003.

[10] R. N. Bracewell, "The Fourier Transform and its Applications, Third Edition", *McGraw-Hill International Editions*, pp. 61, 2000.

[11] "Agilent U9391C/F Comb Generators Technical Overview", *Agilent Technologies*, http://www.home.agilent.com/agilent/product.jspx?pn=U9391C retrieved Jan 2010.

[12] A. Cataldo, G. Monti, E. De Benedetto, G. Cannazza, L. Tarricone, and L. Catarinucci, "Assessment of a TD-Based Method for Characterization of Antennas", *IEEE Trans. Instrum. Meas.*, vol. 58, no. 5, pp. 1412-1419, May. 2009.

[13] R. Tamas, G. Caruntu, and D. Popa, "A Time-Domain Measuring Technique for Ultra-Wide Band Antennas", *Microwave and Optical Technology Letters*, vol. 53, no. 2, pp. 281-286, Feb. 2011.

[14] A. Cataldo, L. Catarinucci, L. Tarricone , F. Attivissimo, and A. Trotta, "A TD-FD Combined Method for Enhancing Reflectometry Measurements in Liquid Quality Monitoring", in *Proc. IEEE Instrum. Meas. Tech. Conf.*, in Warsaw, May. 2007, pp. 1-5.

Appendix C

Measured Spectra in Stimulus Signals

The impulse from the Agilent U9391C generator and the step from the Agilent 54754A TDR were measured directly through the input channels of the oscilloscope and their spectra were plotted as shown in figure C.1. It is worth pointing out the stimulus signals differed in magnitude; the impulse had an amplitude of $-250\,\text{mV}$, whereas the step had an amplitude of $200\,\text{mV}$. The ripples present in the impulse spectra between 30-40 GHz are attributed to multimode effects occurring within the coaxial cable connecting the Agilent U9391C to the oscilloscope. Beyond 4.7 GHz, the 23 ps impulse contains more energy than the 40 ps step.

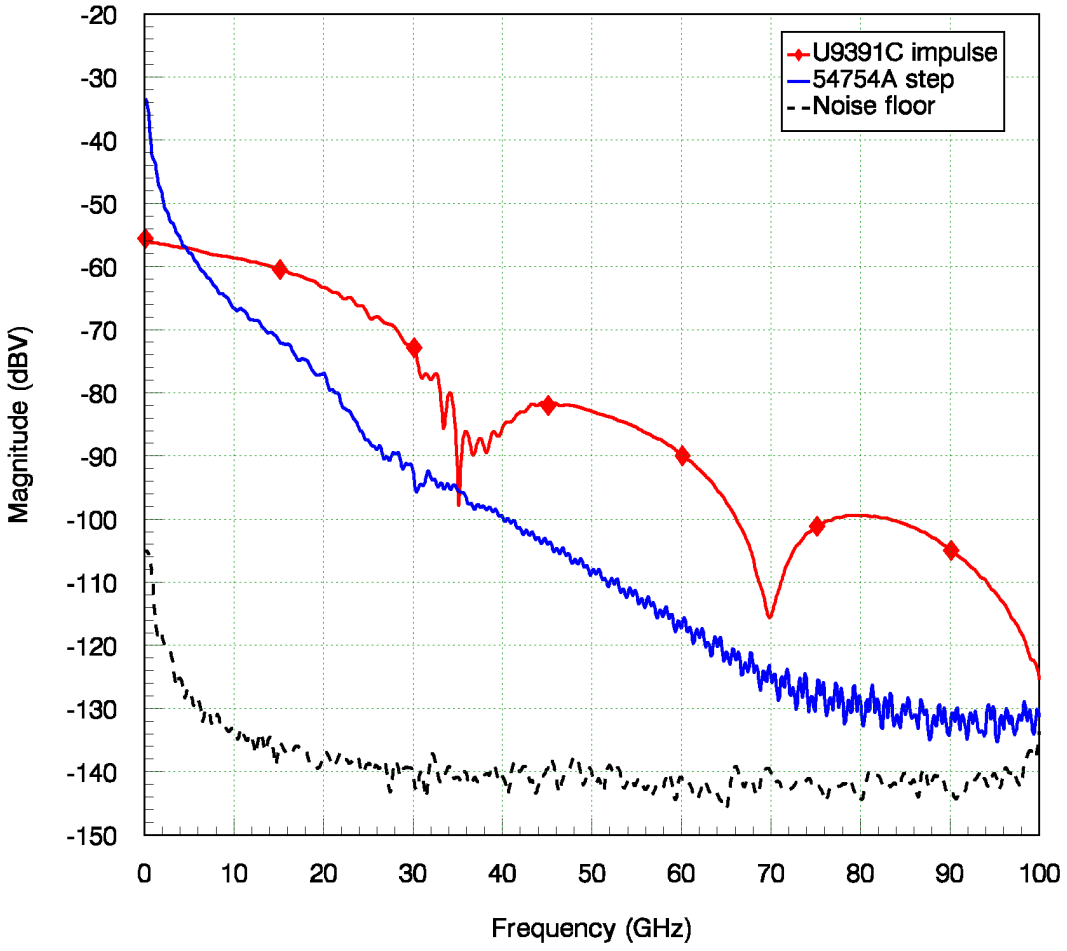

Figure C.1: *The frequency spectra for the Agilent U9391C impulse and the Agilent 54754A step. The noise floor was determined by measuring the noise present in the system with the signal source disabled.*

Appendix D

Specifications of the Impulse Generator

Agilent U9391C/F Comb Generators

U9391C (10 MHz to 26.5 GHz)
U9391F (10 MHz to 50 GHz)

Technical Overview

Key Features

Agilent's U9391C/F comb generators are designed as a phase reference standard for the Agilent PNA-X nonlinear vector network analyzer (NVNA).

- Excellent amplitude and phase flatness enable it to be used as a precision calibration phase reference standard for the NVNA
- NIST traceable phase calibration guarantees a reliable reference to international standards
- Embedded calibration data can be easily accessed via the plug-and-play USB interface
- The USB interface facilitates frequency divider control and calibration data retrieval via the PNA-X
- Rugged 2.4-mm and 3.5-mm bulk-head connectors guarantee high repeatability throughout multiple connects and disconnects

Agilent Technologies

Options

Output connectors

Option FFF – female (output port)
Option FFM – male (output port)

Specifications [1]

Specifications refer to the performance standards or limits against which the U9391C/F comb generators are tested.

Typical characteristics are included for additional information only and they are not specifications. These are denoted as "typical", "nominal" or "approximate" and are printed in italic.

Specifications	U9391C	U9391F
Output frequency range [1]	10 MHz to 26.5 GHz	10 MHz to 50 GHz
Input frequency range	10 MHz to 6 GHz	10 MHz to 6 GHz
Input power range	–15 to +15 dBm	–15 to +15 dBm
Min output power per picket	–80 dBm at 10 MHz input PRF	–95 dBm at 10 MHz input PRF
Amplitude flatness vs. output frequency	< 12 dB at 10 MHz input PRF	< 25 dB at 10 MHz input PRF
Amplitude flatness vs. input power	*0.1 dB (typical)*	*0.1 dB (typical)*
Phase flatness [2]	± 8.5 degrees (10 MHz to 3 GHz); ± 6.5 degrees (3 GHz to 20 GHz); ± 8.5 degrees (20 GHz to 26.5 GHz)	+ 10/–10 degrees (10 MHz to 28 GHz); + 15/–17.5 degrees (28 GHz to 38 GHz); + 15/–30 degrees (38 GHz to 45 GHz); + 15/–40 degrees (45 GHz to 50 GHz)
Pulse width	< 23 ps	< 23 ps
Divide ratio	1, 2, 4, 8, 16	1, 2, 4, 8, 16
Input return loss, S11	> 10 dB (10 MHz to 6 GHz)	> 10 dB (10 MHz to 6 GHz)
Output return loss, S22	> 10 dB (10 MHz to 26.5 GHz)	> 10 dB (10 MHz to 20 GHz) > 7 dB (20 GHz to 45 GHz) > 5 dB (45 GHz to 50 GHz)

1 When driven by low phase noise sources, this comb generator will operate at frequencies lower than 10 MHz, but performance is not guaranteed.
2 For operation below 100 MHz, use a square wave to drive the comb generator.
3. The speciafications refers to the raw performance data. For NVNA application, the phase performance are corrected with the calibration data, not at spurious frequency. Spurious frequency at n*250 MHz and also at input drive frequency.

Environmental Specifications

U9391C/F comb generators are designed to fully comply with Agilent's product operating environment specifications. The following are the summarized environmental specifications for these products.

Specifications	Limits
Temperature	
Operating	0 °C to +55 °C
Storage	–40 °C to +70 °C
Error corrected range	23 °C ±3 °C
Cycling	–65 °C to +85 °C, 10 cycles at 20 °C per minute. 20 minutes dwell time per MIL-STD-883F, Method 1010.8, Condition C (modified)
Relative humidity	
Operation	50% to 95% RH at 40 °C, 24 hours cycling, repeated 5 times
Storage	90% RH at 65 °C, one 24 hour cycle
Shock	
End-use handling shock	Half-sine waveform, 2-3 ms duration, 60 in/s (1.6 ms) delta-V
Transportation shock	Trapezoidal waveform, 18-22 ms duration, 337 in/s (8.56 ms) delta-V
Vibration	
Operating	Random: 5 to 500 Hz, 0.21 grms, 10 min/axis
Survival	Random: 5 to 500 Hz, 2.09 grms, 10 min/axis Swept sine: 5 to 500 Hz, 0.5 grms, 10 min/axis, 4 resonance search, 10 min dwell
Altitude	
Operating	< 4,572 meters (15,000 ft)
Storage	< 15,000 meters (50,000 ft)
ESD immunity	
Direct discharge [1]	8.0 kV per IEC 61000-4-2
Air discharge	15 kV per IEC 61000-4-2

1 To outer conductor

1 Note: The U9391C/F was specially designed for use with the PNA-X **ONLY**.

Typical Performance

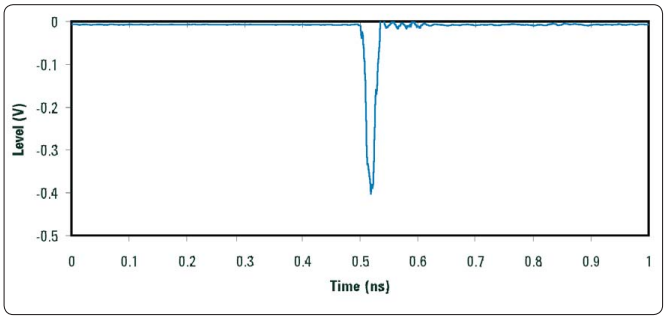

Figure 2. U9391C/F pulse

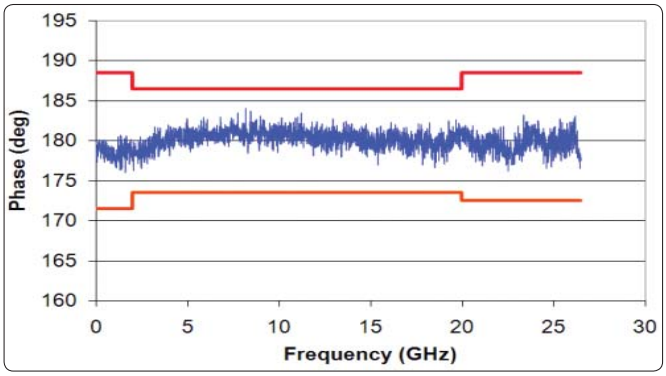

Figure 3. U9391C comb generator phase at 10 MHz PRF

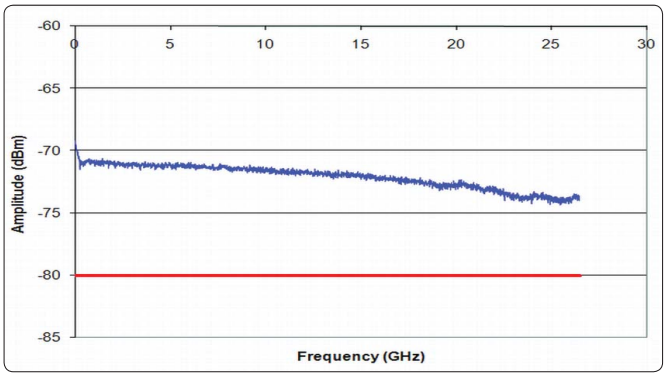

Figure 4. U9391C comb generator magnitude at 10 MHz PRF

Appendix E

Specifications of the Wideband Antenna

Laird TECHNOLOGIES

Innovative **Technology** for a **Connected** World

HORIZONTALLY POLARIZED SECTOR ANTENNAS

SAH58-WB

5470-5850 MHZ HORIZONTALLY POLARIZED WIDE-BAND SECTOR ANTENNA

The horizontally polarized sector antenna systems offered by Laird Technologies are constructed of UV stable ABS plastic radomes and die cast aluminum brackets for long service life in the most demanding conditions. The horizontal polarization allows for reduced interference potential in systems which are installed in areas with high levels of vertically polarized RF noise or where the system manager wants to avoid potential future problems with interference. The super heavy duty bracket system is easy to install and adjust for up to 15 deg of downtilt. The single point bracket allows for easy deployment of multiple sectors around a single pole.

FEATURES RoHS

- Wide-band operation
- Horizontally polarized
- High-gain in a small form factor
- Type N female integrated connector
- Completely weatherproof

MARKETS

- 5.8GHz U-NII band applications
- Base station antennas
- Point to multi-point systems
- 802.11a applications

PARAMETER	SAH58-120-16-WB	SAH58-90-17-WB
Frequency range	5400 - 5850 MHz	5400 - 5850 MHz
VSWR	1.5:1	1.5:1
Impedance	50 ohm	50 ohm
Input power	100W	100W
Pole diameter (OD)	1.5"- 3" (38-76mm)	1.5"- 3" (38-76mm)
Operating temperature	-40 - +70°C	-40 - +70°C
Gain	15 dBi	17 dBi
Horizontal beamwidth	120°	90°
Vertical beamwidth	6°	6°
Polarization	Horizontal	Horizontal
Front-to-back	>25 dB	>26 dB
Mechanical downtilt	15°	15°
Weight	2.6 lbs (1.2 kg)	2.6 lbs (1.2 kg)
Dimensions (L x W x H)	22" x 5" x 2.8" (554 x 125 x 71mm)	22" x 5" x 2.8" (554 x 125 x 71mm)

WIND LOADING

MODEL	SQ. IN	100 MPH	125 MPH
SAH58-WB	110	27.5 lb	43 lb

SYSTEM ORDERING

SAH58-120-16-WB 5400-5850MHz 120deg, 15dBi, wide-band HPOL sector antenna
SAH58-90-17-WB 5400-5850MHz 90deg, 17dBi, wide-band HPOL sector antenna

ANTENNA PATTERNS

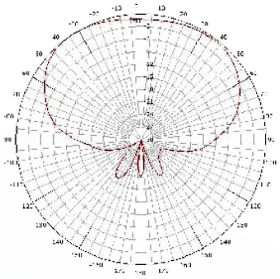

SAH58-120-16-WB
Azimuth

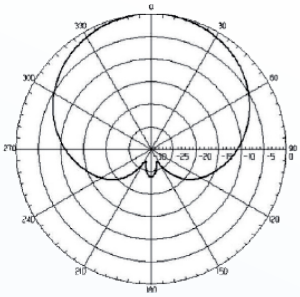

SAH58-90-17-WB
Azimuth

global solutions: local support™

Americas: +1.847 839.6907
IAS-AmericasEastSales@lairdtech.com

Europe: +1.32.80.7866.12
IAS-EUSales@lairdtech.com

Asia: +1.65.6.243.8022
IAS-AsiaSales@lairdtech.com

www.lairdtech.com

ANT-DS-SAH58-WB 0610

Appendix F

Specifications of the Test Cables

FLEX TEST™

Test Cable

CBL-1.5FT-SMSM+

50Ω 1.5FT DC to 18 GHz

Maximum Ratings

Operating Temperature	-55°C to 105°C
Storage Temperature	-55°C to 105°C

Permanent damage may occur if any of these limits are exceeded.

Shielding Effectiveness	>100 dB
Power Handling at 25°C	891W Max. at 0.4 GHz
	539W Max. at 1 GHz
	363W Max. at 2 GHz
	180W Max. at 6 GHz
	117W Max. at 12 GHz
	88W Max. at 18 GHz
Jacket	Clear FEP

Features

- RoHS compliant
- wideband coverage, DC to 18 GHz
- extra rugged construction with strain relief for longer life
- stainless steel SMA connectors for long mating-cycle life
- useful over temperature range, -55°C to 105°C
- triple shield cable for excellent shielding effectiveness
- flexible for easy connection & bend radius
- superior stability of insertion loss, VSWR & phase vs. flexing
- 6 month guarantee*

Applications

- high volume production test stations
- research & development labs
- environmental & temperature test chambers
- replacement for OEM test port cables
- field RF testing
- cellular infrastructure site testing

CASE STYLE: GM1006-1.5

Connectors		Model	Price	Qty.
Conn1	**Conn2**			
SMA-MALE	**SMA-MALE**	CBL-1.5FT-SMSM+	$68.95 ea.	(1-9)

+ RoHS compliant in accordance with EU Directive (2002/95/EC)

The +Suffix has been added in order to identify RoHS Compliance. See our web site for RoHS Compliance methodologies and qualifications.

Outline Drawing

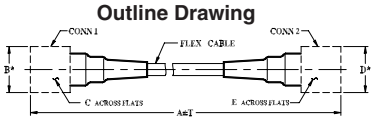

*OVERALL CONNECTOR OR CABLE & BOOT DIMENSION (CONNECTOR SHAPE MAY VARY)

Outline Dimensions (inch / mm)

A		B	C	D	E	T		wt
Feet	Meters					Feet	Meters	grams
1.5	0.46	0.42 10.67	0.312 7.92	0.42 10.67	0.312 7.92	0.06	0.02	58

Cable Cross Section

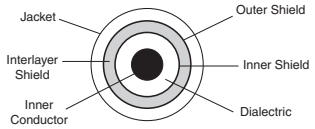

Cable Construction	
Inner Conductor	Solid Silver Plated Copper Clad Steel
Dielectric	Solid PTFE
Shield	Silver-Plated Copper Flat Ribbon Braid Aluminum-Polymide Tape Interlayer 36 GA Silver-Plated Copper Braid (90%k)
Jacket	Clear FEP
Connectors	
• passivated stainless steel • captive contact • thick wall interface (SMA) • gold plated beryllium copper center contacts • PTFE dielectric	

Product Guarantee*

Mini-Circuits® will repair or replace your test cable at its option if the connector attachment fails within six months of shipment. This guarantee excludes cable or connector interface damage from misuse or abuse.

Electrical Specifications at 25˚C

FREQ. (GHz)	LENGTH (FT)	INSERTION LOSS (dB)								RETURN LOSS (dB)							
		DC-2.5 GHz		2.5-6 GHz		6-12 GHz		12-18 GHz		DC-2.5 GHz		2.5-6 GHz		6-12 GHz		12-18 GHz	
f_L-f_U		Typ.	Max.	Typ.	Max.	Typ.	Max.	Typ.	Max.	Typ.	Min.	Typ.	Min.	Typ.	Min.	Typ.	Min.
DC-18	1.5	0.25	0.6	0.4	0.85	0.7	1.2	1.0	1.4	30	23	30	20	27	17	27	17

Custom sizes available, consult factory.

Typical Performance Data

Frequency (MHz)	Insertion Loss (dB)	Return Loss (dB)	
		SMA-MALE	SMA-MALE
50.00	0.03	44.38	43.98
1000.00	0.19	30.17	29.84
2000.00	0.28	35.48	39.27
2500.00	0.31	33.87	39.52
4000.00	0.41	45.40	42.81
5000.00	0.47	34.89	36.08
6000.00	0.52	38.60	38.07
7000.00	0.58	29.78	29.85
8000.00	0.62	39.06	43.08
9000.00	0.68	24.52	24.41
10000.00	0.72	31.52	30.55
12000.00	0.83	21.01	21.15
13000.00	0.84	30.94	31.64
15000.00	0.94	22.65	22.98
18000.00	1.03	31.24	49.01

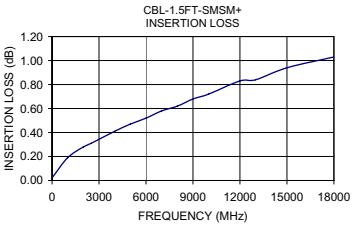

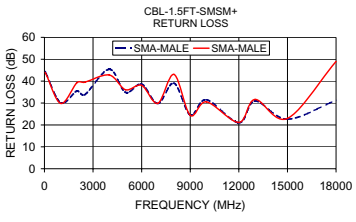

References

[1] J. Scott, "Rapid millimetre-wave sampler response characterization to well beyond 120GHz using an improved nose-to-nose method", *paper TH3A-3, MTT-s IMS Digest, Philadelphia*, pp. 1511–1514, Jun. 2003.

[2] *Agilent Technologies Infiniium 90000 X-Series oscilloscopes,* Agilent Technologies, USA, Data Sheet, 2011.

[3] *Infiniium DCA-J Agilent 86100C wide-bandwidth oscilloscope mainframe and modules,* Agilent Technologies, USA, Data Sheet, 2011.

[4] *Infiniium DCA-J Agilent 86100D wide-bandwidth oscilloscope mainframe and modules,* Agilent Technologies, USA, Data Sheet, 2011.

[5] *Digital serial analyzer sampling oscilloscope,* Tektronix, US, Data Sheet, 2011.

[6] S. W. Smith, "The scientist and engineer's guide to digital signal processing", *San Diego, CA, California Technical Publishing*, pp. 35–66, 1997.

[7] T. H. O'Dell, "Circuits for electronic instrumentation", *Press Syndicate of the University of Cambridge*, pp. 27–36, 1991.

[8] *Sampling oscilloscope techniques,* Tektronix, US, Technique Primer 47W-7209, 1989. [Online]. Available: `http://www.cbtricks.com/miscellaneous/tech_publications/scope/sampling.pdf`

[9] *Evaluating oscilloscope sample rates vs. sampling fidelity* Agilent Technologies, USA, Application Note, 2011.

[10] S. Haykin and M. Moher, "Introduction to analog & digital communications, second edition", *John Wiley & Sons, Inc*, pp. 42–49, pp. 197, 2007.

[11] *What is the difference between an equivalent time sampling oscilloscope and a real-time oscilloscope?*, Agilent Technologies, USA, Application Note 1608, 2008, [Online]. Available: `http://cp.literature.agilent.com/litweb/pdf/5989-8794EN.pdf`

[12] *Agilent 83496A clock recovery module,* Agilent Technologies, USA, Data Sheet, 2006.

[13] *XYZs of oscilloscopes primer,* Tektronix, US, 2009. [Online]. Available: `http://www2.tek.com/cmsreplive/tirep/2280/03W-8605-5%20low%20res_2010.03.04.17.57.03_2280_EN.pdf`

[14] A. J. Metz, "Sampling bridge", US patent number *4,659,945*, Apr. 1987.

[15] W. M. Grove, "Sampling for oscilloscopes and other RF systems: DC through X-band" *IEEE Tran. Microw. Theory Tech.*, vol. MTT-14, no. 12, pp. 629–635, Dec. 1966.

[16] M. Kahrs, "Applications of RF and microwave sampling to instrumentation and measurement" *IEEE MTT-S Digest*, vol. 3, pp. 1503–1506, Jun. 2003.

[17] K. A. Remley and D. F. Williams, "Sampling oscilloscope models and calibrations" *IEEE MTT-S Digest*, vol. 3, pp. 1507–1510, Jun. 2003.

[18] D. F. Williams and K. A. Remley, "Analytic sampling-circuit model" *IEEE Tran. Microw. Theory Tech.*, vol. 49, no. 6, pp. 1013–1019, Jun. 2001.

[19] D. A. Neamen, "Microelectronics: circuit analysis and design, third edition", *The McGraw-Hill Companies, Inc.*, pp. 39–44, 2007.

[20] D. F. Williams, P. Hale and K. A. Remley, "The sampling oscilloscope as a microwave instrument", *IEEE Microwave Magazine*, vol. 8, no. 4, pp. 59–68, Aug. 2007.

[21] *Coaxial cables*, Axon Cable Inc, Oct. 1998. `http://axoncable.com/pdf/coax_A.pdf` retrieved Mar 2011.

[22] F. R. Dungan, "Electronic communications systems", *PWS Publishers*, pp. 160–179, 1987.

[23] *Time domain reflectometry*, Hewlett Packard, USA, Application Note 62, 1988.

[24] S. Ramo, J. R. Whinnery, T. Van Duzer, "Fields and waves in communication electronics, second edition", *John Wiley & Sons, Inc*, pp. 217, 1984.

[25] L. Navarro, E. Mayevskiy, and T. Chairet, "Measurements of characteristic impedance of high frequency cables with time domain reflectometry (TDR)", in *ARFTG Microwave Measurement Symposium, 2008 72nd*, pp. 9–19, Dec. 2008.

[26] *Time domain reflectometry theory,* Agilent Technologies, USA, Application Note 1304-2, 2006. `http://cp.literature.agilent.com/litweb/pdf/5966-4855E.pdf` retrieved Jan 2010.

[27] *Agilent high precision time domain reflectometry,* Agilent Technologies, USA, Application Note 1304-7, 2003.

[28] P. Horowitz and W. Hill, "The art of electronics, second edition", *Cambridge University Press*, pp. 20–33, 1989.

[29] A. Cataldo, G. Monti, E. De Benedetto, G. Cannazza, L. Tarricone, and L. Catarinucci, "A comparative analysis of reflectometry methods for characterization of antennas", in *Proc. IEEE Instrum. Meas. Tech. Conf.*, in Canada, May. 2008, pp. 240–243.

[30] *Agilent network analyzer basics*, Agilent Technologies, USA, Application Note 5965-7917E, 2004.

[31] L. F. Chen, C. K. Ong, C. P. Neo, V. V. Varadan, and V. K. Varadan, *Microwave electronics measurement and materials characterization*, John Wiley & Sons, pp. 126–174, 2004.

[32] *TDR and S-parameters measurements - how much performance do you need?*, Tektronix, US, Application Note, 2006.

[33] A. Cataldo, G. Monti, E. De Benedetto, G. Cannazza, L. Tarricone, and L. Catarinucci, "Assessment of a TD-based method for characterization of antennas", *IEEE Trans. Instrum. Meas.*, vol. 58, no. 5, pp. 1412–1419, May. 2009.

[34] S. M. Riad, "The deconvolution problem: an overview", *Proc. IEEE*, vol.74, no.1, pp. 82–85, Jan. 1986

[35] J. Dunsmore, "Gating effects in time domain transforms", in *ARFTG Microwave Measurement Symposium, 2008 72nd*, pp. 1–8, Dec. 2008.

[36] *S-parameters, insertion and return loss measurements using TDR oscilloscope*, Application Note SPARA-0503, TDA Systems, USA, 2003.

[37] *Tektronix user manual - IConnect and MeasureXtractorTM TDR and VNA software*, Tektronix Inc., Beaverton, OR.

[38] *Time domain spectrum analyzer and "S" parameter vector network analyzer*, Application Note AN-16a, Picosecond Pulse Labs, USA, 2004.

[39] C. Wakayama and J. Loyer, "Correlation between VNA and TDR/TDT extracted S-Parameters up to 20 GHz", *Intel Corp./Univ*, Washington, 2005.

[40] *TDR and VNA measurement primer*, Application Note TVMP-0404, TDA Systems, USA, 2004.

[41] F. J. Harris, "On the use of windows for harmonic analysis with the discrete Fourier transform," *Proceedings of the IEEE.*, vol. 66, no. 1, pp. 51–83 Jan. 1978.

[42] A. A. Girgis and F. M. Ham, "A quantitative study of pitfalls in the FFT," *IEEE Trans. Aero. Elec. Sys.*, vol. AES-16, no. 4, pp. 434–439, Jul. 1980.

[43] J. Waldmeyer, "Fast Fourier transform for step-like functions: the synthesis of three apparently different methods" *IEEE Trans. Instrum. Meas.*, vol. IM-29, no. 1, pp. 36–39, Mar. 1980.

[44] R. G. Lyons, *Understanding digital signal processing*, Prentice Hall PTR, pp. 49–154, 2001.

[45] M. Harper, N. Ridler, and M. Salter, "Comparison between root-impulse-energy and vector network analyzer methods for measuring loss on printed circuit boards", in *ARFTG Microwave Measurement Symp.*, in Portland, OR, 2008, pp. 20–25.

[46] *Improving TDR/TDT measurements using normalization*, Agilent Technologies, USA, Application Note 1304-5, 2001.

[47] S. O. Kasap, "Optoelectronics and photonics, principles and practices", *Prentice-Hall, Inc.*, pp. 79, 2001.

[48] *IPC TM-650 Test methods manual, method 2.5.5.12: Signal propagation loss*, IPC Association, May. 2009. `http://www.ipc.org/4.0_Knowledge/4.1_Standards/test/2-5_2-5-5-12.pdf` retrieved Sep 2011.

[49] A. Rajagopal, "Printed circuit board (PCB) loss characterization up-to 20GHz and modeling, analysis and validation", M.S. thesis, Univ. Missouri-Rolla, 2007.

[50] C. Chiu, W. Chen, K. Liao, B. Chen, Y. Teng, G. Huang, and L. Wu, "Pad characterization for CMOS technology using time domain reflectometry", in *Proc. IEEE Int. RF and Microwave Conf.*, in Kuala Lumpur, Dec. 2008, pp. 215–217.

[51] *Agilent basics of measuring the dielectric properties of materials,* Agilent Technologies, USA, Application Note 5989-2589, 2006.

[52] F. Attivissimo, G. Cannazza, A. Cataldo, E. De Benedetto, and L. Fabbiano, "Enhancement and metrological characterization of an accurate and low-cost method based on seismic wave propagation for soil moisture evaluation", *IEEE Trans. Instrum. Meas.*, vol. 59, no. 5, pp. 1216–1223, May. 2010.

[53] E. Piuzzi, A. Cataldo, G. Cannazza, and E. De Benedetto, "An improved reflectometric method for soil moisture measurement exploiting an innovative triple-short calibration", *IEEE Trans. Instrum. Meas.*, vol. 59, no. 10, pp. 2747–2754, Oct. 2010.

[54] M. Vallone, A. Cataldo, and L. Tarricone, "Water content estimation in granular materials by time domain reflectometry: a key-note on agro-food applications", in *Proc. IEEE Instrum. Meas. Tech. Conf.*, in Warsaw, May. 2007, pp. 1–6.

[55] C. V. Kandala and J. Sundaram, "Nondestructive measurement of moisture content using a parallel-plate capacitance sensor for grain and nuts", IEEE Sensors Journal, vol. 10, no. 7, pp. 1282-1287, Jul. 2010.

[56] A. M. Nicolson and G. F. Ross, "Measurement of the intrinsic properties of materials by time-domain techniques", IEEE Trans. Instrum. Meas., vol. 19, no. 4, pp. 377-382, Nov. 1970.

[57] D. Brandwood, *Fourier transforms in radar and signal processing*, Artech House, Inc., pp. 39–47, 2003.

[58] R. N. Bracewell, *The Fourier transform and its applications, third edition*, McGraw-Hill International Editions, pp. 61, 2000.

[59] *Agilent U9391C/F comb generators technical overview*, Agilent Technologies, [Online]. Available: `http://www.home.agilent.com/agilent/product.jspx?pn=U9391C` retrieved Jan 2010.

[60] J. Scott and D. Gunyan, "Pulse generator", US patent number *7,423,470*, Sep, 2008.

[61] J. Scott and M. Hoy, "Group-delay measurement of frequency-converting devices using a comb generator", *IEEE Trans. Instrum. Meas.*, vol. 59, no. 11, pp. 3012–3017, Nov. 2010.

[62] P. Blockley, D. Gunyan, and J. Scott, "Mixer-based, vector-corrected, vector/network analyzer offering 300kHz-20GHz bandwidth and traceable response", *IEEE Int. Microwave Symp.* in Long Beach, CA, Jun. 2005, pp. 1–4.

[63] *Horizontally polarized sector antennas SAH58-WB*, Laird Technologies, datasheet ANT-DS-SAH58-WB 0610, 2010.

[64] *Agilent 54753A and 54754A TDR plug-in modules user guide*, Agilent Technologies, publication number 54753-97015, 2000.

[65] B. F. Lawrence, "Anechoic chambers, past and present", Conformity, pp. 1-3, Feb. 2005.

[66] W. Kim and M. Swaminathan, "Simulation of lossy package transmission lines using extracted data from one-port TDR measurements an nonphysical RLGC models", IEEE Trans. Adv. Packaging , vol. 28, no. 4, pp. 736–744, Nov. 2005.

[67] T. Dhaene, L. Martens, K. De Kesel, and D. De Zutter, "Advanced calibration and normalization techniques for time domain reflection and

transmission measurements", IEEE Instrum. Meas. Tech. Conf. 1993 IMTC/93, pp. 377–380, 18-20 May. 1993.

[68] T. Dhaene, L. Martens, and D. De Zutter, "Calibration and normalization of time domain network analyzer measurements", IEEE Trans. Microwave Theory and Techniques, vol. 42, no. 4, pp. 580–589, Apr. 1994.

[69] J. K. Hunton, "Analysis of microwave measurement techniques by means of signal flow graphs", IRE Trans. Microwave Theory and Techniques, vol. 8, no. 2, pp. 206–212, Mar. 1960.

[70] D. M. Pozar, *Microwave engineering, third edition*, John Wiley & Sons, Inc., pp. 189–197, 2005.

[71] A. Cataldo, L. Catarinucci, L. Tarricone, F. Attivissimo, and A. Trotta, "A TD-FD combined method for enhancing reflectometry measurements in liquid quality monitoring", in *Proc. IEEE Instrum. Meas. Tech. Conf.*, in Warsaw, May. 2007, pp. 1–5.

[72] A. Cataldo, L. Catarinucci, L. Tarricone, F. Attivissimo, and E. Piuzzi, "A combined TD-FD method for enhanced reflectometry measurements in liquid quality monitoring", *IEEE Trans. Instrum. Meas.*, vol. 58, no. 10, pp. 3534–3543, Oct. 2009.

[73] S. McCabe and J. Scott, "Measurement of antennas and microwave components using time-domain reflectometry of a voltage impulse", *IEEE Microwave and Wireless Components Letters*, vol. 21, no. 11, pp. 634–636, Nov. 2011.